

**Phonon and electron transport through interfaces
and disordered structures**

by

Qichen Song

Submitted to the Department of Mechanical Engineering
in partial fulfillment of the requirements for the degree of

Doctor of Philosophy in Mechanical Engineering

at the

MASSACHUSETTS INSTITUTE OF TECHNOLOGY

February 2022

© Massachusetts Institute of Technology 2022. All rights reserved.

Author
Department of Mechanical Engineering
Feb 1, 2022

Certified by
Gang Chen
Carl Richard Soderberg Professor of Power Engineering
Thesis Supervisor

Certified by
Asegun Henry
Robert N. Noyce Career Development Associate Professor
Thesis Supervisor

Accepted by
Nicolas G. Hadjiconstantinou
Chairman, Department Committee on Graduate Theses

Phonon and electron transport through interfaces and disordered structures

by

Qichen Song

Submitted to the Department of Mechanical Engineering
on Feb 1, 2022, in partial fulfillment of the
requirements for the degree of
Doctor of Philosophy in Mechanical Engineering

Abstract

Understanding phonon and electron transport is of great significance for designing efficient solid-state devices such as transistors, laser diodes and thermoelectric energy converters. The structural randomness is inevitable in solid-state devices, and it is often regarded as the undesirable scattering source for phonons and electrons. This thesis studies manipulating phonon and electron flow using structural randomness via mode-resolved Green's function calculations and pump-probe optical characterizations.

Interface roughness is a common type of randomness in heterostructures, which strongly affects electron and phonon transport across interfaces. We find that atomically rough interfaces can scatter short-wavelength electrons and assist the transmission between mismatched valleys. The contact resistance is reduced by over an order of magnitude. Our study provides new insights on the conventional wisdom to improve the interfacial transport using graded interfaces. We also use the atomistic Green's function to simulate phonon transport across rough interfaces to show that the basic assumption that phonons lose memories in the often-used diffuse phonon scattering model is questionable.

The coherent backscattering of waves in disordered structures can lead to Anderson localization, where the waves are spatially localized and cannot propagate. Anderson localization has been observed in electronic, photonic and acoustic systems. However, observing its impact on heat conduction is challenging due to the broadband nature and three-dimensional transport of phonons. We use the aperiodicity as a type of randomness to enhance phonon Anderson localization. Our calculation predicts that aperiodic Si/Si_{0.2}Ge_{0.8} superlattice can induce coherent backscattering for low-frequency phonons and limit the contribution to transport of high-frequency phonons. The interferences among scattered low-frequency phonons lead to a peak in the thermal conductivity versus length curve, a characteristic feature of phonon Anderson localization. Using frequency-domain thermoreflectance, we validate our theoretical predictions and find that the phonon Anderson localization exists up to 200 K. Our findings provide an efficient approach to localize phonons at moderate

temperatures using randomness.

Thesis Supervisor: Gang Chen
Title: Carl Richard Soderberg Professor of Power Engineering

Thesis Supervisor: Asegun Henry
Title: Robert N. Noyce Career Development Associate Professor

Acknowledgments

I want to thank Prof. Gang Chen, who initiated several important research topics covered in this thesis and gives great advice all the time. He spent a lot of time to improve my presentations and my writings (including this thesis). More importantly, he shows me how to study fundamental problems and produce scientific works with true impacts. I admire his courage to challenge tough fundamental problems and I want to be like that as well. I am very grateful to Prof. Asegun Henry, who helped me think critically and rediscover my passion for science. I am thankful to my committee members, Prof. Mingda Li for being a mentor and a role model, and Prof. Keith Nelson for identifying so many important scientific questions. I sincerely appreciate Rui Pan and Prof. Hong Lu for their nice superlattice samples. Besides, I want to thank all members of the NanoEngineering group and the ASE group, who helped me a lot during my PhD.

I want to thank my friends for their help and my family for their unconditional love. I am especially grateful to Mengying Wu and my parents, who are always caring and supportive.

Contents

1	Introduction	17
1.1	Phonon transport regimes at nanoscale	22
1.1.1	Characteristic length scales	22
1.1.2	Ballistic-diffusive transport	24
1.1.3	Coherent transport	26
1.1.4	Localized transport	26
1.2	Interface scattering	28
1.2.1	Scattering matrix	29
1.2.2	Nonequilibrium Green's function	31
1.2.3	Interface resistance	32
1.3	Organization of the thesis	33
2	Electron transport across rough interfaces	35
2.1	Introduction	35
2.2	Methodology	37
2.3	Results and discussions	39
2.3.1	Band structures	39
2.3.2	Transmission through a perfect interface	43
2.3.3	Transmission through rough interfaces	47
2.4	Conclusion	53
3	Phonon transport through rough interfaces	55
3.1	Introduction	55

3.2	Methodology	57
3.2.1	Revisiting DMM	57
3.2.2	Mode-resolved atomistic Green's function formalism	58
3.2.3	Continuum modeling	63
3.3	Results and discussions	66
3.4	Conclusion	73
4	Phonon Anderson localization in aperiodic superlattices	75
4.1	Introduction	75
4.2	One-dimensional scalar phonon modeling	76
4.2.1	Formalism	77
4.2.2	Results and discussions	79
4.3	Atomistic Green's function simulation	82
4.4	Experimental validation	87
4.4.1	The sample preparation	87
4.4.2	Frequency-domain thermoreflectance	87
4.5	Conclusion	89
5	Transient thermal grating measurement for thin films	91
5.1	Introduction	91
5.2	Methodology	94
5.2.1	Phase-controlled, heterodyne TTG	94
5.2.2	The heat transfer model for layered medium	96
5.3	Results and discussions	99
5.3.1	Thermal conductivity in correlated oxide thin films	99
5.3.2	Thermal conductivity in digital-alloy superlattices	103
5.4	Conclusion	104
6	Summary and outlook	107
6.1	Summary	107
6.2	Outlook	108

A Green's function for electron transmission	111
A.1 Mode-resolved Green's function formalism for electron transport	111
A.2 Interface atomic mixing	115
B The continuum modeling of diffuse phonon scattering	119
B.1 Formalism	119
B.1.1 The transmission and reflection matrix	119
B.1.2 The Green's function in the continuum limit	122
B.1.3 The ensemble averaged Green's function	127
B.1.4 The transmission and reflection probability matrix	128
B.1.5 The analytical expression of \mathcal{G}^+	129
B.1.6 The specular and diffuse transmittance/reflectance	130
B.2 Numerical calculations	134
B.2.1 The interface scattering transition probability for a rough Si/Ge interface	134
C The transient grating signals for phase gratings	137
C.1 The model	137
C.1.1 General solutions	137
C.1.2 Free surface boundary condition	140
C.1.3 Transfer matrix	142

List of Figures

1-1	Interfaces and nanostructures	19
1-2	The phonon and electron transport through a rough interface	20
1-3	Classical size effect	25
1-4	The wave interferences in disordered systems	28
1-5	The schematic for scattering states	30
2-1	The schematic for Green's function calculation and the transmission processes with conserved and non-conserved transverse momentum . .	38
2-2	The band structures for bulk materials	41
2-3	Surface density of states, transmission function and transmittance .	44
2-4	Energy-resolved transmission function and mode-resolved transmittance	46
2-5	The specific contact resistance for rough and perfect interfaces . . .	51
2-6	The role of the symmetry of the disordered structure in transport . .	52
3-1	Schematic for atomistic Green's function calculation and unfolding .	61
3-2	Angle-resolved diffuse transmittance and reflectance	62
3-3	The diffuse transmittance and reflectance from AGF and cotinuum modeling	64
3-4	The frequency-resolved diffuse and total transmittance and reflectance	65
3-5	The similarity between the diffuse transmittance from one side and the diffuse reflectance from the other side	71
3-6	The dependence of transmission and reflection function on the degree of disorders along perpendicular directions	72

4-1	The schematic for one-dimensional aperiodic structures	77
4-2	The localization length and thermal conductivity in aperiodic layered medium from scalar phonon modeling	81
4-3	The thermal conductivity in aperiodic layered medium versus length with different maximum layer thickness	84
4-4	The comparison between the inelastic phonon mean free path and localization length.	85
4-5	The specular and diffuse thermal conductivity versus length with and without interface roughness	86
4-6	The STEM image for the aperiodic superlattice sample grown on Si substrate using molecular-beam epitaxy	87
4-7	Frequency-domain thermoreflectance signals with different radii	88
4-8	The thermal conductivity measured by FDTR in aperiodic layered medium versus length at different temperatures	89
4-9	The thermal conductivity of different aperiodic samples versus temperature	89
5-1	The snapshots for the temperature distribution in transient thermal grating experiments	93
5-2	The optical configuration for heterodyne detection of transient thermal grating	94
5-3	The electrical conductance for thin films with different crystal orientations	100
5-4	TTG signals and thermal conductivity of V_2O_3 thin films at room temperature	101
5-5	TTG signals at different temperatures	102
5-6	Thermal conductivity of V_2O_3 thin film at various temperatures . . .	102
5-7	Interfacial thermal conductance from FDTR	104
5-8	Thermal conductivity of GaAs/AlAs digital-alloy superlattices with different ErAs fractions	105

A-1	Different configurations for atomic mixing at the interface	117
A-2	The sensitivity of electron transmission on the degree of transverse and longitudinal disorders.	118
B-1	The transmittance and reflectance from continuum modeling	132
B-2	Frequency-resolved transmittance and reflectance from continuum modeling	133

List of Tables

4.1 The Anderson localization length at normal incidence	80
--	----

Chapter 1

Introduction

The miniaturization of electronics has enabled the average number of transistors on a chip to double every 18 months. Nowadays, the characteristic length scales of transistors are well below 10 nm. The phonon and electron transport in nanostructures are fundamentally different from their in their bulk counterparts, as the imperfections, interfaces and boundaries in nanostructures induce strong scatterings and lead to size- and structure-dependent transport. When the characteristic length of the system and the wavelength are comparable, the wave natures of electrons and phonons start to play an important role in transport. In the phonon wave transport regime, interference among scattered waves within the coherence length creates new opportunities in manipulating the phonon transport properties via engineering the structures.

Past studies on the size-dependent transport properties, especially phonon heat conduction, have mostly been based on the classical size effect picture[1, 2]. For an intrinsic bulk material, the phonon mean free path Λ is predominantly determined by the three-phonon scattering lifetime τ via $\Lambda = v_g\tau$, where v_g is the group velocity. In a bulk material, the intrinsic phonon mean free path generally has a wide spectrum. For example, it ranges from the order of 1 nm to the order of 10 μm in bulk Si[3]. In polycrystalline materials with grain sizes at nanoscale, phonons with long intrinsic mean free paths travel ballistically inside the grain[4] and eventually becomes scattered by the boundary. Resultantly, their mean free paths become limited by the grain size. In contrast, phonons with short intrinsic mean free paths travel diffusively

and the effect of boundary scattering is much weaker. The phonon thermal conductivity based on the phonon gas model can be expressed by, $\kappa \propto \frac{1}{3}cv_g\Lambda$, where c is the volumetric specific heat. Therefore, the phonon thermal conductivity decreases with decreasing grain sizes. The size effect in phonon heat conduction manifests itself in other systems. For instance, thermal conductivity decreases with decreasing diameters in nanowires[5] or with decreasing thickness in thin films[6].

The interface scattering is the fundamental reason for the classical size effect. The interface (boundary) scattering rate is often simply taken as $1/\tau_{bd} = \frac{v_g}{L}$ with L being the geometry size, where the angular, wavelength and phase dependence of phonon boundary scattering are entirely neglected[7]. When evaluating the transmittance and reflectance through interfaces, the interface scattering is often considered as diffuse, *i.e.*, the transmittance is isotropic (angle-independent) and the phases of scattered phonon waves are considered completely randomized. In addition to the assumption of diffuse scattering, Swartz and Pohl proposed the famous diffuse mismatch model by further assuming that the transmittance from one side equals to the reflectance from the other side, as they argue that the diffuse phonon scattering makes the phonon lose its memory of origin[8].

In solid-state devices consisting of multiple interfaces such as transistors laser diodes and thermoelectric energy converters, as illustrated in Fig. 1-1, interface scattering is one of the dominating phonon scattering mechanisms and accurately describing the interface scattering is crucial for understanding and engineering the thermal resistance of the device. However, the commonly held assumption of perfectly diffuse boundary scattering and neglecting phonon phase information are questionable. A perfect interface has an effective thickness of one lattice spacing a , which strongly interacts with phonons with wavelength $\lambda \sim a$ (wavevector amplitude $q \sim \frac{2\pi}{a}$). It can scatter phonons with different wavelengths with different scattering strength. Moreover, interface scattering is mostly elastic. After being scattered by such static scattering centers, phonons' phases strictly speaking are not randomized. To properly describe the interface scattering, the wave nature of phonon has to be considered. The interface roughness is a common type of structural disorder in practical devices.

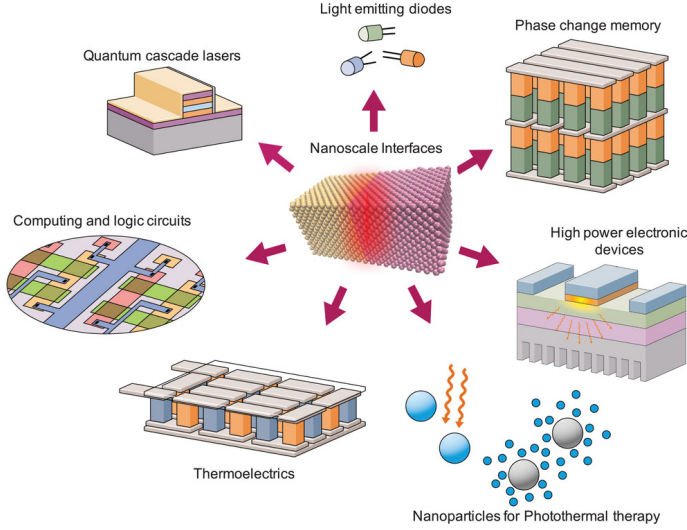


Figure 1-1: Interfacial transport for phonon and electron are important in a variety of applications. Reprinted from Ref. [9].

It broadens the characteristic width of interface from a to a larger value δ , which changes how the interface scattering explicitly depends on the wavelength, as shown in Fig. 1-2. The existence of multiple interfaces further complicates the superposition of scattered phonon waves.

The interface also scatters electrons and induces a large interface resistance[10]. Similar to the phonon interface scattering, the wave properties of electrons must be included when studying the electron interface scattering, as the characteristic length scale of the interface is comparable to electron wavelengths. Therefore, studying the interface scattering for phonons and electrons are both of great significance. What's more, resolving how the interface roughness impacts the interface scattering for phonon and electron is necessary to understand the interfacial transport in practical devices.

Elastic phonon scattering at a single interface maintains the phase (*i.e.*, the way phase evolves with time keeps unchanged). For multiple interfaces, *e.g.*, in superlattices, the reflected and transmitted waves at each interface interfere with each other. The interference can alter the phonon eigenvectors (*i.e.*, how each atom vibrates according to a vibrational normal mode) and lead to a different phonon dispersion relation from the bulk material. Although phonon is always partially reflected by a

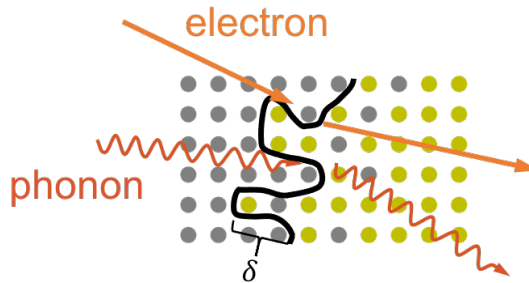


Figure 1-2: The phonon and electron transport through a rough interface. The interface roughness has a characteristic width δ .

single interface, phonon interference in superlattices consisting of multiple interfaces gives rise to passing bands (phonon traveling through interface without interface scattering) and stop bands (phonon propagation is forbidden)[11, 12]. On the other hand, the inelastic scattering, such as three-phonon scattering, can destroy the interferences. In particular, when the inelastic mean free path Λ_{in} is much larger than the phonon coherence length l_c , which is the characteristic length scale for phonon interferences, the phonon coherence is maintained even after multiple elastic scattering events.

Experimentally, coherent phonon heat conduction, where the phonon keeps its phase information in the transport process, has been observed in GaAs/AlAs superlattices with changing number of periods and fixed period length[13]. Below 150 K, the mean free paths for most phonons are found to be much larger than the sample length. As a result, the phonon wave travels coherently from one side to the other side and its phase is maintained. At higher temperatures, the phonon mean free paths are reduced and the fraction for diffusive phonons increases. The thermal transport in this case is partially coherent. The coherent phonon transport in superlattices suggests that phonon interference is crucial in determining the transport property.

The gapped phonon states (inside stop bands) in superlattices due to interference are intrinsically localized (evanescent waves with imaginary wavevectors) thus do not directly contribute to transport. When introducing disorders to the nanostructures, another type of localization can be induced by phonon interferences, called Anderson localization. Unlike in periodic superlattices, the interfering wave components in disordered system do not have any spatial periodicity. Additionally, the effective

transmittance for an incident phonon decays exponentially with length. Anderson localization was first found in Anderson's seminal work in 1958[14]. It has been experimentally found in photonic[15], electronic[16], acoustics[17], cold-atom systems[18]. However, the phonon Anderson localization is much less studied experimentally due to the broadband nature and three-dimensional transport of phonons.

Recently, signatures of phonon Anderson localization has been found in GaAs/AlAs superlattice with random dots inserted at the interfaces[19]. The interface roughness strongly scatters short-wavelength phonons, which makes them minimally contribute to the transport. The random dots scatter phonons with middle and long wavelengths and the interferences among the scattered waves causes exponentially decaying transmittance with the sample length. Accordingly, the thermal conductivity decreases with sample length below 50 K. The transmittance is the squared amplitudes of the summation of all possible scattering waves (complex quantities). As the disordered system become longer, although the number of possible scattering paths for a phonon to propagate from one side to the other side of the sample increases rapidly, the transmittance is not necessarily increasing as the summation of scattered waves can be either positive or negative. On the other hand, for any forward scattering path, its time-reversal path is also a possible scattering path. Together, two time-reversal paths form constructive interference, and along the combined path the phonon travels back to exactly where it starts, *i.e.*, the phonon wave is spatially localized. It turns out that as the system length increases, it is always easier to find interfering paths that make phonon circle back than the paths that let phonon travel through the sample[20]. Consequently, the transmittance becomes smaller with longer sample length. The phonon Anderson localization provides a new way to manipulate phonons, which can be useful in low-thermal-conductivity applications such as thermoelectrics, as well as in quantum information science to prevent phonon from interacting with spin and causing quantum decoherence[21]. However, there is no report on phonon Anderson localization at moderate temperatures, which greatly limits the applications of Anderson localization.

From above-mentioned examples, we clearly see that the geometry of the struc-

tures has a great impact both on phonon and electron transport, which also creates new opportunities to manipulate phonon and electron transport via structural engineering. The classical size effect without invoking the wave effect describes the size-dependent transport when phases are fully randomized by interface scattering. However, for phonon and electron transport through interfaces and disordered structures, the wave effect plays a significant role. The lacking understanding of how the interface roughness impacts the phonon and electron transport substantially limits the possibilities of improving phonon and electron transport. Furthermore, for phonon transport through disordered structures, the phases of phonon waves cannot be overlooked. The interferences among scattered waves in disordered structures causes phonon Anderson localization. The Anderson localization provides a new approach to manipulate phonons using disorders, yet has only been achieved at extremely low temperatures. To make Anderson localization a practical strategy to control phonons, more structural design and experimental tests are needed to push up the temperature needed to achieve phonon Anderson localization.

This thesis focuses on the interplay between structural randomness and the wave properties of phonon and electron, including wavelengths, phases, interferences. It provides the practical strategies to engineer phonon and electron wave transport using randomness via mode-resolved Green's function calculations and pump-probe optical characterizations.

1.1 Phonon transport regimes at nanoscale

Several important characteristic length scales divide the phonon transport regimes into ballistic-diffusive transport regime, coherent transport regime and localized transport regime. We will introduce those length scales in the following.

1.1.1 Characteristic length scales

In the transport process, phonon propagation is accompanied by various types of scatterings. The elastic scattering processes that conserve incident phonon's energy

include impurity scattering, alloy scattering, interface scattering, boundary scattering *etc..* In contrast, the inelastic scattering processes that do not conserve the phonon energy include three-phonon scattering, phonon-electron scattering, *etc..* In a system where multiple scattering mechanisms coexist, the total scattering rate can be evaluated by invoking the Matthiessen's rule, which states that the total scattering rate is the summation of all types of scattering rates expressed by $\frac{1}{\tau} = \frac{1}{\tau_{\text{impurity}}} + \frac{1}{\tau_{\text{alloy}}} + \dots$. Note that the phonon phases and phonon interferences are entirely neglected in this treatment.

The phonon mean free path Λ describe the average traveling distance between two consecutive scattering events. Specifically, the elastic scattering mean free path $\Lambda_e = v_g \tau_e$ and the inelastic scattering mean free path $\Lambda_{\text{in}} = v_g \tau_{\text{in}}$ are determined by the elastic and inelastic scattering lifetime, respectively. The recent process in first-principle calculation of the phonon mean free paths has provided a reliable way to acquire the inelastic phonon mean free path[22, 3, 23] and elastic phonon mean free path accurately[24, 25, 26, 27].

For an inelastic scattering process, such as three-phonon interaction (two phonons scatter and emit a new phonon or one phonon emits two new phonons), the phonons are annihilated or created, and hence their phase information is completely destroyed after one scattering event. The coherence length l_c is defined to describe the distance within which the temporal behavior of phonon phases remains the same. The Thouless length is used as a measure of coherence length for electron transport, where $l_c = (D \tau_{\text{in}})^{1/2}$ and D is the diffusivity[28, 29]. For phonon transport, we have $D = \frac{v_g \Lambda}{3}$, where Λ is the phonon mean free path that incorporate all types of scattering processes and satisfies, $\Lambda^{-1} = \Lambda_e^{-1} + \Lambda_{\text{in}}^{-1}$. Therefore, the phonon coherence length can be obtained by, $l_c = \sqrt{\Lambda \Lambda_{\text{in}} / 3}$ [2]. For a system with strong inelastic scattering ($\Lambda_{\text{in}} \ll \Lambda_e$), we have $l_c \approx \Lambda_{\text{in}} / \sqrt{3} \ll \Lambda_e$, whereas for a system with strong elastic scattering ($\Lambda_{\text{in}} \gg \Lambda_e$), we have $l_c \approx \sqrt{\Lambda_e \Lambda_{\text{in}} / 3} \gg \Lambda_e$. That is to say, in elastic scattering dominated system, phonons can maintain their coherence even far beyond the mean free path, as the elastic scattering generally only partially destroys the phase information of phonons.

1.1.2 Ballistic-diffusive transport

The phonon thermal conductivity $\kappa = G \cdot L$, where G is the thermal conductance and L is the total length. According to the Landauer-Büttiker formalism[10], the phonon thermal conductance can be defined by,

$$G = \frac{1}{2\pi A} \int_0^\infty \hbar\omega \Theta(\omega) \frac{\partial f_{\text{BE}}}{\partial T} d\omega \quad (1.1)$$

where A is the cross-sectional area, $\Theta(\omega) = \frac{1}{N_{\mathbf{k}\parallel}} \sum_{\mathbf{k}\parallel} \text{tr}(\mathbf{t}^\dagger(\omega, \mathbf{k}\parallel) \mathbf{t}(\omega, \mathbf{k}\parallel))$ is the phonon transmission function, which describes the number of phonon conducting channels at given frequency ω , $\mathbf{t}(\omega, \mathbf{k}\parallel)$ is the phonon transmission matrix at given transverse momentum $\mathbf{k}\parallel$ and f_{BE} is the Bose-Einstein distribution function. The Landauer-Büttiker formalism suggests that the conductance is intimately related to the transmission function $\Theta(\omega)$ [30].

If we assume the phonon transmission function is frequency-independent $\Theta(\omega) = \Theta \cdot \tau$, where Θ is the average transmission function when all transmission channels have unity transmission probability and τ is a constant transmission probability (transmittance). We have the conductance directly proportional to the transmittance $G \propto \tau$. Consider the transport across a short sample with length l . We denote the transmission from one side to the other side of this sample τ_1 . If we double the length of the sample and neglect any coherence effect on changing the transmittance, it is intuitive to think that the effective transmittance is simply $\tau_1 \times \tau_1$. However, such expression is actually wrong as the multiple scattering process is ignored. The transmittance through the sample with length $2l$ should be,

$$\tau_2 = \tau_1 \tau_1 + \tau_1 (1 - \tau_1)^2 \tau_1 + \dots = \frac{\tau_1^2}{1 - (1 - \tau_1)^2} \quad (1.2)$$

One can further generalize to the sample with length Nl ,

$$\tau_N = \frac{1}{1 + N^{\frac{1-\tau_1}{\tau_1}}} \quad (1.3)$$

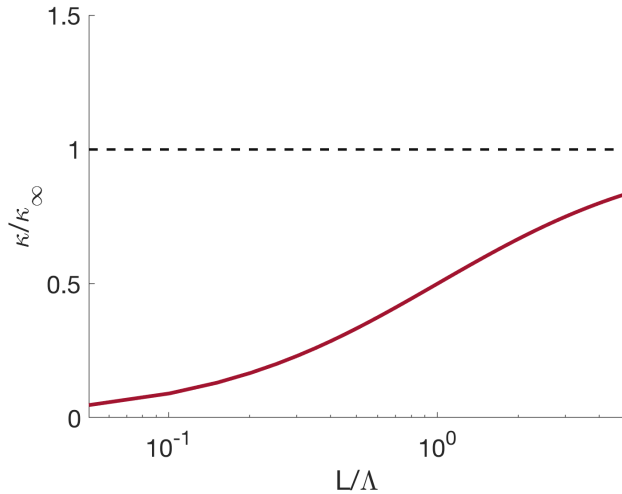


Figure 1-3: The length dependence of thermal conductivity in ballistic-diffusive transport regime.

The thermal conductivity of samples with length $L = Nl$ can then be expressed by,

$$\kappa \propto \tau_N \cdot L = \frac{\Lambda L}{\Lambda + L} \quad (1.4)$$

where $\Lambda = \frac{\tau_1}{1-\tau_1} \cdot l$ is the phonon mean free path. When $L \gg \Lambda$, the thermal conductivity converges to a constant bulk value and the phonon transport is diffusive. On the other hand, when $L \ll \Lambda$, the thermal conductivity $\kappa \propto L$ and the phonon transport is ballistic. In Fig. 1-3, we present the size dependence of the thermal conductivity κ , where the thermal conductivity always increases with the system size. The size dependence given by Eq. 1.4 is one example of classical size effect. Such transport regime is called ballistic-diffusive transport.

The classical size effect based on the phonon particle picture has already been widely studied. In this thesis, we are more interested in studying wave effect on transport, which is much less explored. In the above analysis, the wave nature of phonon is entirely overlooked, as we have explicitly assumed the that phonon transport is incoherent, where after scattering phonons lost information about its previous paths and such behavior can be regarded as random walk. One can also make analogy to ray tracing in optics to understand the incoherent phonon transport[31].

1.1.3 Coherent transport

The phonon transport is coherent within the coherence length. The reasons why coherent phonon transport has been mostly observed in short-period superlattices[13, 32] are as follows. At low temperatures, the elastic scattering dominates over the inelastic scattering, which makes coherence length $\Lambda < l_c < \Lambda_{\text{in}}$. The short-wave-length phonons are strongly scattered by the interface disorders as the mass-disorder scattering rate $\propto \omega^4$ [33], while the long-wave-length phonons can travel across all interfaces rather than being diffusively scattered by interfaces and losing their phases[13, 32]. As a result, phonon can travel coherently from one side to the other side of the sample. The transmittance remains a constant and so does the thermal conductance. Hence, the thermal conductivity linearly increases with the total length, $\kappa \propto L$.

One might argue that this is just the small L limit in the classical ballistic-diffusive transport (or simply the ballistic limit) given by Eq. 1.4. However, the classical ballistic-diffusive transport assumes that phonon loses its phase entirely beyond the length l ($l \geq l_c$). The classical ballistic-diffusive picture cannot properly describe the transport below l (or below l_c), where the coherence is important. Beyond the length l , the transport is fully incoherent, as the phase are completely randomized due to multiple elastic scatterings and inelastic scatterings. On average phonon interference has a negligible impact on transport.

At higher temperatures, the coherence length decreases due to reduced inelastic mean free path Λ_{in} (three-phonon scattering rate $\propto T$), the coherent transport gradually disappears. It is worth mentioning that accurate calculation of coherence length is lacking thus it is difficulty to know exactly when the phonon phases and interferences can be neglected. To summarize, we can call the transport coherent within the coherence length l_c .

1.1.4 Localized transport

When introducing random disorders into the short-period superlattices, as realized in the experimental work by Luckyanova *et. al.*[19], the disorders not only strongly

scatter phonons but induce strong interferences among the scattered waves. Consider the transport from A to B inside a superlattice with doped random dots at interfaces, as shown in the Fig. 1-4 (a). The calculation of probability needs to include all possible scattering paths. For simplicity, we assume there are only two possible paths and the transport is one-dimensional¹. The probability of transition from A to B can be expressed by,

$$\begin{aligned} P_{A \rightarrow B} &= |u_1 + u_2|^2 \\ &= \underbrace{P_1 + P_2}_{\text{classical}} + \underbrace{2\sqrt{P_1 P_2} \cos(kL_1 - kL_2)}_{\text{interference}} \end{aligned} \quad (1.5)$$

The first term describes the classical random work paths, which are additive. The second term describes the contribution from interference between different scattering paths. In the incoherent transport regime discussed in Session 1.1.2, the interference term does not contribute much. However, when the inelastic effect is weaker, the interference term contributes more to the transport.

The probability of returning to the point A, $P_{A \rightarrow A}$, is also related to the summation of all possible paths. The random disorders usually cause stronger enhancement of the probability of coming back, known as the coherent backscattering[34]. If the degree of disorder is even larger, there are paths that form loops and contribute substantially in $P_{A \rightarrow A}$. In certain cases, the two possible paths are time-reversal to each other, and they form constructive interference. Resultantly, we have the reflectance of unity,

$$\begin{aligned} P_{A \rightarrow A} &= |u_1 + u_2|^2 \\ &= \frac{1}{4} \cdot |e^{ikL} + e^{-ikL}| \\ &= 1 \end{aligned} \quad (1.6)$$

as $L = 0$. In other words, the wave is localized.

The Fig. 1-4 (b) describes an extreme case of localization. Generally, the reflectance quickly increases with the increasing system length, whereas the transmit-

¹As shown in the Fig. 1-4, the actual scattering paths are not one-dimensional. For simple mathematical demonstration, we assume all waves are plane waves moving along one dimension.

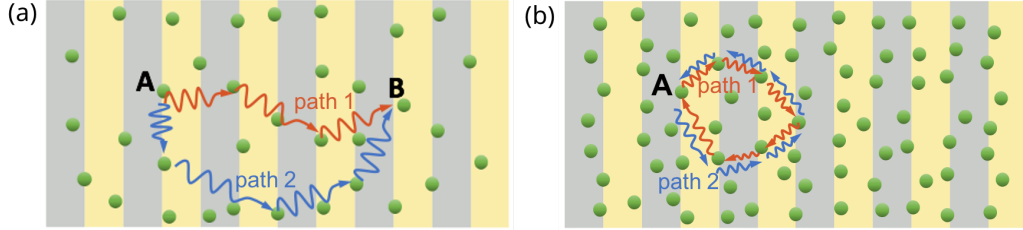


Figure 1-4: (a) The random dots in the weak-disorder regime causes interferences among scattered waves, which enhances chances of reflecting back, known as coherent backscattering. (b) The random dots in the strong-disorder causes stronger interference. The two time-reversal paths make the phonon stays where it starts and cannot propagate, known as Anderson localization.

tance behaves in the opposite way. In the localized transport regime, the transmission function is exponentially decaying with system length $\Theta(\omega) \propto e^{-L/\zeta}$, where ζ is the decay length. As a consequence, the thermal conductivity satisfies,

$$\kappa \propto L e^{-L/\zeta} \quad (1.7)$$

which peaks at $L = \zeta$. Such length dependence of thermal conductivity is a unique feature of Anderson localization. The Anderson localization of phonons is an emerging phenomenon due to wave interferences and provides new directions in controlling phonon dynamics.

1.2 Interface scattering

The interface scatterings for phonon and electron are significantly affecting the phonon and electron transport. At the interface, the incident electron/phonon can be transmitted or reflected. Scattering matrix is often used to describe the probability for different interface scattering processes. The nonequilibrium Green's function calculation can be used to obtain the scattering matrix and the interface conductance for phonon and electron[35].

1.2.1 Scattering matrix

We consider the scattering matrix for electron as an example and the scattering matrix for phonon can be analogously defined. Denote $u_L(+)$ and $u_R(+)$ the forward propagating state from the left side and the right side, respectively. As depicted in Fig. 1-5, due to the scattering of the interface, the wavefunction of left side becomes,

$$c_L = u_L(+) + \mathcal{R}u_L(-) \quad (1.8)$$

and the propagating modes in right side can be expressed by,

$$c_R = \mathcal{T}u_R(+) \quad (1.9)$$

where the matrix \mathcal{R} and \mathcal{T} are the generalized reflection and transmission matrix. The physical transmission and reflection matrices are obtained by normalizing these matrices according to the current normal to the interface,

$$t_{RL,ji} = \sqrt{\frac{v_{R,z,j}a_L}{v_{L,z,i}a_R}}\mathcal{T}_{ji} \quad (1.10)$$

$$r_{LL,ji} = \sqrt{\frac{v_{L,z,j}}{v_{L,z,i}}}\mathcal{R}_{ji} \quad (1.11)$$

The transmission/reflection matrix element describes the ratio between the transmitted/reflected current of mode j and the incident current of mode i , both along the interface normal. Note that the lattice constant along z direction is used to compute the current for each mode, which is proportional to the velocity divided by the unit-cell volume. In the following, we use the physical transmission and reflection matrix to study the transmission and reflection probability. The scattering matrix S that describes the all scattering processes at an interface can be expressed by,

$$S = \begin{pmatrix} r_{LL} & t_{LR} \\ t_{RL} & r_{RR} \end{pmatrix}. \quad (1.12)$$

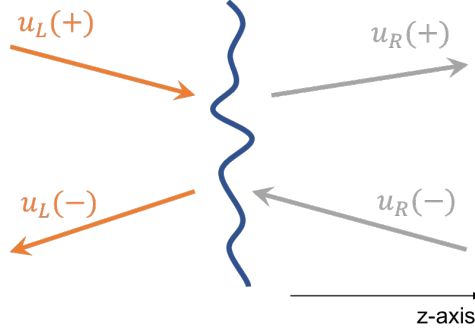


Figure 1-5: The schematic for scattering states for an interface scattering problem.

With the help of the scattering matrix, the incoming and outgoing states normalized by current are simply related via, $u_{\text{out}} = S u_{\text{in}}$.

In particular, the transmission matrix element $t_{RL,ji}$ is proportional to the Green's function element $G_{ji} = \langle u_j | \hat{G} | u_i \rangle$, where $\hat{G} = (E - \hat{H} + i\eta)^{-1}$ is the Green's function operator, \hat{H} is the Hamiltonian operator, $|u_i\rangle$ and $|u_j\rangle$ are the wavefunctions for incident and transmitted electron in bra-ket notation (for phonon transport, $|u_i\rangle$ and $|u_j\rangle$ are the phonon eigenvectors). For a perfect interface, the transverse momentum is conserved $\mathbf{k}_{i,\parallel} = \mathbf{k}_{j,\parallel}$ and the scattering process is called specular transmission. However, when interface disorders are introduced, such momentum conservation law is no longer valid and the scattering process when $\mathbf{k}_{i,\parallel} \neq \mathbf{k}_{j,\parallel}$ is called nonspecular (diffuse) transmission.

The nonspecular transmission can enhance the transmittance for phonon and electron. For instance, consider the phonon transport across a perfect interface with large mismatch. The critical cone for transmission, *i.e.*, the surface in the phonon dispersion relations that separates the completely reflected phonon states and other phonon states, is very narrow and phonon cannot escape outside the critical cone. With interface disorders added, the phonon are allowed escape outside the critical cone via nonspecular transmission, which largely enhances the total transmittance. In this case, the disorders can actually reduce the interface resistance. Understanding how the disordered structure determines the nonspecular transmittance can offer new opportunities in optimizing the interfacial transport.

1.2.2 Nonequilibrium Green's function

Due to the intimate relation between the transmission matrix and the Green's function, nonequilibrium Green's function has been commonly used to study the phonon and electron transport through interfaces[36, 37]. We introduce the nonequilibrium Green's function formalism for electron transport in the following and the formalism for phonon transport can be similarly derived. The Green's function method is a nonperturbative approach capable of both weak-disorder and strong-disorder cases. Also, it intrinsically incorporates all wave effects, which is important for the interface scattering problem. The Green's function for Schrödinger equation is defined to satisfy the following equation²,

$$[(E + i\eta) I - H(\mathbf{k}_{\parallel})] G(E, \mathbf{k}_{\parallel}) = I \quad (1.13)$$

where $H(\mathbf{k}_{\parallel})$ is the Hamiltonian matrix, η is an infinitesimal real number and I is the identity matrix. The Hamiltonian consists of three parts, left lead, device region and right lead, where the two leads are essentially two reservoirs of electrons and the electron travel between two reservoirs through the device region. In block-wise form, the Hamiltonian matrix reads,

$$H(\mathbf{k}_{\parallel}) = \begin{pmatrix} H_L + \Sigma_L & H_{LC} & 0 \\ H_{CL} & H_C & H_{CR} \\ 0 & H_{RC} & H_R + \Sigma_R \end{pmatrix} \quad (1.14)$$

where Σ_L and Σ_R are self-energies for two lead regions. The transmission function at given \mathbf{k}_{\parallel} , a measure of number of conducting channels, is given by,

$$\Theta(E, \mathbf{k}_{\parallel}) = \text{tr} [\Gamma_L(E, \mathbf{k}_{\parallel}) G(E, \mathbf{k}_{\parallel}) \Gamma_R(E, \mathbf{k}_{\parallel}) G^\dagger(E, \mathbf{k}_{\parallel})] \quad (1.15)$$

where $\Gamma_R(E, \mathbf{k}_{\parallel})$ and $\Gamma_L(E, \mathbf{k}_{\parallel})$ are coupling matrices related to the self-energies.

²We take electron transport for example and phonon transport can be similarly defined, except that E becomes ω^2 .

The conductance can be obtained by the Landauer-Büttiker formalism[35],

$$G = -\frac{2e^2}{hA} \int \Theta(E) \frac{\partial f_{\text{FD}}}{\partial E} dE \quad (1.16)$$

where $\Theta(E) = \frac{1}{N_{\mathbf{k}_{\parallel}}} \sum_{\mathbf{k}_{\parallel}} \Theta(E, \mathbf{k}_{\parallel})$ is the transmission function and f_{FD} is the Fermi-Dirac distribution function. The spin degree of freedom is multiplied (no spin-orbital coupling). Conventionally, $G_0 = \frac{2e^2}{h}$ is called the conductance quantum.

1.2.3 Interface resistance

The electrical interface resistance is the ratio between the electrochemical potential difference and the current,

$$R = \frac{\Delta\Phi}{I} \quad (1.17)$$

Note that the conductance given by Landauer-Büttiker formalism (Eq. 1.16) cannot be directly used to compute the interface resistance. The reasons are as follows. Consider a perfect bulk material with an imagined plane as an interface. The expected interface resistance associated with the imaginary interface should be zero. However, directly using Eq. 1.16 will give a finite value of interface resistance. This is because Eq. 1.16 describes the conductance for the transport between two reservoirs that are at different equilibrium state and have well-defined electrochemical potential, which is conventionally regarded as a two-probe setup. However, near the interface, due to the strong interface scattering, the electrons are far from equilibrium. For example, on the left side of the interface, the right-moving electrons are those out of the left reservoir (left lead), while the left-moving electrons can be those reflected by the interface or those transmitted from the right reservoir (right lead). As a result, the electrochemical potential cannot be rigorously defined near the interface. Nevertheless, we can still compute the effective electrochemical potential by assuming that the local electron population follows a Fermi-Dirac distribution.

The effective electrochemical potential energy on the left and right side of the

interface μ_1 and μ_2 are,

$$\begin{aligned}\mu_1 &= \mu_L - (\mu_L - \mu_R) \frac{G}{2g_L} \\ \mu_2 &= \mu_R + (\mu_L - \mu_R) \frac{G}{2g_R}\end{aligned}\tag{1.18}$$

where μ_L and μ_R are the electrochemical potential energies for the left and right reservoir, which satisfy the relation $\mu_L - \mu_R = |e|\Delta\Phi$, e is the elementary charge for electron, and g_L and g_R are the conductance for bulk materials. The conductance between μ_1 and μ_2 is then expressed by,

$$G_4 = \left[\frac{1}{G} - \frac{1}{2} \left(\frac{1}{g_L} + \frac{1}{g_R} \right) \right]^{-1}\tag{1.19}$$

which is also called the four-probe conductance. The interface resistance can be expressed by,

$$R = \frac{1}{G_4}\tag{1.20}$$

In the limit of perfect transmission and two sides made of same type of material, the resistance $[G_4]^{-1}$ is zero, which is as expected. In the limit of low temperature and considering the same materials for two leads, the conductance reduces to the famous Landauer formula[10],

$$G_4 = \frac{2e^2}{hA} \frac{\Theta(E_f)}{\Theta_{\text{bulk}}(E_f) - \Theta(E_f)}\tag{1.21}$$

where $\Theta_{\text{bulk}}(E_f)$ is the transmission function with unity transmittance for the bulk material in the leads. For phonon transport, the four-probe conductance can be similarly computed to Eq. 1.19 by considering the effective local temperatures instead of the electrochemical potential energy near the interface[38].

1.3 Organization of the thesis

This thesis essentially has three parts. The first part contains the practical strategy to reduce the interface resistance for electrons and phonons using disorders. In the second part, the aperiodicity is studied as a strategy to induce phonon Anderson

localization, both computationally and experimentally. In the last part, an optical method for measuring thermal transport properties of nanostructures are presented.

In Chapter 2 and Chapter 3, we study the mode-resolved interface scattering for electrons and phonons. In Chapter 2, we present the method to compute the specular and nonspecular transmission through rough interfaces. In particular, we examine the role of wavevectors and symmetries of Bloch wavefunctions in assisting or hindering the electron transport. We also identify the specific type of disordered structures that reduce the contact resistance the most.

In Chapter 3, we apply the mode-resolved atomistic Green's function to study diffuse phonon scattering. Specifically, we examine the famous model for thermal boundary resistance, the diffuse mismatch model and the physical assumptions behind it. In addition, we clarify the competing roles of specular and diffuse transmission and reflection in determining the thermal boundary resistance. In Chapter 3, we also lay the foundation of the computational schemes to study phonon transport in nanostructures.

In Chapter 4, we study the phonon transport in aperiodic layered media computationally and identify Anderson localization of phonons. We then use frequency-domain thermorelectance to experimentally measure the length dependence of thermal conductivity of aperiodic superlattices and confirm the existence of phonon Anderson localization up to 200 K. Our findings provides a practical way to engineer phonon transport using aperiodicity.

In Chapter 5, we present an experimental method using transient thermal grating to measure the thermal conductivity of thin film and the thermal boundary resistance. Such method serves as a good alternative method of measuring the thermal transport in nanoscale thin films to other conventional optical characterization methods.

Last but not least, in Chapter 6, we present a summary and an outlook for future directions of studying and engineering phonon and electron transport in nanostructures.

Chapter 2

Electron transport across rough interfaces

2.1 Introduction

The importance of interfaces in advanced semiconductor devices has been clearly pointed out by Herbert Kroemer with his famous statement, “the interface is the device”[39]. Semiconductor heterostructures play essential roles in vertical-cavity surface-emitting lasers[40, 41, 42], heterostructure bipolar transistors[43, 44], quantum cascade lasers[45], quantum well infrared photodetectors[46], thermionic micro-coolers[47, 48], bipolar transistors[49], spin qubit devices[50, 51], thermoelectric power generators[52, 53, 54, 55], *etc.* However, the interfaces in heterostructures strongly scatter electrons and cause the contact resistance[10, 56, 38, 57]. The interface scattering probabilities are not only determined by the intrinsic properties of bulk materials, but by the non-intrinsic properties such as the interface structures. Specifically, the interface roughness due to atomic mixing[58], as a common type of interface disorder, alters the contact resistance. In order to design proper interface structures that minimize interfacial resistance, it is crucial to understand how the atomic mixing affects electron scattering at interfaces.

The nonequilibrium Green’s function (NEGF) is often used to describe the structure-dependent charge transport[35]. Many works using NEGF combined with Landauer

formula for conductance are conducted to study the transport across molecular junctions[59, 60, 61, 62], nanotransistors[36, 63], grain boundaries in two-dimensional materials[64], metal-semiconductor interfaces[65, 66], metal-metal interfaces in magnetic multilayers [67, 68, 69, 70] and semiconductor interfaces[71, 72]. In particular, Bellotti *et al.* investigated the carrier transport through semiconductor interfaces in the presence of positional and compositional disorders using NEGF and found that the disorder significantly impedes the coherent propagation of carriers through multiple interfaces[71]. Tibaldi *et al.* performed a large-scale NEGF calculation of the carrier transport in a realistic tunnel junctions for vertical-cavity surface-emitting lasers and achieved a good agreement with experimental $I - V$ curve. However, the interface roughness in the transverse directions is neglected in these works, as the computational cost of NEGF increases dramatically with the cross-section areas of the interface. Besides NEGF calculation, Daryoosh *et al.* used a simple effective mass model to study the carrier transport through barriers in metal-based superlattices and found that the nonspecular (diffuse) scattering can greatly boost the thermoelectric figure of merit zT [55]. Los studied how the transmission probability varies with the average fluctuations of potential energies due to interface disorders under the effective mass approximation[73]. However, the effective mass approximation adopted in these works can poorly describe practical semiconductors with band pockets not at zone center. Due to the multi-valley nature[53] of the band structures of semiconductors, new physics shall emerge for electron interfacial transport.

In this Chapter, we apply the mode-resolved Green's function formalism with tight-binding Hamiltonian to study charge transport across perfect and rough interfaces due to atomic mixing. In particular, we take advantage of the transverse translational symmetry to reduce the computational cost of surface Green's function. The tight-binding Hamiltonian makes sure the multiple carrier pockets in the Brillouin zone are properly described. We vary the degree of disorders in transverse directions and perpendicular direction and study the specular and nonspecular interface scattering processes with mode resolution. Moreover, we unveil the roles of disorders and symmetries in assisting nonspecular transmission. We show that over

one order of magnitude of reduction of the specific contact resistance can be achieved by the interfacial atomic mixing.

2.2 Methodology

In the Green's function calculation, we first divide the system into three regions, two semi-infinite lead regions and a device region, as depicted in Fig. 2-1 (a). The repeated cells along z direction in the lead region are indexed by 0, 1, ... and the period length is $a_{z,\alpha}$ with $\alpha = x, y$. The whole supercell structure is periodic along directions parallel to the interface. Inside the lead region, there are $N_{uc,x} \times N_{uc,y}$ identical unitcells along the transverse directions. The transverse lattice vector for the supercell is $\mathbf{R}_{sc,\alpha} = N_{uc,\beta} \mathbf{R}_{uc,\beta}$ with $\beta = x, y$, where $\mathbf{R}_{uc,\beta}$ is the transverse lattice vector for the unitcell. As a result, the transverse momentum in the supercell representation can be uniquely unfolded in a momentum defined in the unitcell representation, as elucidated in Fig. 2-1 (b). The unfolded momentum can be expressed by,

$$\mathbf{k}_{uc,\parallel} = \mathbf{k}_{sc,\parallel} + a\mathbf{G}_{sc,x} + b\mathbf{G}_{sc,y} \quad (2.1)$$

where a and b are integers to be determined. Finding the correct pair of a and b is known as an unfolding problem and we use the unfolding scheme by Popescu and Zunger[74] to resolve the correct $\mathbf{k}_{uc,\parallel}$.

We consider the elastic interface scattering limit, where the energy E of the incident electron is conserved. In addition, the in-plane translational symmetry of the supercell dictates that the transverse momentum $\mathbf{k}_{sc,\parallel}$ must be conserved during an interface scattering event. When the device region contains a perfect interface with the same in-plane periodicity as the lead region, the transverse momentum $\mathbf{k}_{uc,\parallel}$ is conserved. However, when the device region consists of a rough interface, $\mathbf{k}_{uc,\parallel}$ is not always conserved. This is because the interface roughness breaks the internal transverse translational symmetry within the supercell and $\mathbf{k}_{sc,\parallel}$ can be unfolded into different $\mathbf{k}_{uc,\parallel}$ for the incident state and the transmitted state. As illustrated in

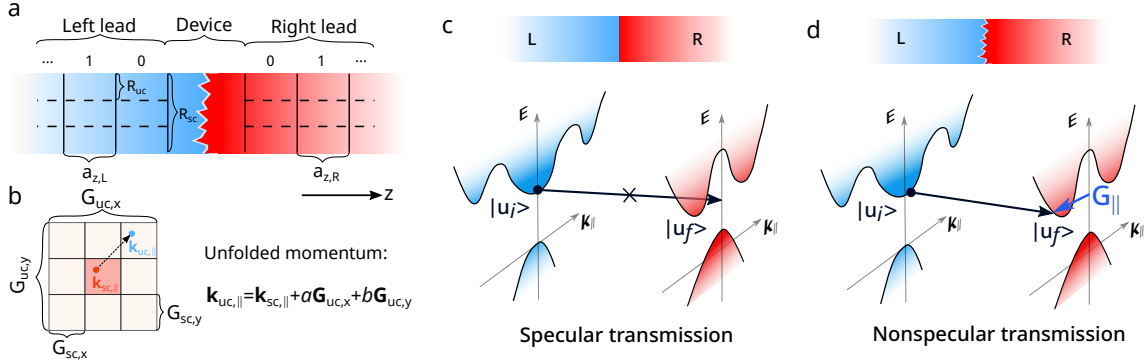


Figure 2-1: (a) The partitioning for Green’s function calculation with repeated unitcell in the lead region being numbered with 0, 1 (b) The transverse momentum conservation law and how the transverse momenta in the unitcell representation and the supercell representation are related. (c) Specular transmission process through a perfect interface where the transverse momentum is conserved, $\mathbf{k}_{i,||} = \mathbf{k}_{f,||}$. (d) Nonspecular transmission processes through a disordered interface, where $\mathbf{k}_{i,||} = \mathbf{k}_{f,||} + m\mathbf{G}_x + n\mathbf{G}_y$, allows the scattering between valleys with different $\mathbf{k}_{||}$.

Fig. 2-1 (c), for a perfect interface, $\mathbf{k}_{uc,||}$ is conserved, and we denote this type of scattering process the specular transmission. For a rough interface shown in Fig. 2-1 (d), $\mathbf{k}_{uc,||}$ can be either conserved or nonconserved. Particularly, we denote the scattering process with nonconserved $\mathbf{k}_{uc,||}$ the nonspecular transmission.

We define the transmission probability matrix from the left side $T_{ji}(E, \mathbf{k}_{sc,||})$ as the ratio between the normal current of the transmitted state j to the incident state i . Formally, we can express the specular and nonspecular transmission probability matrix with,

$$\begin{cases} T_{s,ji}(E, \mathbf{k}_{sc,||}) = T_{ji}(E, \mathbf{k}_{sc,||}), & \text{when } \mathbf{k}_{uc,||,j} = \mathbf{k}_{uc,||,i} \\ T_{ns,ji}(E, \mathbf{k}_{sc,||}) = T_{ji}(E, \mathbf{k}_{sc,||}), & \text{when } \mathbf{k}_{uc,||,j} \neq \mathbf{k}_{uc,||,i} \end{cases} \quad (2.2)$$

The elements of the transmission probability matrix from the left side is given by,

$$T_{ji}(E, \mathbf{k}_{sc,||}) = |t_{RL,ji}(E, \mathbf{k}_{sc,||})|^2 \quad (2.3)$$

where the transmission matrix $t_{RL,ji}(E, \mathbf{k}_{\text{sc},\parallel})$ is related to the Green's function[75],

$$t_{RL}(E, \mathbf{k}_{\text{sc},\parallel}) = i\sqrt{V_R^r}[U_R^r]^{-1}G_{N+1,0}[U_L^{a\dagger}]^{-1}\sqrt{V_L^a} \quad (2.4)$$

The formal definitions and detailed calculations of the velocity matrices $V_{R/L}^{r/a}$, eigenvector matrices $U_{R/L}^{r/a}$ and Green's function $G_{N+1,0}$ can be found in the Appendix A. Note that the calculation of the velocity matrices and eigenvector matrices require the surface Green's function $g_{L/R}^{a/r}(E, \mathbf{k}_{\text{sc},\parallel})$. We apply the Fourier transform to the Hamiltonian to obtain the block-diagonal surface Green's function. Then, we apply the inverse Fourier transform to obtain the surface Green's function. These procedures allow us to invert small matrix multiple times rather than directly inverting the large matrix, which greatly boosts the computational efficiency. The detailed implementation can be found in Ref. [76].

2.3 Results and discussions

2.3.1 Band structures

We study the [001] Si/Ge interface as it is a classical semiconductor interface used in a wide range of applications such as quantum information storage[51], strained field-effect transistors[?, ?] and thermoelectrics[77, 53]. To start with, we examine the bands structures for Si and Ge individually. We use $sp^3d^5s^*$ Slater-Koster tight-binding model[78, 79] to construct the Hamiltonian, with hopping integral parameterizations from Niquet *et al*[80]. More specifically, the hopping integral varies with the bond length according to a power law,

$$V_{\alpha\beta\gamma}(L) = V_{0,\alpha\beta\gamma} \left(\frac{L}{L_0}\right)^{\chi_{\alpha\beta\gamma}} \quad (2.5)$$

where α and β refer to the orbital types, γ is the type of bond, L is the bond length, L_0 is the unstrained bond length, $V_{0,\alpha\beta\gamma}$ is the hopping integral for unstrained bond, and $\chi_{\alpha\beta\gamma}$ is the power law exponent. The band structures using this set of hopping

integrals have shown an excellent agreement with GW calculations with various strain ratios[80]. The bulk Si and Ge have mismatched lattice constants with $a_{\text{Si}} = 5.431 \text{ \AA}$ and $a_{\text{Ge}} = 5.658 \text{ \AA}$. Correspondingly, the unstrained bond lengths for Si and Ge are 2.352 \AA and 2.450 \AA , respectively. For simplicity, we study the lattice-matched interface and we assume the Si-Si and Ge-Ge bond lengths are the same, $L = 2.398 \text{ \AA}$, which is relaxed Si-Ge bond length found by Niquet *et al*[80]. Furthermore, we rescale the L_0 for Si-Si bond and Ge-Ge bond to be $L_0 = 2.398 \text{ \AA}$ to ensure that the Si's and Ge's band structures are the same with their unstrained bulk band structures[81, 82]. In our calculation, the spin-orbital coupling is not included.

First, we compare the band structures $E_n(\mathbf{k})$ of bulk Si and Ge along high-symmetry paths and examine the distributions of electron/hole pockets in the first Brillouin zone, as depicted in Fig. 2-2 (a), which clearly shows that the conduction band pockets for Si and Ge are distributed very differently, whereas their valence band pockets are quite similar. In particular, the highest valence bands for Si and Ge are both at Γ point. In contrast, the conduction band edge for Si is close to X point along the Γ X path (in the following, we denote this point Δ), while the conduction band edge for Ge is at L point. In addition, there are 6 pockets for Si's lowest conduction band at Δ point, while there are 4 pockets (or 8 half-pockets) for Ge at L point. The second-lowest conduction band for Si is at X point. The second- and third-lowest conduction bands for Ge are at Γ point and Δ point, respectively.

Next, we look into the symmetry properties of the Bloch wavefunctions in order to develop an understanding of how symmetry affects the transmission. In the bracket notation, the transmission matrix element is directly proportional to the Green's function matrix element,

$$t_{ji} \propto \langle u_j | \hat{G} | u_i \rangle \quad (2.6)$$

where $\hat{G} = (EI - \hat{H})^{-1}$ is the Green's function operator and \hat{H} is the Hamiltonian operator[30, 83]. It is easy to show that \hat{G} inherits all symmetries of \hat{H} [84]. For $|u_j\rangle$ and $|u_i\rangle$ with certain type of symmetries, the transmission matrix element t_{ji} is guaranteed to vanish according to group theory[85]. Thus, it is essential to identify

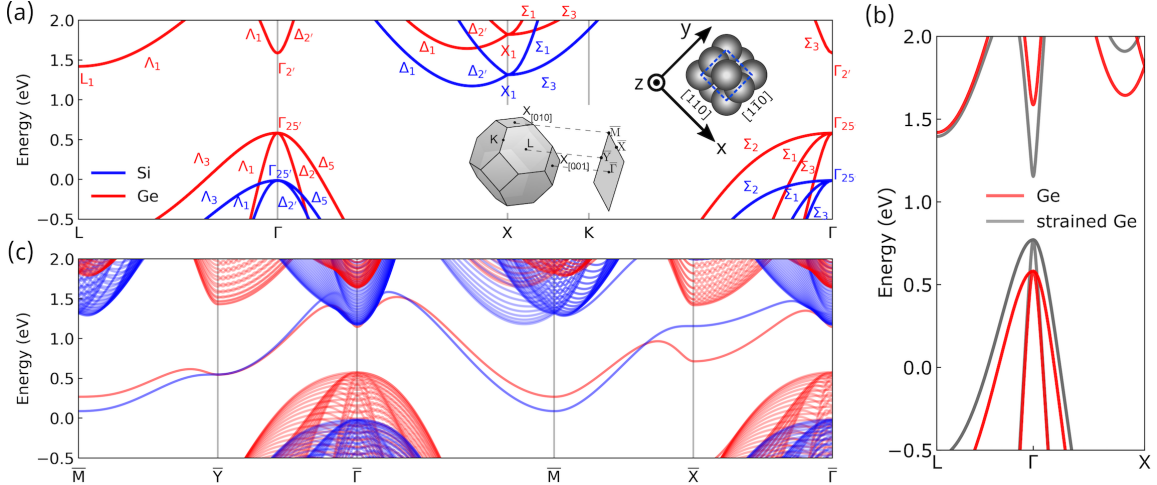


Figure 2-2: (a) The band structure for bulk Si, Ge along high symmetry lines in the first Brillouin zone. Left inset: the three-dimensional first Brillouin zone of Si (Ge) and its projection on the (001) plane. Right inset: the atomic structure for Si (Ge) unitcell along [001] direction. (b) The band structures for Ge and tensile-strained Ge (2 %). (c) The band structures for Si and Ge slabs along high symmetry lines in the surface Brillouin zone. The slab contains 108 atom layers (27 a in thickness with a the lattice constant).

the symmetries of Bloch wavefunctions of the two sides.

To describe the symmetry properties of Bloch wavefunctions in Si and Ge, the Bouckaert-Smoluchowski-Wigner (BSW)[86] notation is adopted in Fig. 2-2 (a), which marks the irreducible representations for the Bloch wavefunction. The different irreducible representations of the same group (labeled by the same Greek letter with different subscripts) are orthogonal to each other. The character tables for different groups can be found in group theory textbooks[85] and online databases[87]. They describe how the Bloch wavefunction transforms under different symmetry operations. For instance, the states of the lowest conduction band of Si at Δ point transform as Δ_1 representation under the symmetry operations of C_{4v} group. On the other hand, the states of the second-lowest conduction band in Ge at Δ point transform as $\Delta_{2'}$ representation. Without the loss of generality, we consider the Δ points along the z axis [(0,0,1) axis]. In this case, one of the C_{4v} group elements is the symmetry operation $\hat{S} = \{C_4|\boldsymbol{\tau}_d\}$ with $\boldsymbol{\tau}_d = \frac{1}{4}(a, a, a)$, which first rotates the Bloch wavefunction by 90 degree with respect to the z axis and then applies the translation operator by $\boldsymbol{\tau}_d$.

When applying \hat{S} to a state $|u_i\rangle$ of Δ_1 symmetry, we have $\hat{S}|u_i\rangle = 1 \cdot e^{ik_z a/4}|u_i\rangle$, where k_z is the wavevector's z component. The phase factor $e^{ik_z a/4}$ appears because the space group of Si (Ge) structure is nonsymmorphic. In comparison, when applying the same operator \hat{S} to a state u_i of $\Delta_{2'}$ symmetry, we have $\hat{S}|u_i\rangle = -1 \cdot e^{ik_z a/4}|u_i\rangle$. Intuitively, one can regard Δ_1 as “even” and $\Delta_{2'}$ as “odd” in a more generalized way. If the incident and transmitted states are not compatible, they will never interact. Hence, knowing the symmetry properties of wavefunctions (*i.e.*, their irreducible representations) will be useful in the later analysis of the transmission probabilities.

Moreover, the strain effect can change the relative positions for different valleys in the reciprocal space. We find that the strain generally has a smaller impact on Si compared with Ge thus we only consider the case of applying strain to Ge. Since we have already assumed the Si and Ge have the same bond lengths $L = 2.398 \text{ \AA}$, we change the equilibrium L_0 of Ge from 2.398 \AA to 2.343 \AA while keeping L unchanged. The corresponding hopping integrals $V_{\alpha\beta\gamma}$ defined in Eq. 2.5 are altered and the Ge band structure is accordingly changed. Equivalently, we have applied a tensile strain of 2 % to Ge. In Fig. 2-2 (b), we compare the band structures of strained Ge (sGe for short) with the relaxed Ge. The elongated bond pushes the second-lowest conduction band downwards and make it the lowest conduction band. It also shifts the third-lowest band further upwards. Meanwhile, the strained Ge-Ge bond also makes the valence band upwards and thus causing a smaller bandgap. The features of the sGe band structure are consistent with other works[51, 88].

When forming an interface, the translational symmetry is broken along the direction normal to the interface, and the band structures are now projected to the two-dimensional surface Brillouin zone, as depicted in the left inset of Fig. 2-2 (c). We conduct a slab calculation to study the projected band structure. The slab is periodic along x and y directions and finite in z direction. The unitcell for Si (Ge) slab along [001] direction contains 4 atoms, as shown in the right inset of Fig. 2-2 (a). Note that the atomic structure of Si (Ge) has mirror symmetries with respect to (110) and $(1\bar{1}0)$ planes. In Fig. 2-2 (c), we find that the highest valence bands of Si and Ge are both projected to the $\bar{\Gamma}$ point. Two out of the six lowest conduction band pockets

of Si are projected to the $\bar{\Gamma}$ point, two pockets are projected to a point between $\bar{\Gamma}$ and \bar{X} point and the remaining two pockets are projected to a point between $\bar{\Gamma}$ and \bar{Y} point. As for Ge, two of the four lowest conduction band pockets at L points are projected to the \bar{X} point and the remaining two are projected to the \bar{Y} point. Since we use a slab to compute the projected band structure, we observe the surface states[89] for Si and Ge in the bandgap. They each have two degenerate surface states within the x-y plane, one for the top surface, one for the bottom surface. However, in the direction normal to the interface (z direction), these surface states are localized thus do not contribute to the interfacial transport.

Lastly, we study the density of states for the projected band. The density of states for the projected band structures at the given energy E and transverse momentum $\mathbf{k}_{uc,\parallel}$ is obtained by taking the imaginary part of retarded surface Green's function given by Eq. A.4 for the lead,

$$SDOS(E, \mathbf{k}_{uc,\parallel}) = -\frac{1}{\pi} \text{Im}g_{\alpha}^r(E, \mathbf{k}_{uc,\parallel}) \quad (2.7)$$

where $g_{\alpha}^r(E, \mathbf{k}_{uc,\parallel})$ is the retarded surface Green's function for α lead with $\alpha = \text{Si}, \text{Ge}$. From the density of states shown Fig. 2-3 (a), where we use color to indicate $\ln[\text{SDOS}(E, \mathbf{k}_{uc,\parallel})]$, we identify the localized states in the bandgap, the continuum spectrum of propagating conduction band electrons and the resonant states inside the continuum spectrum.

2.3.2 Transmission through a perfect interface

We first study the electron transmission through a perfect interface. There are several relevant physical quantities, and we want to clarify their definitions here to avoid confusion. $t_{RL,ji}(E, \mathbf{k}_{sc,\parallel})$ is the transmission matrix, which is used to compute the transmission probability matrix. $T_{ji}(E, \mathbf{k}_{sc,\parallel})$ is the transmission probability matrix, which described mode-to-mode transition probability, normalized by normal incident current. $T_i(E, \mathbf{k}_{sc,\parallel})$ refers the transmission probability (transmittance) across the interface for an incident electron i . The transmission spectrum $T(E, \mathbf{k}_{sc,\parallel})$ is the

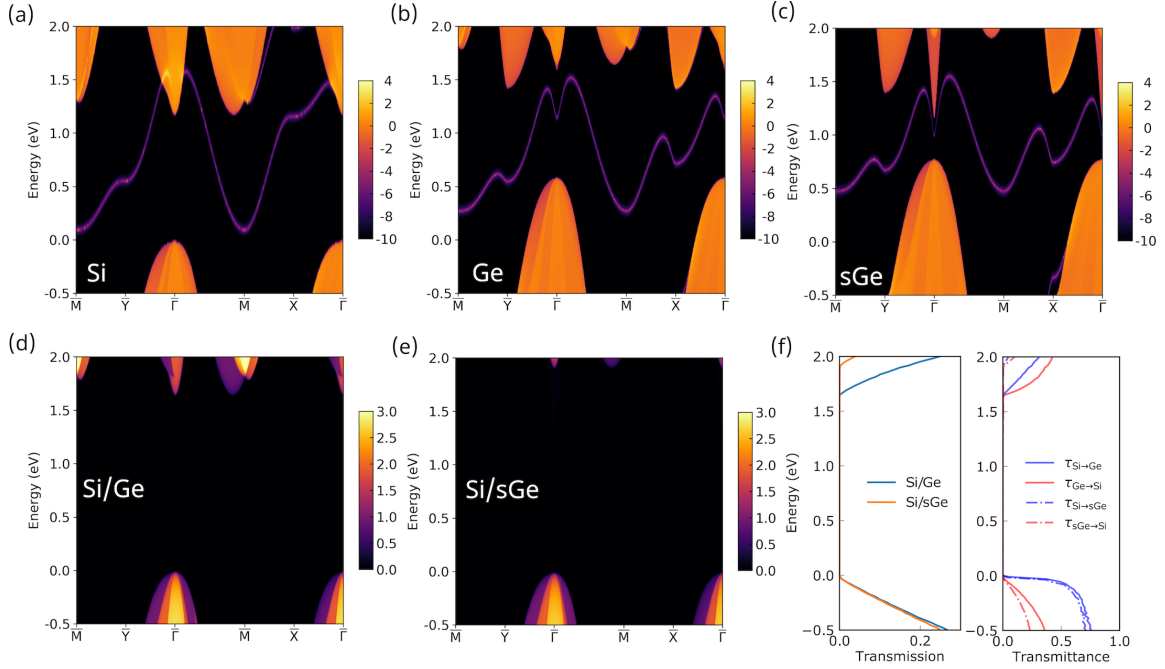


Figure 2-3: The surface density of states $\text{SDOS}(E, \mathbf{k}_{\text{uc},\parallel})$ for (a) Si, (b) Ge and (c) sGe. The logarithm of the surface density of state is indicated by colors and the spin degree of freedom 2 is not multiplied. The transmission spectra $T(E, \mathbf{k}_{\text{uc},\parallel})$ along high symmetry lines in the surface Brillouin zone through (d) a perfect Si/Ge [001] interface and (e) a perfect Si/sGe [001] interface. (f) Left panel: the transmission function $\Theta(E) = \frac{1}{N_{\mathbf{k}_{\text{uc},\parallel}}} \sum_{\mathbf{k}_{\text{uc},\parallel}} T(E, \mathbf{k}_{\text{uc},\parallel})$ for a perfect Si/Ge interface and a perfect Si/sGe interface ($N_{\mathbf{k}_{\text{uc},\parallel}} = 40 \times 40$ is used). Right panel: the transmittance $\tau_\alpha(E) = \frac{\Theta(E)}{\Theta_{\text{bulk},\alpha}(E)}$ from Si and Ge side, where $\Theta_{\text{bulk},\alpha}(E)$ is the transmission function for bulk α material.

number of transmission channels including all subbands that have same E and $\mathbf{k}_{\text{sc},\parallel}$. The transmission function (we use transmission in short in figures) $\Theta(E)$ describe the total number of transmission channels at the given energy E and is the sum of all transmission channels with different $\mathbf{k}_{\text{sc},\parallel}$. Note that $t_{RL,ji}(E, \mathbf{k}_{\text{sc},\parallel})$, $T_{ji}(E, \mathbf{k}_{\text{sc},\parallel})$, $T_i(E, \mathbf{k}_{\text{sc},\parallel})$ depend on which side incident electron is from, whereas $T(E, \mathbf{k}_{\text{sc},\parallel})$, $\Theta(E)$ are independent of the side of incidence.

The transmission probability can be computed by summing the transmission probability matrix over all possible final states. And the specular part and nonspecular

part of the transmission probability read,

$$\begin{cases} T_{s,i}(E, \mathbf{k}_{sc,\parallel}) = \sum_j T_{s,ji}(E, \mathbf{k}_{sc,\parallel}) \\ T_{ns,i}(E, \mathbf{k}_{sc,\parallel}) = \sum_j T_{ns,ji}(E, \mathbf{k}_{sc,\parallel}) \end{cases} \quad (2.8)$$

The transmission function is the measure of conductance channels and it can be expressed by, $\Theta(E) = \Theta_s(E) + \Theta_{ns}(E)$, where the specular and nonspecular transmission function are defined by,

$$\begin{aligned} \Theta_s(E) &= \frac{1}{N_{\mathbf{k}_{sc,\parallel}}} \sum_{i,\mathbf{k}_{sc,\parallel}} T_{s,i}(E, \mathbf{k}_{sc,\parallel}) \\ \Theta_{ns}(E) &= \frac{1}{N_{\mathbf{k}_{sc,\parallel}}} \sum_{i,\mathbf{k}_{sc,\parallel}} T_{ns,i}(E, \mathbf{k}_{sc,\parallel}) \end{aligned} \quad (2.9)$$

For the case of perfect interface, all the transmission processes are specular, hence we have $T_{s,ji}(E, \mathbf{k}_{sc,\parallel}) = T_{ji}(E, \mathbf{k}_{sc,\parallel})$. In addition, for the perfect interface, we only need to construct a unitcell as the supercell such that the in-plane momenta in the unitcell representation and the supercell representation are the same, $\mathbf{k}_{uc,\parallel} = \mathbf{k}_{sc,\parallel}$.

The transmission spectrum is attained by $T(E, \mathbf{k}_{uc,\parallel}) = \sum_i T_i(E, \mathbf{k}_{uc,\parallel})$, where we sum over all subbands with the same E and $\mathbf{k}_{uc,\parallel}$. In Fig. 2-3 (d) and (e), we show the transmission spectra $T(E, \mathbf{k}_{uc,\parallel})$ through the Si/Ge and Si/sGe interfaces. Comparing with the surface density of states through examining the Fig. 2-3 (a)-(d), we see that the transmission is non-zero only when the surface density of states for Si and sGe overlap. This is due to the energy and momentum conservation requirement. For example, the Ge's lowest conduction band at \bar{X} and \bar{Y} does not have any corresponding states in Si thus cannot contribute to transmission. Most of the overlapped states are the valleys at $\bar{\Gamma}$ and along the $\bar{\Gamma}\bar{M}$ path, which corresponds to the lowest conduction band in Si, and second- and third-lowest conduction bands in Ge.

Because of the mismatch of conduction band valleys of Si and Ge, a large “transport gap” of 1.65 eV emerges at the $\bar{\Gamma}$ point. For a Si/sGe interface, the transmission spectra for holes change slightly from a Si/Ge interface. The transport gap is 1.91 eV, which even larger due to fewer energy and momentum matched conduction bands.

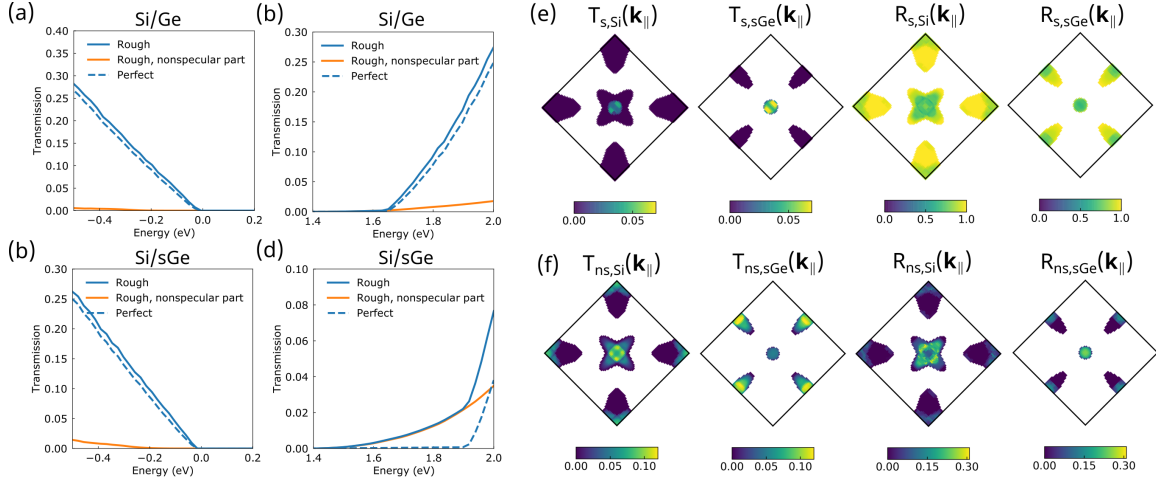


Figure 2-4: The ensemble-averaged total transmission function $\Theta(E)$ and nonspecular transmission function $\Theta_{ns}(E)$ through rough Si/Ge interfaces for (a) electrons and (b) holes in solid lines compared with the transmission function for a perfect interface in dashed line. 21 configurations of 2×2 , 8 ml disordered interfaces are used for ensemble average. (c) and (d): the transmission function for Si/sGe interfaces. (e) and (f): the ensemble-averaged mode-resolved specular and nonspecular scattering probabilities at $E = 1.77$ eV for rough Si/sGe interfaces defined by Eq. 2.8 as a function of in-plane momentum $\mathbf{k}_{uc,\parallel}$. The calculation uses a $40 \times 40 \mathbf{k}_{sc,\parallel}$ -point mesh. Equivalently, it corresponds to a $80 \times 80 \mathbf{k}_{uc,\parallel}$ mesh.

From the energy-resolved transmission and transmittance in Fig. 2-3 (f), we also find that strain has much smaller impact on the hole transmission than the electron transmission. This is because the valence bands stay at $\bar{\Gamma}$ point even with strain, while the strain changes the position of conduction bands in reciprocal space more profoundly.

What is intriguing is that at $\bar{\Gamma}$ point, Si and sGe have overlapped conduction band pockets, yet the transmission $T(E, \mathbf{k}_{uc,\parallel})$ is still almost zero. This implies that there are other factors other than energy and momentum conservation which limits the transmission. We found out that the zero transmission originates from the different symmetries of the wavefunctions. In three-dimensional Brillouin zone, the lowest conduction band of sGe is at Γ point with Γ_2' symmetry. Under the symmetry operation $\hat{S} = \{C_4 | \tau_d\}$ mentioned above, it transforms as $\hat{S}|u_{R,\Gamma}\rangle = -|u_{R,\Gamma}\rangle$. In comparison, for the lowest conduction band of Si at Δ point, it satisfies $\hat{S}|u_{L,\Delta}\rangle = e^{ik_{L,z}a/4}|u_{L,\Delta}\rangle$. The Hamiltonian for a perfect Si/sGe interface should always have “even” symmetry representation Δ_1 . Hence, it follows that $\hat{S}\hat{H} = e^{ik_{L,z}a/4}\hat{H}$ and

$\hat{S}\hat{G} = e^{-ik_{L,z}a/4}\hat{G}$. As a result, the transmission matrix element should satisfy the condition, $t_{ji} \propto \langle u_{R,\Gamma} | \hat{G} | u_{L,\Delta} \rangle = \langle \hat{S}u_{R,\Gamma} | \hat{S}\hat{G} | \hat{S}u_{L,\Delta} \rangle = -\langle u_{R,\Gamma} | \hat{G} | u_{L,\Delta} \rangle$. Consequently, we obtain that $T_{ji} = |t_{ji}|^2 = 0$. Similarly, for the electrons at Δ point with $\mathbf{k} = (0, 0, k_{R,z})$, they have Δ_2' symmetry and transform as $\hat{S}|u_{R,\Delta}\rangle = -e^{ik_{R,z}a/4}|u_{R,\Delta}\rangle$. Resultantly, we have $t_{ji} \propto \langle u_{R,\Delta} | \hat{G} | u_{L,\Delta} \rangle = \langle \hat{S}u_{R,\Delta} | \hat{S}\hat{G} | \hat{S}u_{L,\Delta} \rangle = -\langle u_{R,\Delta} | \hat{G} | u_{L,\Delta} \rangle$ and correspondingly $T_{ji} = 0$. In short, the transmission at $\bar{\Gamma}$ is exactly zero, dictated by symmetry.

2.3.3 Transmission through rough interfaces

We add interface disorders in the form of atomic mixing. In particular, we randomly swap pairs of Si and Ge atoms that have the same distance to the interface. We use a larger supercell with in-plane periodicity to describe the rough interface. To mimic an actual rough Si/Ge interface observed in experiments[58], we make sure that the further away from the interface, the fewer or equal number of atom pairs are swapped. In the following, we define two measures of the degree of interface disorders along the interface normal and along the transverse directions.

The first measure is the number of atom layers that are involved in atomic mixing. If there are 2 layers of Si and 2 layers of Ge atoms that are involved in atomic intermixing, the number of atoms that are swapped per layer follows a pattern of 1|2|2|1. We label such interface structure by 4 ml, in short for four mixing layers. A larger ml number corresponds to the larger degree of disorders in the cross-plane direction. The atomic number density of Si across the rough interface with different mixing layers can be found in Fig. A-1 in the Appendix A.

The second measure is the size of the transverse supercell. For example, when we construct a 2×2 transverse supercell with 4 ml structure, there are 2 out of 4 atoms for the Si atom layer closest to the interface and 1 out of 4 atoms for the Si atom layer secondly closest to the interface involved in atomic mixing. When we use a larger transverse supercell (3×3 or 4×4), we let the number of swapped atoms unchanged. The larger transverse supercell we use, the smaller degree of disorders along the transverse directions. For a given ml number and a given supercell size, we generate 21 random configurations and compute the ensemble average of the transmission and

reflection probability matrix elements.

We found that the total transmissions for electrons and holes are both enhanced for rough Si/Ge and Si/sGe interfaces compared with the corresponding perfect interfaces, as shown in Fig. 2-4 (a)-(d). Particularly, the total transmission function for a perfect Si/sGe interface with energy E ranging from 1.5 eV to 1.9 eV is zero, whereas transmission function for the corresponding rough interface is largely enhanced by nonspecular scattering processes. For the hole transmission, we notice that the nonspecular part is much smaller than the specular part and the enhancement in the total transmission is not significant, although the transmission for both electrons and holes are enhanced by the rough interface compared with the perfect interface. This is because holes are close to $\mathbf{k} = 0$ and have long wavelengths. In Fig. A-2 of Appendix A, we have shown the dependence of transmission function on the degree of disorders along transverse and longitudinal directions. It turns out that the smaller transverse supercell dimensions and large mixing layer numbers are in favor of the nonspecular transmission. The smaller transverse supercell provides a large \mathbf{G}_{\parallel} , which allows the transition between valleys with large momentum mismatch. The larger degree of disorders along the perpendicular direction can lower the lateral symmetry to a greater extent and provides more channels that are previously forbidden by symmetry. Moreover, the effective thickness δ of the interface roughness along the perpendicular direction increases with increasing ml number. The interface roughness preferably couples with carriers with $|k_z| \sim \frac{2\pi}{\delta}$. The enhancement of transmission will be promoted if the corresponding valley satisfies $|k_z| \sim \frac{2\pi}{\delta}$.

In Fig. 2-4 (e), we plot the mode-resolved specular transmission and reflection probabilities at $E = 1.77$ eV as a function of their unfolded momentum $\mathbf{k}_{uc,\parallel}$. We find that the overlapped valleys for Si and sGe at $\bar{\Gamma}$ point lead to small specular transmission probability. This is because the atomic mixing at the interface breaks the symmetry of Hamiltonian \hat{H} and the above-mentioned symmetry-forbidden transmission at $\bar{\Gamma}$ point is now allowed. In Fig. 2-4 (f), we show the nonspecular transmission and reflection probabilities. The majority of nonspecular transmission processes are found to be starting from the $\bar{\Gamma}$ and \bar{M} point in Si to the \bar{X} and \bar{Y} point in sGe.

These processes correspond to the transition between the lowest conduction band of Si at Δ point and the lowest conduction band of Ge at L in the three-dimensional Brillouin zone. Si's conduction band at Δ point and Ge's conduction band at L point are both far from Γ point and the conduction electrons have small wavelengths. The characteristic length of disorders has to be small to contribute to the nonspecular interface scattering. Thus, smaller transverse supercell dimensions, *i.e.*, atomic-scale disordered structures, are in favor of more nonspecular transmission channels.

We can define the specular and nonspecular reflection probabilities similarly to the transmission. By examining the specular and nonspecular reflection probabilities, we find that the newly emerged nonspecular reflection channels are accompanied by the removal of the specular transmission channels at the same $\mathbf{k}_{uc,\parallel}$. Although the increasing nonspecular reflection probability is detrimental for interfacial transport, there are overall more nonspecular transmission channels than the nonspecular reflection channels thus total transmission is still enhanced.

With the knowledge of the transmission function, we proceed to compute the contact resistance. The Landauer-Büttiker formalism is used to compute the two-probe conductance,

$$G_{12} = -\frac{2e^2}{h} \int dE \Theta(E) \frac{\partial f}{\partial E} \quad (2.10)$$

where h is the Plank constant, $f = \frac{1}{e^{(E-\mu)/k_B T} + 1}$ is the Fermi-Dirac distribution function and the factor 2 describes the spin degree of freedom. The subscripts 1 and 2 refer to the left and right sides. The four-probe conductance can be computed by[29, 30],

$$G_4 = \frac{1}{G_{12}^{-1} - \frac{1}{2}(G_{11}^{-1} + G_{22}^{-1})} \quad (2.11)$$

where G_{11} and G_{22} are the two-probe conductance for bulk material 1 and 2, respectively. In practical calculations of the conductance for a bulk material, we let the two leads and devices all consist of same materials. Then, the specific contact resistance is defined by,

$$\rho_c = \frac{A}{G_4} \quad (2.12)$$

where A is the cross-section area.

In Fig. 2-5, we observe over an order of magnitude reduction in the contact resistance for conduction electrons through the rough Si/sGe interface at various temperatures compared with the corresponding perfect interface. For the rough Si/Ge interface, a much smaller reduction in contact resistance for conduction electrons is found. This is because the perfect Si/Ge interface does not have the symmetry-forbidden transmission for low-energy conduction electrons as the perfect Si/sGe interface does. As a result, for Si/Ge interface, the lowered symmetry due to interface roughness does not benefit as much as the Si/sGe interface. For valence bands, the hole contact resistances for Si/Ge and Si/sGe interfaces are only slightly reduced by the interface disorders, as most holes from two sides have compatible momenta and symmetries.

Last but not least, we want to examine how the symmetry of the disordered interface changes the nonspecular transmission. The nonspecular transmission probability can be analyzed using perturbation theory[90, 76] and we argue that the non-specular transmission probability is proportional to the scattering matrix element, $t_{ns,ji} \propto \langle u_j | \Delta H | u_i \rangle$, where the perturbed potential is the difference between the potential energy for disordered interface and perfect interface, $\Delta H = H_{\text{rough}} - H_{\text{perfect}}$. For different disordered interface structures, the symmetry of ΔH can be different.

In Fig. 2-6, we have shown the nonspecular transmission for three representative disordered interface configurations. In Fig. 2-6 (d), we have plotted the projected band structures of Si and sGe, sorted according to the symmetries of Bloch wavefunctions under mirror operation. The conduction band for Si and sGe are both even under the σ_x operation, thus it is preferred to have ΔH with even symmetry as well such that $t_{ns,ji} \propto \langle u_j | \Delta H | u_i \rangle = \langle \sigma_x u_j | \sigma_x \Delta H | \sigma_x u_i \rangle = \langle u_j | \Delta H | u_i \rangle$ and $t_{ns,ji}$ is not forbidden by symmetry. As for the case with no mirror symmetries along x or y directions, the symmetry of the whole system is lowered and the symmetry analysis for $t_{ns,ji}$ does not work. Although there are some nonspecular transmission channels for the case with no mirror symmetry, the nonspecular transmission still favors the disordered structures with compatible symmetries with the initial and final states than those without.

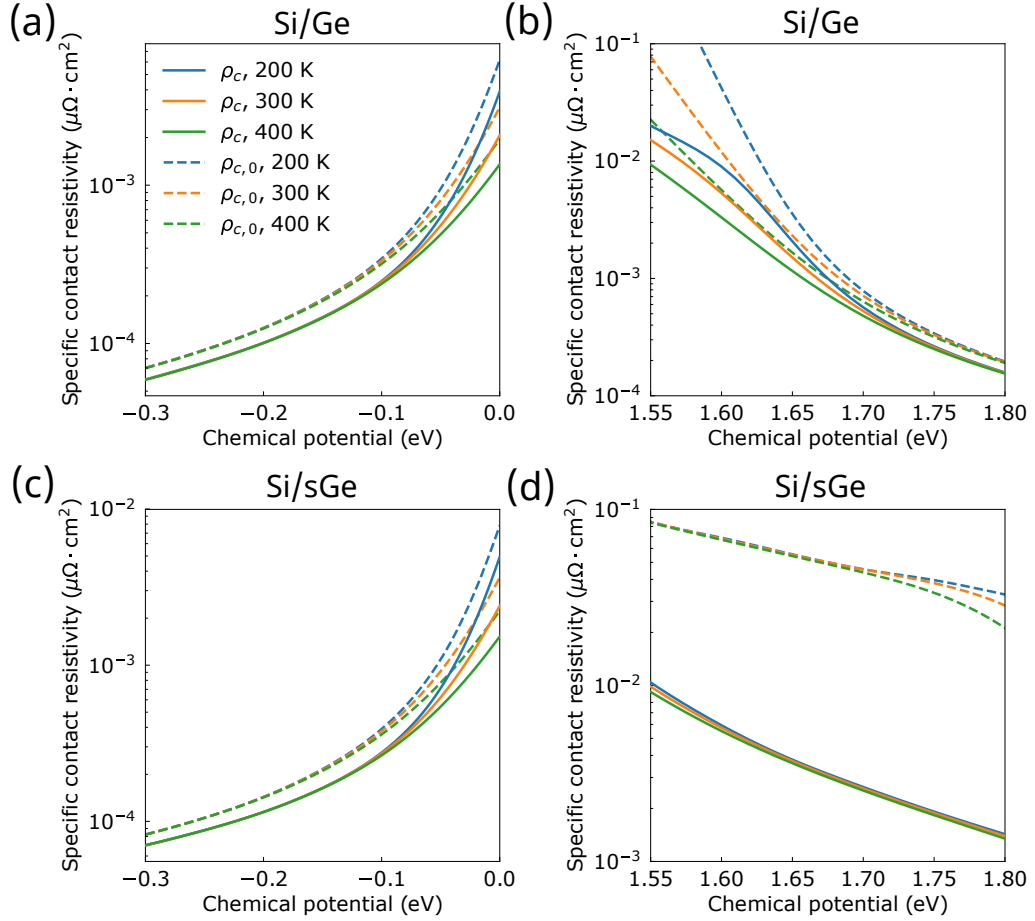


Figure 2-5: The specific contact resistance for (a) electrons and (b) holes for rough Si/Ge interfaces in solid lines and for the perfect Si/Ge interface in dashed lines at various temperatures. The specific contact resistance for (c) electrons and (d) holes for rough Si/sGe interfaces in solid lines and the perfect Si/sGe interface in dashed lines at various temperatures.

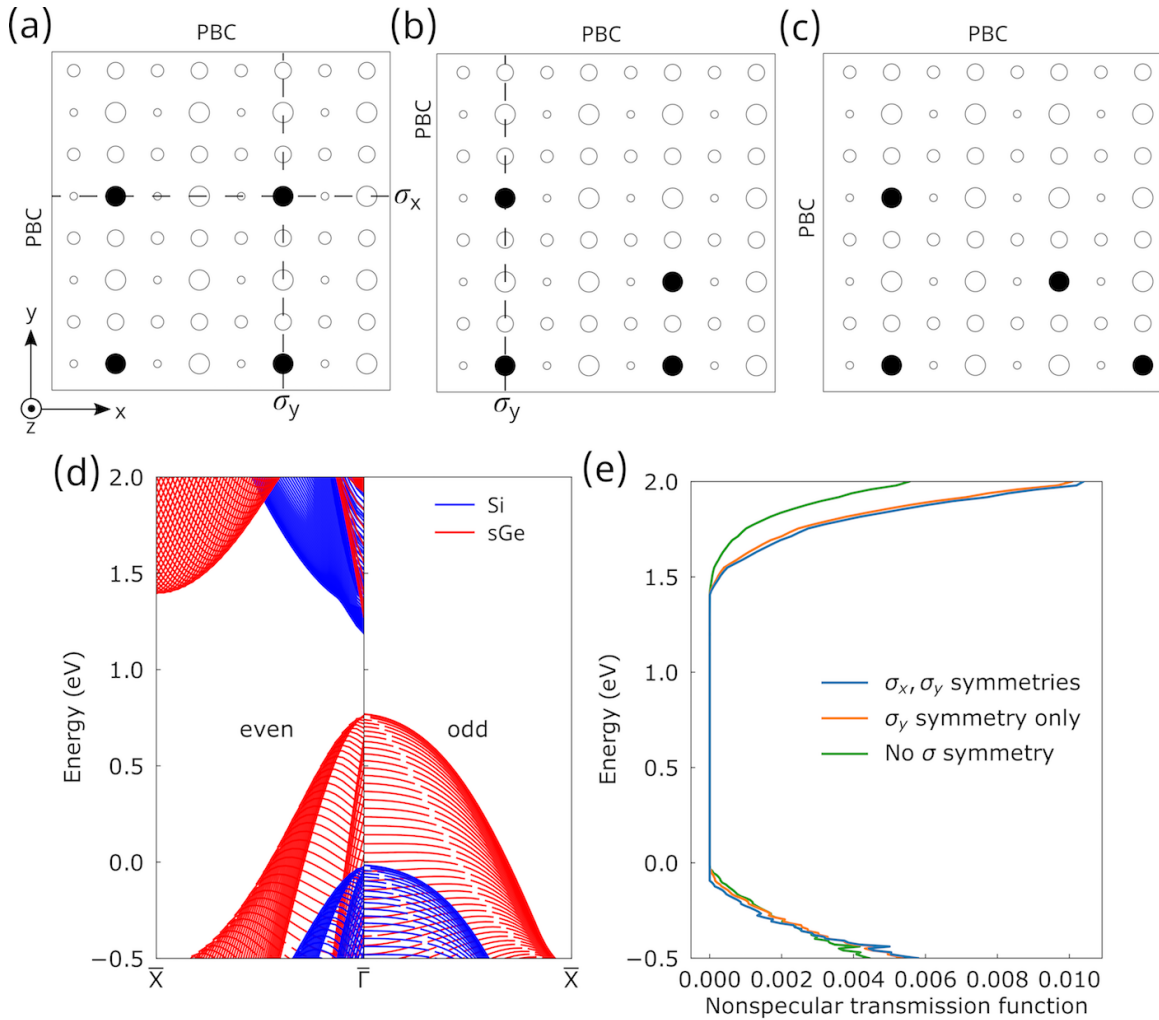


Figure 2-6: (a) The disordered structure with both σ_x and σ_y symmetry. (b) The disordered structure without σ_x yet with σ_y symmetry. (c) The disordered structure without σ_x and σ_y symmetry. σ_x and σ_y refer to the mirror symmetries along the x and y directions. In (a)-(c), the open circles are the Si atoms and the filled circles refer to the swapped Ge atoms. The larger circles represent the atoms closer to the interface. We only plot the Si side here, and on the Ge side the swapped Si atoms have the same transverse positions with the swapped Ge atoms on the Si side. (a)-(c) all correspond to 4×4 , 2 ml structures. (d) The projected bulk band structures of Si and sGe along $\bar{\Gamma}\bar{X}$ in the surface Brillouin zone sorted by their symmetries. (e) The nonspecular transmission function $\Theta_{ns}(E)$ for the three disordered interface structures plotted in (a)-(c).

2.4 Conclusion

We have studied the charge transport through a [001] Si/Ge interface. The transmission through a perfect interface must be specular. The electron transmission through the Si/Ge interface is very low due to momentum-mismatched band structures. The incompatible symmetries of the electron states at different pockets also forbid the transmission, leading to a high contact resistance. However, with atomic mixing at the interface, the symmetry is lowered and the previously forbidden transmission is allowed. In addition, the nonspecular transmission connecting electron pockets with different transverse momentum is enabled by those interface disorders. As a result, the specific contact resistance is reduced by over an order of magnitude.

Chapter 3

Phonon transport through rough interfaces

3.1 Introduction

The interface between two dissimilar materials, or even same materials but different crystal orientations, can scatter phonons and gives rise to the thermal boundary resistance for heat flow across the interface[8, 91, 92]. One model for the thermal boundary resistance is based on assuming that phonons are specularly scattered at the interface and computing the phonon transmittance and reflectance based on acoustic wave equations, *i.e.*, the acoustic mismatch model (AMM)[93, 91]. However, it was found that the AMM only works at very low temperatures at which the phonon wavelengths are long. At elevated temperatures, phonons of short wavelengths carry most of the heat, and they do not experience specular transmission/reflection due to interface imperfections, such as atomic mixing. The diffuse mismatch model (DMM) is proposed as an extreme to describe phonon transport across such rough interfaces[8]. Two major assumptions are made in the DMM. Firstly, the transmittance is isotropic, *i.e.*, transmittance is angle-independent. Secondly, phonons lose memory of their origin after being scattered by the interface such that one cannot distinguish if a phonon has just been through a transmission or reflection process. Although the DMM has improved the agreement with experimental measurements of thermal boundary resis-

tance at high temperatures[94, 95], the assumptions behind DMM have never been examined in detail.

The thermal boundary resistance has been studied using equilibrium molecular dynamics[96, 97, 98] and nonequilibrium molecular dynamics[99, 100, 101]. In particular, phonon-mode-resolved transmittance had been formulated, which builds upon the atomic trajectories at steady state from molecular dynamics (MD) simulations[102], where the anharmonicity of phonons is intrinsically included. It has been applied to study mode-resolved transmittance through perfect interfaces, yet it has not been used to examine details of diffuse phonon transmittance across a disordered interface. Phonon wave-packet dynamics technique has been applied to compute the transmittance and reflectance of each phonon mode, and the Kapiza resistance can be calculated using Landauer formalism[103, 104]. The MD simulations and, especially the wave-packet dynamics simulations, however, require large structures in real space, including two bulk regions and the interface region, and simulating phonon transport through a rough interface with a large lateral dimension becomes computationally extensive.

The atomistic Green's function (AGF) has been shown as an effective method to study phonon interfacial transport[105, 37, 106]. The method is formulated in reciprocal space such that one does not have to deal with large-scale simulations of atomic displacements in real space. Recent advances in calculation of interfacial thermal resistance using the AGF have provided more insights in understanding interfacial thermal resistance with detailed information including mode-resolved transmission coefficients[107, 108, 109, 105]. Specifically, Ong *et al* studied the phonon specular-ity and coherence for phonon transport through a disordered grain boundary in two-dimensional graphene, and showed that incoherent phonon scatterings at interface are almost perfectly diffusive[110]. Ong also demonstrated that the specularity parameters are different for transmittance and reflectance for graphene grain-boundaries[111]. Using AGF combined with *ab initio* inter-atomic force constants, Tian *et al* found that the intermixing of atoms for Si/Ge interface can enhance interfacial thermal conductance[106]. Sadashivam *et al* demonstrated using phonon-eigenspectrum-based

formulation of AGF that the enhanced interfacial thermal conductance of a Si/Ge interface with atom intermixing comes from diffuse transmission channels where the in-plane momentum is not conserved[108]. The scattering boundary method (SBM), a mathematically equivalent method to AGF has been proposed by Young *et al*[112] and generalized by Zhao *et al*[113] to study mode-resolved phonon scattering at the interface. Simon *et al*[114] has applied SBM to study phonon scattering at the interface between two-dimensional materials. Recently, Latour *et al* have demonstrated the transmission spectra across a perfect interface as a function of incident angle of phonons, using mode-resolved AGF[109]. However, in order to study diffuse phonon scattering, a supercell of a rough interface with a large lateral dimension is required. In addition, the folded lateral wavevector in the supercell must be carefully mapped back to the wavevector defined in the original unitcell. We realize that, despite these studies, none of them had critically examined the validity of DMM for diffuse phonon scattering.

In this Chapter, we conduct mode-resolved AGF calculation of transmittance and reflectance, and revisit the assumptions of DMM. Our study reveals that most phonons do not lose their memory of origin. We also derive an analytical expression for the diffuse transmittance and reflectance based on a continuum model, and show that it works reasonably well at low frequencies.

3.2 Methodology

3.2.1 Revisiting DMM

To derive the DMM, Swartz and Pohl[8] have made two major assumptions. The first assumption is that phonons are diffusely scattered by the interface and the transmittance is isotropic,

$$T_{L \rightarrow R}(\omega, \mathbf{q}\nu) = T_{L \rightarrow R}(\omega) \quad (3.1)$$

where \mathbf{q} is the wavevector of the phonon with frequency ω and ν is the phonon branch index on the left side. The second assumption is that the transmittance from one

side must equal the reflectance from the other side, *i.e.*, complete loss of memory,

$$R_{R \rightarrow R}(\omega, \mathbf{q}\nu) = T_{L \rightarrow R}(\omega) \quad (3.2)$$

Consequently, the transmittance from right side writes,

$$T_{R \rightarrow L}(\omega, \mathbf{q}\nu) = 1 - T_{L \rightarrow R}(\omega) \quad (3.3)$$

At a given frequency, by invoking the principle of detailed balance, the transmittance in the elastic scattering limit writes,

$$\begin{aligned} & T_{L \rightarrow R}(\omega) \\ &= \frac{\sum_{\mathbf{q}\nu}^+ \frac{v_{Rz,\mathbf{q}\nu}}{V_{uc,R}} \delta(\omega - \omega_{R,\mathbf{q}\nu})}{\sum_{\mathbf{q}\nu}^+ \frac{v_{Lz,\mathbf{q}\nu}}{V_{uc,L}} \delta(\omega - \omega_{L,\mathbf{q}\nu}) + \sum_{\mathbf{q}\nu}^+ \frac{v_{Rz,\mathbf{q}\nu}}{V_{uc,R}} \delta(\omega - \omega_{R,\mathbf{q}\nu})} \\ &= \frac{\Theta_{bulk,R}(\omega)}{\Theta_{bulk,L}(\omega) + \Theta_{bulk,R}(\omega)} \end{aligned} \quad (3.4)$$

where $v_{\alpha z, \mathbf{q}\nu}$ with $\alpha = L, R$ is the group velocity normal to the interface for phonons from the left or the right side, $\omega_{\alpha, \mathbf{q}\nu}$ is the phonon frequency and $V_{uc,\alpha}$ is the volume of unitcell of the left and the right side. The superscript + means that only forward-moving states with $v_{\alpha z, \mathbf{q}\nu} > 0$ are included in the summation. The transmittance can also be written in terms of the ratio of transmission functions, as expressed in the second line of the equation. $\Theta_{bulk,L/R}(\omega)$ is the bulk transmission function for the left/right side, which is a measure of the number of heat conduction channels.

To assess the validity of DMM, we examine if the transmittance and reflectance are indeed isotropic and if the transmittance from one side and reflectance from the other side are the same.

3.2.2 Mode-resolved atomistic Green's function formalism

The essential physical quantities to study diffuse phonon scattering by a rough interface are the transmission probability matrix $T_{mn}(\omega)$ and reflection probability matrix $R_{ln}(\omega)$ at a given phonon frequency ω , which describe the transition probability from

the initial state n to the final state l or m via interface scattering processes. These matrices are computed from mode-resolved atomistic Green's function formalism as outlined in Ref. [75, 107, 110], with details provided in the supplementary material in Ref. [76]. Specifically, we divide the system of interest into three parts, the left lead, the right lead and the device. We have applied decimation technique in computing the surface Green's function for the leads[115]. The recursive Green's function method is used to compute the Green's function for the device region[116, 117]. A propagating state coming out of one lead can be transmitted through (or be reflected by) the device region and travel to the other lead (or the same lead). We then compute the ratio of the heat flux along the z direction of the outgoing state m (or state l), to the heat flux along the z direction of the initial state n , which is the element of transmission probability matrix $T_{mn}(\omega)$ (or reflection probability matrix $R_{ln}(\omega)$).

For a rough interface created by atomic mixing at the interface, the transverse translational symmetry is broken by the interfacial disorders. It is impractical to compute scatterings of an infinitely large rough interface. Instead, we construct a supercell of two materials and a rough interface between them with periodic boundary conditions along the transverse directions (x -direction and y -direction). Because of the transverse periodicity of the supercell, the phonon state of the lead region defined at a given transverse wavevector $\mathbf{q}_{sc,\parallel}$ can only be scattered into phonon states of the lead region (either the left or the right lead) with the same wavevector $\mathbf{q}_{sc,\parallel}$.

The lead part of the supercell contains $N_x \times N_y$ repeated unitcells, as depicted in Fig. 3-1 (a). The period lengths of the lead along the direction normal to the interface are $a_{z,L}$ for the left lead and $a_{z,R}$ for the right lead. The phonon wavevectors parallel to the interface in the supercell and in the unitcell representations are related via $\mathbf{q}_{uc,\parallel} = \mathbf{q}_{sc,\parallel} + a\mathbf{G}_{sc,x} + b\mathbf{G}_{sc,y}$, where a and b are integers. $\mathbf{G}_{sc,x}$ and $\mathbf{G}_{sc,y}$ are transverse reciprocal lattice vectors of the supercell. The phonon states at the corresponding equivalent wavevectors (with same q_z and same branch index) in the two representations are equivalent[118]. The phonon state in the unitcell representation is preferred as it is much easier to interpret than the supercell representation (we will hide subscript uc in the following for visual clarity). However, for a given

supercell state $\mathbf{q}_{sc,\parallel}$, there are multiple possible choices of a and b . To find out the correct pair of a and b for wavevector \mathbf{q}_\parallel is known as an unfolding problem. We have adopted the unfolding scheme by Popescu *et al*[74] and the details can be found in the supplementary material in Ref. [76].

For an interface scattering event, the transverse wavevectors for initial state n and final state m in the unitcell representation are constrained by,

$$\mathbf{q}_n = \mathbf{q}_m + a\mathbf{G}_{sc,x} + b\mathbf{G}_{sc,y}, \quad (3.5)$$

where a and b are unknown integers, as wavevectors of initial and final states in the supercell representation can be unfolded differently. This expression indicates that the interface scattering can either be a momentum conserved (specular), when $a = b = 0$, or momentum non-conserved (diffuse) process for other a and b values. Depending on the transverse wavevector of state n and state m , the transmission probability matrix can be categorized into specular and diffuse transmission parts $T_{mn}(\omega) = T_{s,mn}(\omega) + T_{d,mn}(\omega)$, where

$$\begin{cases} T_{s,mn}(\omega) = T_{mn}(\omega), & \text{when } \mathbf{q}_{\parallel,n} = \mathbf{q}_{\parallel,m} \\ T_{d,mn}(\omega) = T_{mn}(\omega), & \text{when } \mathbf{q}_{\parallel,n} \neq \mathbf{q}_{\parallel,m} \end{cases} \quad (3.6)$$

The reflection probability matrix can be analogously expressed by, $R_{ln}(\omega) = R_{s,ln}(\omega) + R_{d,ln}(\omega)$, where

$$\begin{cases} R_{s,ln}(\omega) = R_{ln}(\omega), & \text{when } \mathbf{q}_{\parallel,n} = \mathbf{q}_{\parallel,l} \\ R_{d,ln}(\omega) = R_{ln}(\omega), & \text{when } \mathbf{q}_{\parallel,n} \neq \mathbf{q}_{\parallel,l} \end{cases} \quad (3.7)$$

The diffuse transmittance for a given incident phonon n from the left side is defined by summing over the scattering probabilities of all possible outgoing states,

$$T_{d,L \rightarrow R}(\omega, \Omega_L) = \sum_m T_{d,mn}^{L \rightarrow R}(\omega) \quad (3.8)$$

where $\Omega_L = (\theta, \phi)$ indicates transmittance is a directional quantity. The polar and

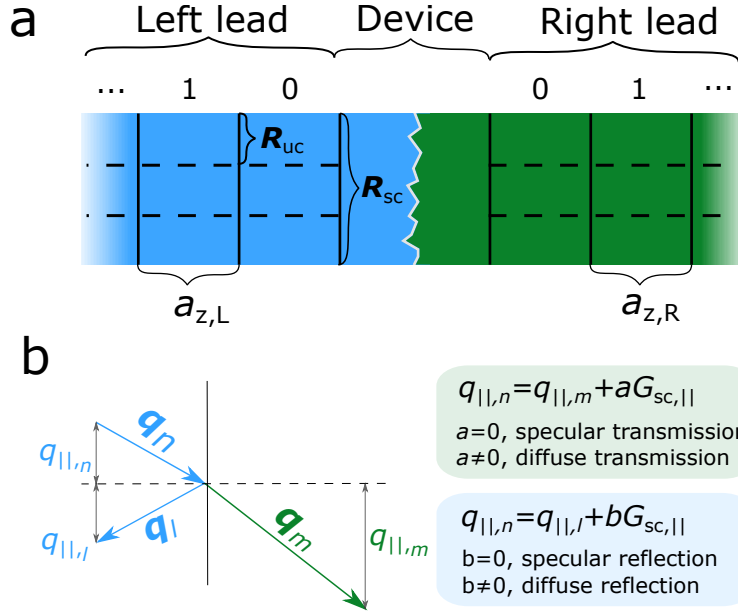


Figure 3-1: (a) In AGF, the system is partitioned into three parts: two semi-infinite leads and a rough interface as the device region. The lead region in the supercell, contains N_{uc} unitcells and transverse lattice vector $\mathbf{R}_{sc} = N_{uc}\mathbf{R}_{uc}$. The numbers $0, 1, \dots$ denote the index of repeated cells for left and right leads. The period lengths along the direction normal to the interface are $a_{z,L}$ and $a_{z,R}$ for the left and right lead, respectively. (b) The in-plane wavevector for incident, transmitted and reflected phonons, $\mathbf{q}_{||,n}$, $\mathbf{q}_{||,m}$ and $\mathbf{q}_{||,l}$. $a = 0$ corresponds to specular transmission, while $a \neq 0$ corresponds to diffuse transmission. Similarly, $b = 0$ corresponds to specular reflection, while $b \neq 0$ corresponds to diffuse reflection. Note the schematic is drawn for two-dimensional system for visual clarity and for three-dimensional system the partitioning and wavevector conservation laws can be analogously defined.

azimuthal angles are defined in a coordinate system where the interface normal lies along the z-axis, $\theta = \arccos \frac{v_z}{|\mathbf{v}|}$, $\phi = \arctan \frac{v_y}{v_x}$. $\mathbf{v} = (v_x, v_y, v_z)$ is the group velocity for incident phonon n from the left side and we use $L \rightarrow R$ to denote the trajectory of the phonon. The reason for using the angle of the group velocity rather than the phase velocity (or wavevector) is that group velocity is a uniquely defined quantity irrelevant to the choice of in-plane Brillouin zone while not for the phase velocity. Likewise, the diffuse reflectance for a given initial state n from the left side and from the right side read,

$$R_{d,\alpha \rightarrow \alpha}(\omega, \Omega_\alpha) = \sum_m R_{d,mn}^{\alpha \rightarrow \alpha}(\omega) \quad (3.9)$$

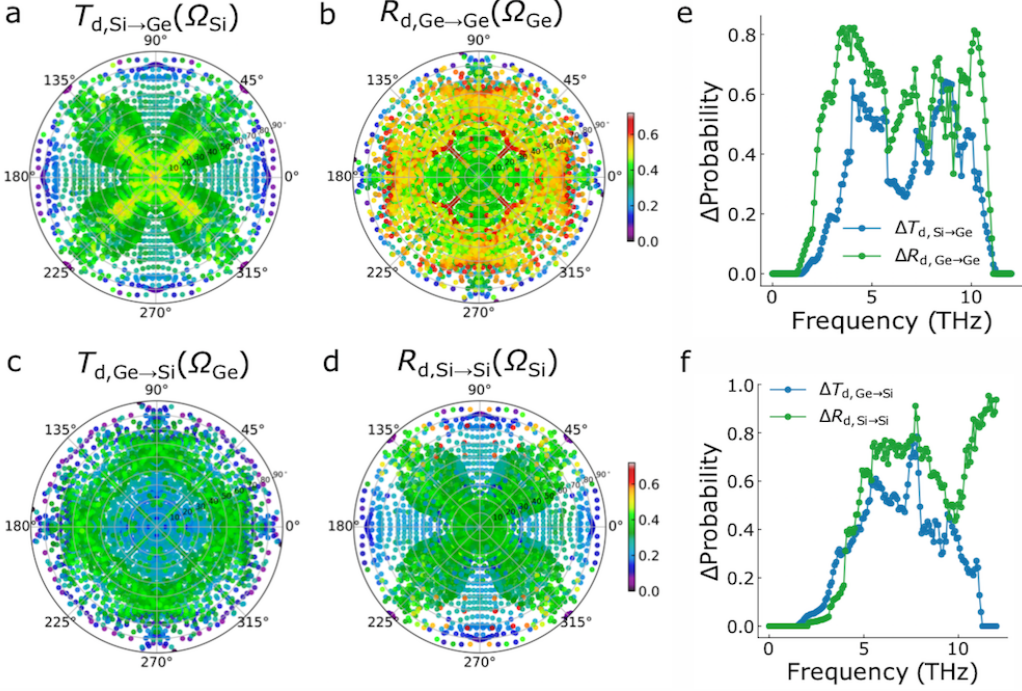


Figure 3-2: The angle-resolved (a) diffuse transmittance $T_{d,\text{Si}\rightarrow\text{Ge}}(\Omega_{\text{Si}})$ from the Si side and (b) diffuse reflectance $R_{d,\text{Ge}\rightarrow\text{Ge}}(\Omega_{\text{Ge}})$ from the Ge side at $\omega = 5$ THz. The angle-resolved (c) diffuse transmittance $T_{d,\text{Ge}\rightarrow\text{Si}}(\Omega_{\text{Ge}})$ from the Ge side and (d) diffuse reflectance $R_{d,\text{Si}\rightarrow\text{Si}}(\Omega_{\text{Si}})$ from the Si side at $\omega = 5$ THz. $\Omega_\alpha = (\theta_\alpha, \phi_\alpha)$, $\alpha = \text{Si}, \text{Ge}$ is the direction of incident group velocity. The radial coordinate corresponds to the polar angle θ_α (angle of incidence) and the polar axis corresponds to the azimuthal angle ϕ_α . (e), (f) The difference between maximum and minimum diffuse scattering probability as a measure of the anisotropy of diffuse scattering probability. The diffuse scattering probability is obtained by taking the ensemble average of calculations for 21 structures of 8 ml disordered configurations with a $20 \times 20 \mathbf{q}_{\text{sc},\parallel}$ -point mesh.

where $\alpha = L, R$. The specular transmittance and reflectance can be similarly defined.

Furthermore, to study the impact of diffuse phonon scattering on interfacial transport, we compute the transmission function $\Theta(\omega)$, which accounts for the total phonon conduction transmission at a given frequency ω , defined by,

$$\Theta(\omega) = \Theta_s(\omega) + \Theta_d(\omega) \quad (3.10)$$

$\Theta_s(\omega)$ and $\Theta_d(\omega)$ are specular and diffuse transmission function obtained by summing

over all possible incoming and outgoing states at a given frequency[119],

$$\begin{aligned}\Theta_s(\omega) &= \sum_{mn} T_{s,mn}^{L \rightarrow R}(\omega) \\ \Theta_d(\omega) &= \sum_{mn} T_{d,mn}^{L \rightarrow R}(\omega)\end{aligned}\tag{3.11}$$

The specular and diffuse reflection function is defined by,

$$\begin{aligned}\Xi_{s,\alpha}(\omega) &= \sum_{mn} R_{s,mn}^{\alpha \rightarrow \alpha}(\omega) \\ \Xi_{d,\alpha}(\omega) &= \sum_{mn} R_{d,mn}^{\alpha \rightarrow \alpha}(\omega)\end{aligned}\tag{3.12}$$

with $\alpha = L, R$. Note that the transmission function for two sides are the same due to the time-reversal symmetry of the transmission probability matrix but not for the reflection function.

3.2.3 Continuum modeling

In addition to the AGF simulation, we also derived analytical formulas for diffuse the transmittance and reflectance from continuum modeling with details provided in the Appendix B B. The model assumes scalar acoustic waves and random mass disorders distributed at the interface, and hence neglects mode conversion at the interface. The model is derived based on perturbation theory and it only takes the density ρ_L, ρ_R , bulk modulus μ_L, μ_R and number of pairs of swapped atoms per unit area n as parameters. The model captures the specific contributions to the total transmittance/reflectance of specular and diffuse scattering processes and allows one to calculate diffuse and specular transmittance and reflectance components analytically.

We assume a linear dispersion $\omega = c|\mathbf{q}|$, where the sound velocities for the left and right side are $c_L = \sqrt{\mu_L/\rho_L}$ and $c_R = \sqrt{\mu_R/\rho_R}$, respectively. Due to the simple dispersion relation, the transverse \mathbf{q}_{\parallel} can uniquely define a forward-moving phonon state. Thus, we use \mathbf{q}_{\parallel} and \mathbf{q}'_{\parallel} to denote the initial and final states, instead of using m and n . The momentum for a phonon state in the left side is $(\mathbf{q}_{\parallel}, q_L) = \frac{\omega}{c_L}(\sin\theta_L \cos\phi, \sin\theta_L \sin\phi, \cos\theta_L)$, where q_L is the perpendicular momentum. For a

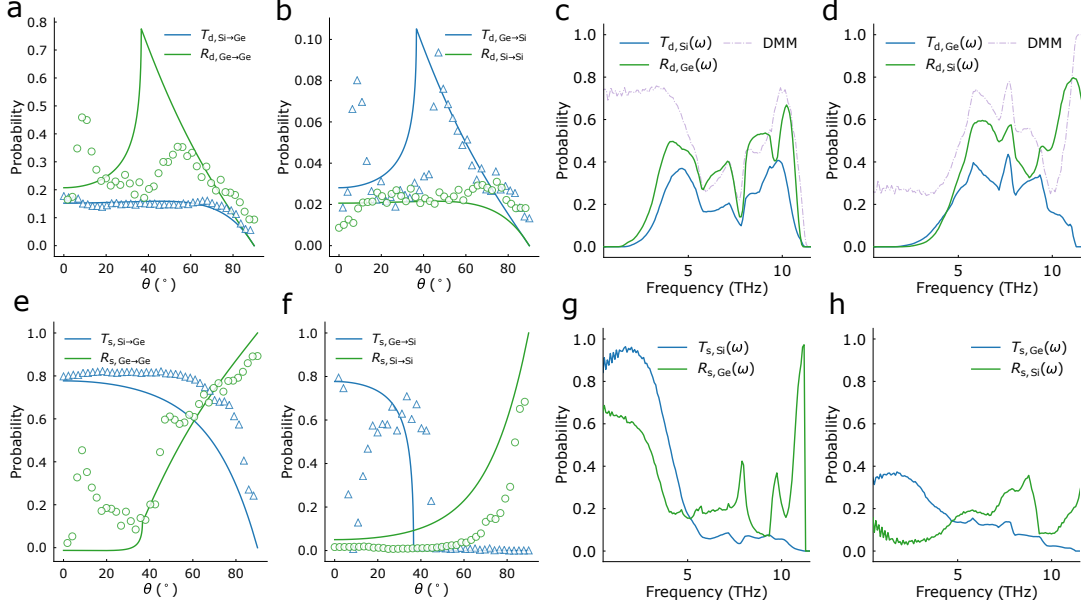


Figure 3-3: (a), (b) The diffuse transmittance $T_{d,\alpha}$ from one side and the diffuse reflectance $R_{d,\beta}$ from the other side as a function of the polar angle of the incident phonon at $\omega = 3.3$ THz. The markers are obtained by integrating $T_d(\Omega)$ and $R_d(\Omega)$ from AGF calculation for 8 ml structures over the azimuthal angle ϕ divided by 2π . The solid lines are predictions from continuum modeling with the number of pairs of swapped atoms per unit area $n = 2.78/a^2$ and $a = 5.527$ Å. (c), (d) The average diffuse transmittance $T_{d,\alpha}(\omega)$ from one side and the average diffuse reflectance $R_{d,\beta}(\omega)$ from the other side as a function of frequency from AGF calculation in solid lines, compared with DMM in dash-dot lines. (e)-(h) are the specular transmittance and specular reflectance corresponding to (a)-(d).

specular transmission process from the left side to the right side, the transverse momentum is conserved. Thus, the corresponding transmitted phonon state on the right side is $(\mathbf{q}_\parallel, q_R) = \frac{\omega}{c_R}(\sin\theta_R\cos\phi, \sin\theta_R\sin\phi, \cos\theta_R)$. It follows that the perpendicular velocities for the initial and final state are $v_L = c_L\cos\theta_L = c_L\sqrt{1 - c_L^2|\mathbf{q}_\parallel|^2/\omega^2}$, $v_R = c_R\cos\theta_R = c_R\sqrt{1 - c_R^2|\mathbf{q}_\parallel|^2/\omega^2}$, respectively.

From our continuum model, the diffuse transmittance for a given incident state from the left side writes,

$$T_{d,L \rightarrow R}(\omega, \Omega_L) = \int \frac{d^2\mathbf{q}'_\parallel}{(2\pi)^2} T_d^{L \rightarrow R}(\omega, \mathbf{q}'_\parallel, \mathbf{q}_\parallel) \quad (3.13)$$

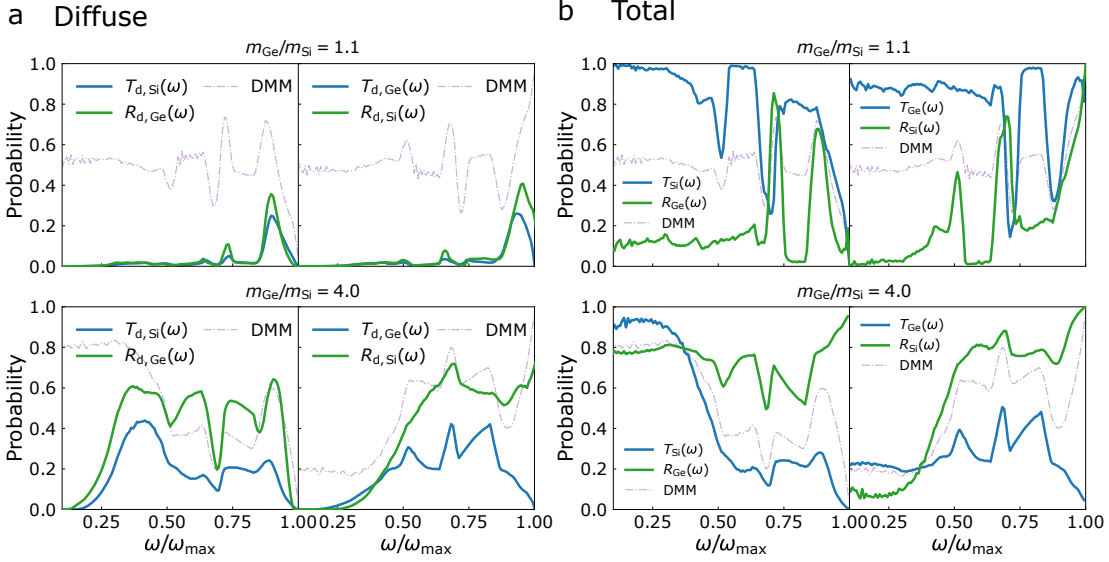


Figure 3-4: The frequency-resolved (a) diffuse and (b) total transmittance/reflectance from Si and Ge side with different $m_{\text{Ge}}/m_{\text{Si}}$ from AGF calculation for 8 ml structures and DMM. ω_{max} is the maximum allowed frequency for non-zero transmission function $\Theta(\omega)$. $\omega_{\text{max}} = 17.2$ THz when $m_{\text{Ge}}/m_{\text{Si}} = 1.1$, and $\omega_{\text{max}} = 9.1$ THz when $m_{\text{Ge}}/m_{\text{Si}} = 4.0$.

where

$$T_{\text{d}}^{L \rightarrow R}(\omega, \mathbf{q}'_{\parallel}, \mathbf{q}_{\parallel}) = 4\omega^{-2}V_2 \frac{\rho_R v'_R}{|\rho_L v'_L + \rho_R v'_R|^2} \frac{\rho_L v_L}{|\rho_L v_L + \rho_R v_R|^2} \quad (3.14)$$

Here, V_2 is a quantity related to density of mixed atoms at interface (see Appendix B B). Essentially, we have integrated over all possible final states \mathbf{q}'_{\parallel} on the right-hand side. Note that the final transverse momentum is bounded by $|\mathbf{q}'_{\parallel}| \leq \frac{\omega}{c_R}$.

The diffuse reflectance for a phonon state from the left-hand side is,

$$R_{\text{d},L \rightarrow L}(\omega, \Omega_L) = \int \frac{d^2 \mathbf{q}'_{\parallel}}{(2\pi)^2} R_{\text{d}}^{L \rightarrow L}(\omega, \mathbf{q}'_{\parallel}, \mathbf{q}_{\parallel}) \quad (3.15)$$

where

$$R_{\text{d}}^{L \rightarrow L}(\omega, \mathbf{q}'_{\parallel}, \mathbf{q}_{\parallel}) = 4\omega^{-2}V_2 \frac{\rho_L v'_L}{|\rho_L v'_L + \rho_R v'_R|^2} \frac{\rho_L v_L}{|\rho_L v_L + \rho_R v_R|^2} \quad (3.16)$$

and the transverse momentum of the final state is bounded by $|\mathbf{q}'_{\parallel}| \leq \frac{\omega}{c_L}$.

If we denote $F(\omega) = \int \frac{d^2\mathbf{q}_{\parallel}}{(2\pi)^2} 4\omega^{-2} V_2 \frac{\rho_L v'_L}{|\rho_L v'_L + \rho_R v'_R|^2}$, the diffuse transmittance from one side and the diffuse reflectance from the other side can be respectively expressed by,

$$T_{d,R \rightarrow L}(\omega, \Omega'_R) = \frac{\rho_R v'_R}{|\rho_L v'_L + \rho_R v'_R|^2} F(\omega) \quad (3.17)$$

$$R_{d,L \rightarrow L}(\omega, \Omega_L) = \frac{\rho_L v_L}{|\rho_L v_L + \rho_R v_R|^2} F(\omega) \quad (3.18)$$

It is evident that they are both anisotropic since they depend on perpendicular incident velocity. Their ratio writes,

$$\frac{T_{d,R \rightarrow L}(\omega, \Omega'_R)}{R_{d,L \rightarrow L}(\omega, \Omega_L)} = \frac{\rho_R v'_R}{\rho_L v_L} \frac{|\rho_L v_L + \rho_R v_R|^2}{|\rho_L v'_L + \rho_R v'_R|^2} \quad (3.19)$$

which is not a constant. Thereby, our continuum model suggests that the diffuse transmittance from one side and the diffuse reflectance from the other side are generally not equal.

3.3 Results and discussions

We study phonon transport through a disordered [001] Si/Ge interface by creating a 3×3 supercell (along x and y direction). We use the average of Si's and Ge's lattice constants, $a = 5.527 \text{ \AA}$, as the lattice constant in generating the supercell structures and the Stillinger-Weber inter-atomic potential to compute the dynamical matrix and Green's function[120]. The interface is constructed by randomly swapping Si and Ge atoms with the same distances to the interface and the further away from the interface the fewer atoms are swapped. At even further distances from the interface, no Si and Ge atoms are swapped. For instance, when we have 2 layers of Si and 2 layers of Ge atoms are mixed, 2 pairs of Si and Ge atoms will be swapped in the Si and the Ge layer closest to the interface and 1 pair of Si and Ge atoms will be swapped in the Si and the Ge layer secondly closest to interface. In this case, we have a 1|2|2|1 configuration, with each number denoting the number of swapped atoms within the

same layer. We label such interface structure by 4 ml, in short for 4 mixing layers in total. Apparently, a larger ml number means a larger degree of disorder. We generate 21 configurations for each given total mixing layers and compute the ensemble average of the transmission and reflection probability matrix $T_{mn}^{L \rightarrow R}(\omega)$, $T_{mn}^{R \rightarrow L}(\omega)$, $R_{mn}^{L \rightarrow L}(\omega)$ and $R_{mn}^{R \rightarrow R}(\omega)$.

We first examine the angular dependence of ensemble-averaged diffuse transmittance and reflectance at a given frequency to ascertain whether or not they are isotropic. In Fig. 3-2, we find strong angle dependence of diffuse transmittance and diffuse reflectance from the Si side as well as the Ge side, contradicting the assumption of isotropic reflectance and transmittance underlying the DMM. The diffuse reflectance from Ge to Ge is found to be overall higher than the diffuse transmittance from Si to Ge. The diffuse reflectance from Si to Si is in a similar range compared with the diffuse transmittance from Ge to Si, although their explicit angle dependences are drastically different.

If the DMM is valid, the diffuse transmittance from one side and the diffuse reflectance from the other side should be isotropic. We compute the difference between the maximum and minimum scattering probability at different frequencies, as a measure of anisotropy, shown in Fig. 3-2 (e) and (f). We observe that the diffuse scattering probability generally varies in a wide range. For example, the diffuse reflectance from the Si side at high frequencies ranges almost from zero to one. Hence, we conclude the diffuse transmittance and reflectance from both sides are highly anisotropic.

Additionally, we find out that the patterns of diffuse transmittance and diffuse reflectance do not have two perfect diagonal reflection axes as the perfect Si/Ge [001] interface structure does. This is the consequence of ensemble average of disordered structures, where each structure might have broken the reflection symmetry, and it is not guaranteed to recover the original symmetry after ensemble average. Still, we can clearly observe a clover-like pattern for the diffuse transmittance and reflectance from the Si side, which originates from the pmm symmetry of the phonon bands for a perfect [001] Si/Ge interface.

In particular, to quantitatively study how the diffuse transmittance and diffuse

reflectance depend on the polar angle, we integrate the angle-dependent scattering probability over the azimuthal angle. As shown in Fig. 3-3 (a), at $\omega = 3.3$ THz, the diffuse transmittance from Si is lower than the reflectance from Ge, while in Fig. 3-3 (b), the diffuse transmittance from Ge is higher than the diffuse reflectance from Si. It is interesting to note that the continuum model agrees well with the results from AGF when incident states are from Si, suggesting the model captures the physics of diffuse phonon scattering. On the contrary, the continuum model predicts a different diffuse scattering probability profile compared with the calculation from AGF when incident phonons are from Ge. From the analytical expression in the continuum model for diffuse scattering probability (Eq. 3.13 and Eq. 3.15), we learn that the peak in diffuse transmittance and reflectance profile corresponds to the critical angle for total internal reflection (37 degrees). In comparison, the scattering probability profile from AGF has two peaks (9 degrees and around 50 degrees). In Fig. 3-3 (e) and (f), we find that the specular transmittance and reflectance have a much stronger dependence on the polar angle compared with their diffuse counterparts. Our continuum model for specular scattering probabilities again shows good agreement with the AGF calculation except incapable of capturing the multiple peaks arising from total internal reflection. Note that the continuum modeling is based on a scalar field, where the polarization vectors are not included. The difference between continuum modeling and AGF calculation suggests that without considering mode conversion among different polarizations, the scalar continuum model cannot accurately describe the actual number of available diffuse transmission and reflection pathways.

To study the diffuse transmittance at different frequencies, we define an average diffuse transmittance for phonon modes with the same frequency by,

$$T_{d,\alpha}(\omega) = \frac{\sum_n^+ T_{d,n}^{\alpha \rightarrow \beta}(\omega) v_{z,n}}{\sum_n^+ 1 \cdot v_{z,n}} = \frac{\Theta_d(\omega)}{\Theta_{\text{bulk},\alpha}(\omega)} \quad (3.20)$$

where $v_{z,n}$ is the group velocity normal to the interface. $\Theta_{\text{bulk},\alpha}(\omega)$ is the transmission function for bulk material α (we use two leads and device all consisting of α atoms in AGF calculation). The average total transmittance including specular transmittance

and diffuse transmittance is defined by, $T_\alpha(\omega) = \frac{\Theta(\omega)}{\Theta_{\text{bulk},\alpha}(\omega)}$. The average diffuse and total reflectance are $R_{d,\alpha}(\omega) = \frac{\Xi_{d,\alpha}(\omega)}{\Theta_{\text{bulk},\alpha}(\omega)}$ and $R_\alpha(\omega) = \frac{\Xi_\alpha(\omega)}{\Theta_{\text{bulk},\alpha}(\omega)}$, respectively. Note that the sum of transmittance and reflectance is one, yet the sum of diffuse transmittance and diffuse reflectance is less than one, as not all phonons are diffusely scattered. On the other hand, the sum of transmittance and reflectance given by DMM is always unity. Therefore, when we compare the diffuse transmittance/reflectance with transmittance/reflectance by DMM, it is entirely possible their values do not match. However, what we are more interested in answering is whether or not the phonon loses its memory, *i.e.*, whether the diffuse transmittance from one side equals the diffuse reflectance from the other side[121].

In Fig. 3-3 (c), we find that the diffuse transmittance from Si is lower than the diffuse reflectance from Ge for all frequencies. They both deviate from DMM given by Eq. 3.4 at low frequencies. At high frequencies, the DMM's prediction is close to the reflectance from Ge. In Fig. 3-3 (d), the diffuse transmittance from Ge is lower than reflectance from Si except for low frequencies. And they are both different from DMM. The crossing point at 4.4 THz for transmittance and reflectance suggest that at this frequency, the average transmittance from Ge side is the same with average diffuse reflectance from Si side, although they individually have strong angle dependence. The gap between diffuse transmittance from one side and diffuse reflectance from the other side suggests that diffuse phonon scattering depends on the initial state such that phonons actually do not lose their memory of origin. In Fig. 3-3 (g) and (h), we see that the specular scattering probability is generally much higher than the diffuse scattering probability at low frequencies, suggesting that at low frequencies, the interface scattering is almost all specular. This trend is also consistent with previous findings[108, 122].

An important factor that is relevant to the diffuse phonon scattering is the amount of dissimilarity between two materials. According to Pohl and Swartz[8], DMM predicts that diffuse scattering increases thermal boundary resistance of the interface between similar solids, suggesting that diffuse scattering plays a significant role when the mass ratio between the two materials is close to one. In Fig. 3-4, we present the

frequency-resolved transmittance and reflectance with different mass ratios $m_{\text{Ge}}/m_{\text{Si}}$ (we fix the mass m_{Si} and vary the mass m_{Ge}). We find that when the two sides are similar, the diffuse transmittance from one side is similar to the diffuse reflectance from the other side. This partially aligns with the assumptions of DMM, although the diffuse transmittance and diffuse reflectance still have strong anisotropy in directions (see Fig. 6 in the supplementary material in Ref. [76]). When the mass ratio is large, the transmittance from one side is no longer similar to the reflectance from the other side, indicating that the scattering probability strongly depends on where the initial states are from. As for the total transmittance and reflectance, due to the inclusion of the specular scattering probability, the difference between transmittance from one side and reflectance from the other side is enlarged. It is interesting to note that when two sides are similar, although DMM cannot correctly describe either scattering probability, it is close to the average of the total transmittance from one side and the total reflectance from the other side. When the two sides are dissimilar, the DMM's prediction becomes similar to the total transmittance in Ge side at low frequencies and the total transmittance in Si side at high frequencies. This suggests that for certain cases, DMM is able to roughly describe the total transmittance from one side in a certain frequency range but not for all frequencies.

To study how much memory the phonon loses regarding its origin in a quantitative manner, we define a similarity measure by,

$$S_\beta(\omega) = \exp\left(-\frac{|T_{d,\alpha}(\omega) - R_{d,\beta(\omega)}|}{R_{d,\beta}(\omega)}\right) \quad (3.21)$$

where $T_\alpha(\omega)$ is the diffuse transmittance from one side and $R_\beta(\omega)$ is the diffuse reflectance from the other side, and the final states for these scattering processes are on the β side. $S_\beta \rightarrow 1$ means high similarity between the diffuse transmittance and reflectance when the final state is on the β side, *i.e.* phonon completely loses its memory of origin. $S_\beta \rightarrow 0$ means low similarity between the diffuse transmittance from one side and diffuse reflectance from the other side, and phonon does not lose its memory. A large mass ratio generally lead to a smaller similarity measure. We

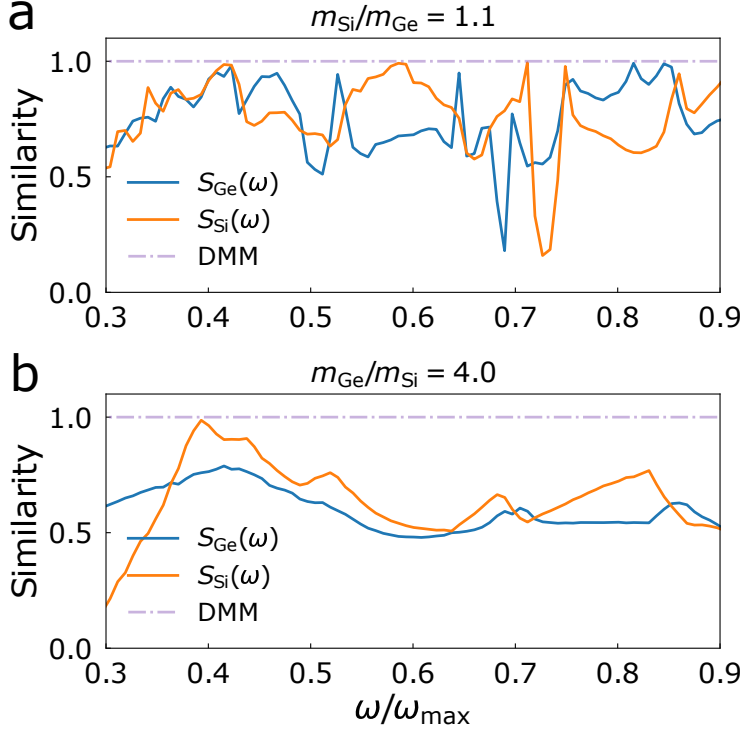


Figure 3-5: The similarity between the diffuse transmittance from one side and the diffuse reflectance from the other side. The blue lines correspond to the cases when the final states are on the Ge side and the orange lines correspond to the cases where the final states are on the Si side. The diffuse transmittance and reflectance for evaluating the similarity are from the data presented in Fig. 3-4 (a).

also find that the similarity measure depends which side the final state resides at. For example, in Fig. 3-5 (b), we find that at $\omega = 0.39\omega_{\max}$, when phonon is scattered into Si side, it loses its memory. However, this is not true when phonon is scattered into Ge side. In comparison, for DMM, the similarity is always one when the final states are on either side of the interface.

Lastly, we want to discuss the diffuse phonon scattering's role in interfacial transport. In Fig. 3-6 (a), we plot the total transmission function as a function of frequency with different numbers of mixing layers. And we find that the total transmission can either be enhanced or reduced compared with the perfect Si/Ge interface as a result of the competition between the specular transmission versus diffuse transmission. From Fig. 3-6 (b) and (c), we find as the degree of disorder increases, the specular transmission decreases while the diffuse transmission increases. In other words, the

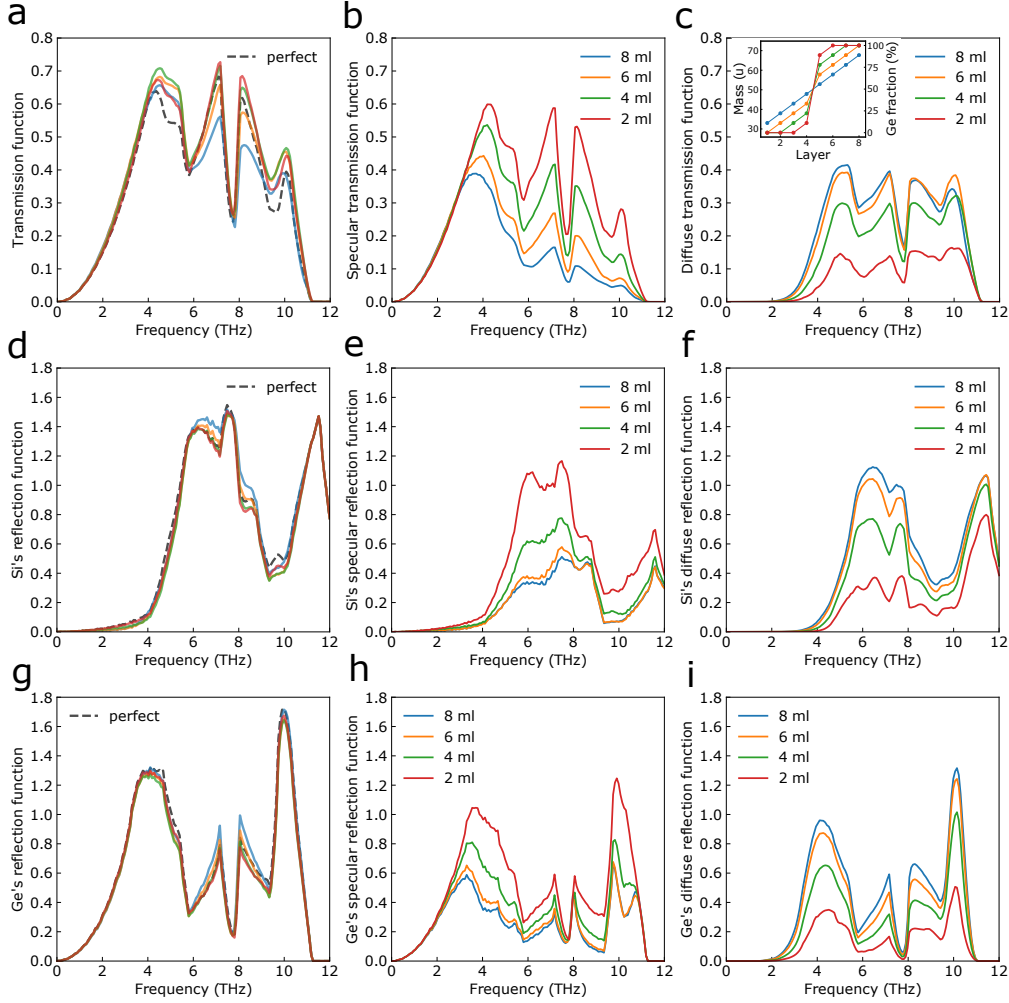


Figure 3-6: (a) The total transmission function, (b) the specular transmission function and (c) the diffuse transmission function versus phonon frequency for [001] Si/Ge interfaces from AGF. Inset: the ensemble-averaged mass profile as a function of atom layer number at the interface region obtained by averaging the mass of atoms within the same layer. The right axis is the Ge fraction in each atom layer. The distance between adjacent atom layers is $a/4 = 1.382 \text{ \AA}$. (d)-(f) The total, specular and diffuse reflection function from the Si side. (g)-(i) The total, specular and diffuse reflection function from the Ge side.

disorders remove specular channels while creating new diffuse channels. As a result, we do not observe significant changes in the transmission function due to atomic mixing. The opposite trends for specular and diffuse transmission versus the degree of disorder eventually leads to the maximum thermal conductance for 4 ml structures. It is interesting to note that similar enhancements for transmission enabled by disor-

ders have been discovered in electron transport in heterostructures[55]. From Fig. 3-6 (d)-(i), we learn that the increasing amount of disorders always reduce the specular reflection function and increases the diffuse reflection function. Thus, the disorders can both increase the diffuse transmission (enhancing the interface conductance) and the diffuse reflection (worsening the interface conductance). This competition is another reason why we cannot observe significant enhancement of thermal conductance by disorders. Our current analysis is based on elastic scattering, yet phonon anharmonicity can contribute to interfacial transport by enabling “vertical coupling” between conduction channels of different frequencies. There are several works on understanding the anharmonicity’s role in thermal interface conductance for abrupt interfaces[123, 124, 125, 126], but how diffuse scattering and anharmonicity affect heat conduction channels remains unclear.

3.4 Conclusion

Through AGF calculation, we have demonstrated that the diffuse phonon scattering by a single disordered interface depends both on initial incoming states as well as the final outgoing states. The transmittance and reflectance strongly depend on the polar angle of group velocity. Also, the transmittance from one side and reflectance from the other side are generally different. That is to say, phonons do not lose their memory after diffuse scattering by a single interface. When two materials are similar, the diffuse transmittance from one side and the diffuse reflectance from the other side become similar to each other. However, the total transmittance from one side and total reflectance from the other side are still different.

The number of specular transmission channels for interfacial transport is always reduced by interfacial disorders while new transmission channels are created by diffuse phonon scatterings. The competing roles of specular and diffuse transmission can lead to either enhanced or reduced transmission function and interfacial thermal conductance.

We also derived the expressions for transmittance and reflectance for diffuse scat-

tering processes based on the continuum approximation, which works reasonably well in the low-frequency range. The model leads to different analytical expressions for diffuse transmittance from one side and diffuse reflectance from the other side. Our model also shows that the diffuse transmission opens up new transmission channels even for those states above the critical angle for total internal reflection.

Chapter 4

Phonon Anderson localization in aperiodic superlattices

4.1 Introduction

The ability to control phonon is of great importance in manipulating nanoscale thermal transport[1] and delaying quantum decoherence in quantum information science[21]. Phonons in certain disordered nanostructures with feature sizes similar to phonon wavelength experience Anderson localization[14], where the phonons stay spatially localized due to strong constructive wave interferences. Several theoretical studies on phonon Anderson localization show that random mass disorders cause the exponentially decaying transmittance with system length[127, 128, 129, 130, 131].

However, experimental observation of phonon Anderson localization is difficult because of the broadband nature of phonons and strong phase-destroying inelastic scattering. Additionally, for three-dimensional materials, the number of available propagating paths can easily surpass the number of localized paths. Phonon Anderson localization has only been experimentally observed in superlattices with random dots below 50 K[19]. However, the required extremely low temperature greatly limits the application of Anderson localization.

To experimentally observe phonon Anderson localization at higher temperatures, we propose several strategies. We need atomic-scale interface roughness that scat-

ters high-frequency phonon efficiently. The roughness cannot be too large, otherwise the diffusive interface scattering will destroy the phases for remaining phonons. In addition, we use alloy to further remove high-frequency phonons' contribution to transport. More importantly, we use aperiodicity as a type of disorder to induce strong interference among scattered waves. The interfaces in aperiodic structure also strongly scatter phonons with middle wavelengths.

We experimentally demonstrate that phonon Anderson localization exists up to 200 K in aperiodic Si/Si_{0.2}Ge_{0.8} superlattices. Our simulation shows that high-frequency phonons are strongly scattered by interface roughness and alloys, while low-frequency phonons form constructive interferences and their transmittance exponentially decay with system length. The thermal conductivity from simulation and optical measurements both show a peak in its length dependence curve, a unique feature attributed to Anderson localization. At higher temperatures, the phonon interferences are destroyed by phonon-phonon scattering and thermal conductivity monotonically increases with length, where phonon transport is in the classical ballistic-diffusive regime. Our work validates the theoretical understanding of phonon wave-particle duality as well as the universality of Anderson localization of waves. It also provides a simple yet practical strategy to dynamically convert propagating phonons to localized phonons.

4.2 One-dimensional scalar phonon modeling

According to the scaling theory of localization by Abrahams *et. al.*[132], electron is always localized in one-dimensional disordered systems at $T = 0$ K. For phonon transport within the coherence length l_c , such argument also applies. However, how the localization length depends on different phonon modes and the degree of disorder remains unknown. In the section, we conduct one-dimensional scalar phonon modeling to answer these questions.



Figure 4-1: The schematic for one-dimensional aperiodic structures in the transfer matrix calculation.

4.2.1 Formalism

We simulate the transmission coefficients for scalar phonons through randomly aperiodic superlattices using transfer matrix method. The details of the transfer matrix method can be found in Ref. [133]. We outline the methodology for the sake of completeness in the following.

As shown in Fig. 4-1, the first and the last layer, A_0 and A_N , are both semi-infinite made of material A. For the rest of the layers, the layer thickness $A_i, B_i \in [L_1, L_2]$ are randomly chosen for each layer according to a uniform distribution function. We denote the starting and the ending position for layer B_i with x_i and x'_i and thus we have $L_1 \leq x'_i - x_i \leq L_2$. The index i ranges from 1 to $N - 1$ for material A and from 1 to N for material B. The standard deviation for the layer thickness of two media are $\sigma_A, \sigma_B = \frac{L_2 - L_1}{\sqrt{12}}$. The average layer thickness for A and B are $l = \frac{L_1 + L_2}{2}$. The phonons within the layer A_0 can be expressed in terms of plane waves, $\Psi_{A_0} = a_{A_0}e^{ik_A x} + b_{A_0}e^{-ik_A x}$, where the wavevector magnitude is $k_A = \frac{\omega}{c_A}$ (we consider normal incidence) and $c_A = \sqrt{\mu_A/\rho_A}$ is the group velocity (μ_A is the bulk modulus). On the other end of the structure, we have the plane-wave solution, $\Psi_{A_N} = a_{A_N}e^{ik_A x} + b_{A_N}e^{-ik_A x}$. The coefficients in front of plane waves for the N th layer and the 0 th layer are related via,

$$\begin{pmatrix} a_{A_N} \\ b_{A_N} \end{pmatrix} = \begin{pmatrix} M_{11} & M_{12} \\ M_{21} & M_{22} \end{pmatrix} \begin{pmatrix} a_{A_0} \\ b_{A_0} \end{pmatrix} \quad (4.1)$$

where the two-by-two matrix is the transfer matrix and its matrix elements are related to the transmission and reflection coefficients, $M_{11} = \frac{1}{t_{N0}^*}$, $M_{21} = -\frac{r_{N0}^*}{t_{N0}^*}$, $M_{21} = -\frac{r_{N0}}{t_{N0}}$ and $M_{22} = \frac{1}{t_{N0}}$. The transmission and reflection probability are, $T_{N0} = |t_{N0}|^2$ and $R_{N0} = |r_{N0}|^2$.

Specifically, the transfer matrix is the product of the transfer matrix associated

with each interface and Eq. 4.1 can be expressed by,

$$\begin{pmatrix} a_{A_N} \\ b_{A_N} \end{pmatrix} = \mathbf{h}^*(\phi'_{A_N}) \mathbf{M}_N \mathbf{h}(\alpha_{A_{N-1}}) \mathbf{M}_{N-1} \mathbf{h}(\alpha_{N-2}) \cdots \mathbf{M}_2 \mathbf{h}(\alpha_{A_1}) \mathbf{M}_1 \mathbf{h}(\phi_{A_1}) \begin{pmatrix} a_{A_0} \\ b_{A_0} \end{pmatrix} \quad (4.2)$$

where the matrices \mathbf{M}_i and \mathbf{h} read,

$$\mathbf{M}_i = \begin{pmatrix} e^{i\alpha_{B_i}} \cosh^2 \gamma - e^{-i\alpha_{B_i}} \sinh^2 \gamma & 2i \sin \alpha_{B_i} \cosh \gamma \sinh \gamma \\ -2i \sin \alpha_{B_i} \cosh \gamma \sinh \gamma & e^{-i\alpha_{B_i}} \cosh^2 \gamma - e^{i\alpha_{B_i}} \sinh^2 \gamma \end{pmatrix} \quad (4.3)$$

$$\mathbf{h}(\alpha_{A_i}) = \begin{pmatrix} e^{i\alpha_{A_i}} & 0 \\ 0 & e^{-i\alpha_{A_i}} \end{pmatrix} \quad (4.4)$$

with the phase $\phi'_{A_N} = ik_A x'_{A_N}$ and $\phi_{A_1} = ik_A x_{A_1}$, the phase shift in each layer $\alpha_{B_i} = k_B(x'_i - x_i)$, $\alpha_{A_i} = k_A(x_{i+1} - x'_i)$, $\sinh \gamma = \frac{1}{2} \left(\sqrt{Z} - \frac{1}{\sqrt{Z}} \right)$ and the acoustic impedance $Z = \frac{\rho_B c_B}{\rho_A c_A}$. We further denote the average phase shifts $\alpha_X = \langle \alpha_{X_i} \rangle$ with $X = A, B$ and the corresponding standard deviation $\sigma_X = (\langle \alpha_{X_i}^2 \rangle - \langle \alpha_{X_i} \rangle^2)^{1/2}$.

Conventionally, the localization constant is defined by the logarithm of the transmission amplitude divided by the number of layers[134],

$$\lambda = -\frac{1}{N} \ln(|t_{N0}|) \quad (4.5)$$

where N is the number of B layers. The inverse of the localization constant describes after how many layers phonons are almost fully localized. We can also compute the localization length by multiplying the average layer thickness,

$$\xi = -\frac{N(l_A + l_B)}{\ln(T_{N0})} = \frac{l}{\lambda} \quad (4.6)$$

The localization constant can be analytically computed. The analytical expression

for the localization constant writes[133],

$$\lambda = \begin{cases} \frac{1}{2} \frac{\sin^2 2\gamma}{1-a_r^2} (\sin^2 \alpha_A \sigma_B^2 + \sin^2 \alpha_B \sigma_A^2), & \omega < \omega_c \\ 2 \ln(\cosh \gamma), & \omega \geq \omega_c \end{cases} \quad (4.7)$$

where $a_r = \cos \alpha_A \cos \alpha_B - \sin \alpha_A \sin \alpha_B (\cosh^2 \gamma + \sinh^2 \gamma)$ and the critical frequency ω_c is the crossing point of the two expressions. It is easy to show that with increasing impedance Z , the localization constant is rapidly increasing (localized in a shorter length scale).

The above expressions are applicable to normal incidence. For oblique incidence from A_0 , one can simply change the acoustic impedance Z with

$$Z(\theta) = \frac{\rho_B c_B \sqrt{1 - \frac{c_B^2}{c_A^2} \sin^2 \theta}}{\rho_A c_A \sqrt{1 - \sin^2 \theta}} \quad (4.8)$$

where θ is the incident angle.

The transmission function can be computed by,

$$\Theta(\omega) = \pi A D_A(\omega) c_A \int_0^1 \sin \theta T_{N0}(\omega, \sin \theta) d\sin \theta \quad (4.9)$$

where A is the transverse cross-sectional area, $D_A(\omega) = \frac{\omega^2}{2\pi^2 c_A^3}$ is the phonon density of states and $T_{N0}(\omega, \sin \theta) = e^{-2N\lambda(\sin \theta)}$ is the transmission probability. The thermal conductance G can be computed using Landauer-Büttiker formalism mentioned in Chapter 1 and the thermal conductivity is given by $\kappa = GL$.

4.2.2 Results and discussions

From the analytical expression in Eq. 4.7, we learn that the localization length is highly sensitive to the impedance Z . We list the localization lengths in the strong-disorder regime ($\omega > \omega_c$) for common superlattices in Table 4.1. The impedance for Si/Ge and Si/Si_{0.2}Ge_{0.8} are slightly larger than that of AlAs/GaAs. However, their inverse localization constants are over one order of magnitude smaller than that

Table 4.1: The Anderson localization length at normal incidence

Materials	$\rho_A(\text{kg/m}^3)$	$c_A(\text{m/s})$	$\rho_B(\text{kg/m}^3)$	$c_B(\text{m/s})$	$Z(\circ)$	$[\lambda(\omega > \omega_c)]^{-1}$
Si/Ge	2333	8433	5323	5400	1.4610	28.00
Si/Si _{0.2} Ge _{0.8}	2333	8433	4725	5732	1.3765	39.34
AlAs/GaAs	3720	6400	5320	4730	1.0569	1305

of AlAs/GaAs. If the inverse localization constant (or localization length) is too large, it can be even longer than the inelastic mean free path such that the phase-destroying phonon-phonon interaction makes localization disappear. Thus, the exponential decay of thermal conductance due to phonon Anderson localization in Si/Ge or Si/Si_{0.2}Ge_{0.8} is potentially much easier to observe experimentally with shorter samples.

In Fig. 4-2 (a), we find the localization length decreases with increasing frequency at low frequencies and phonons at low frequencies are in the weak-localization regime ($\omega < \omega_c$). In particular, the localization length diverges with ω^{-2} when $\omega \rightarrow 0$. At higher frequencies, the phase shift at each layer is greater and the interferences among scattering paths are enhanced. The strong interferences lead to the strong localization regime, where the localization length ξ becomes independent of the frequency. The numerical results agree nicely with the analytical expression thus we use the analytical expression for localization length in the following calculation.

We observe that the angle of incidence has a strong impact on the localization length, shown in Fig. 4-2 (b). This is because the impedance $Z(\theta)$ increases with incident angle θ thus it becomes easier to localize phonons within a shorter distance with high incident angles. At the same incident angle, the higher frequency corresponds to stronger phase shifts and interferences, thus a smaller localization length. Moreover, changing incident angle can also trigger the transition from weak localization to strong localization because the effective impedance changes drastically.

We present the thermal conductivity versus length with different degree of disorder at 300 K in Fig. 4-2 (c). We can identify similar trends with slightly changed the maximum layer thickness L_2 . In the strongly localized regime, the localization length is independent of frequencies and the configurations, thus the conductance is almost

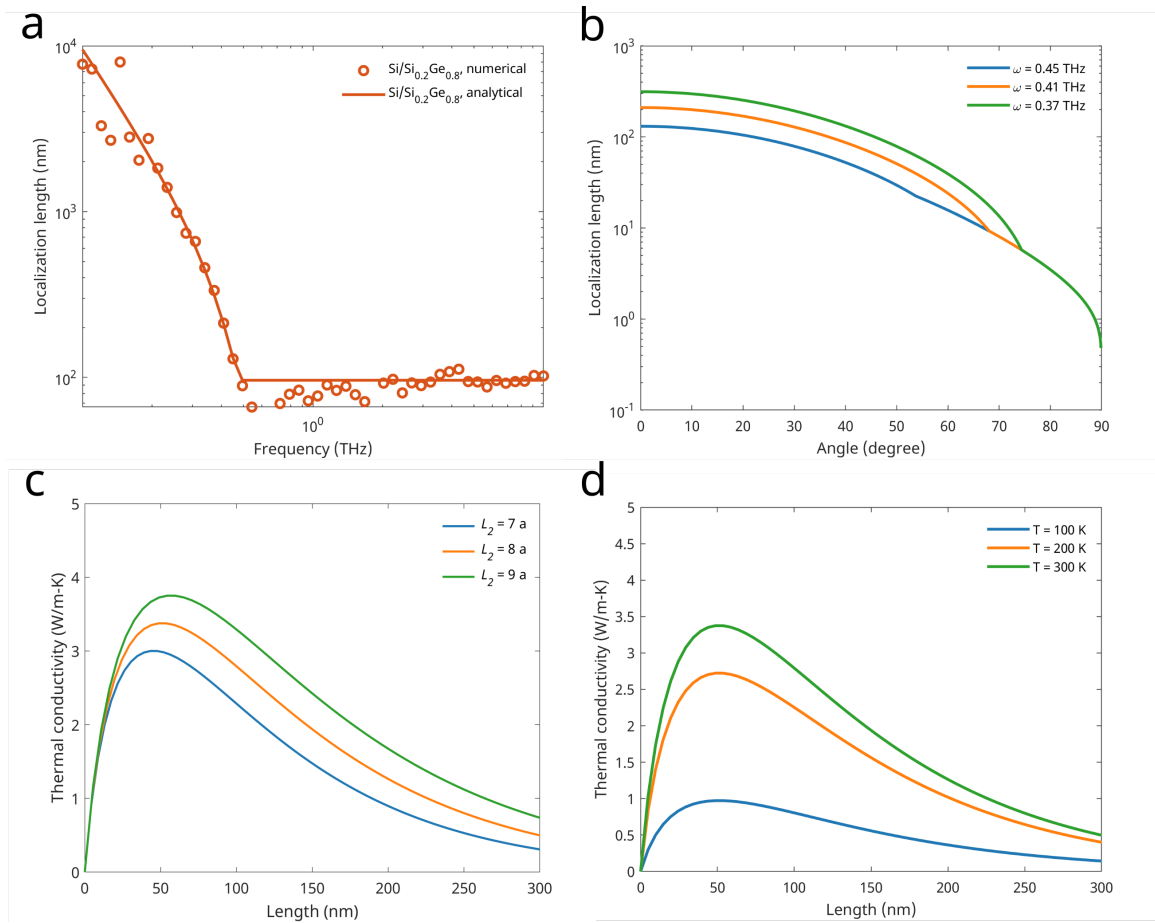


Figure 4-2: (a) The localization length in the weak-disorder and strong-disorder regime. The dots are from numerical transfer matrix calculation and the solid line is from the analytical expression. (b) The localization length versus the incident angle. (c) The length-dependent thermal conductivity with different maximum layer thickness L_2 at 300 K. (d) The length-dependent thermal conductivity at different temperatures. In all calculations, $L_1 = a$, where a is the lattice constant of Si. In (a), (b) and (d), $L_2 = 8a$. A degeneracy factor of 3 for phonon density of states is multiplied when evaluating the thermal conductivity.

independent of the degree of disorder. As a result, the thermal conductivity is higher with a larger average layer thickness.

In Fig. 4-2 (d), we show the thermal conductivity versus length at different temperatures. At high temperatures, high-frequency phonons are excited, and those phonons are in strong localization regime thus the significant decay of thermal conductivity can be observed. At low temperatures, those low-frequency phonons that are only weakly localized contribute the most to transport, thus the thermal conductivity decay is slower than high temperatures.

The scalar phonon model is essentially a toy model that enables us to conduct an order of magnitude analysis and understand the angular and frequency dependence of localization lengths. However, such model has several limitations. First, it cannot describe phonon polarization, which means that the scattering between different phonon branches are neglected. Second, only acoustic phonons are included and the optical phonons are neglected, which can overestimate the thermal conductivity since the acoustic phonons usually have higher group velocities than optical phonons. Last but not least, the interface roughness, which is commonly seen in practical heterostructures, is neglected. The interface roughness changes phonon transport through layered structure from 1D to 3D, where phonons are more difficult to be localized according to the scaling theory[132, 34]. We are interested in predicting the emergence of Anderson localization quantitatively thus a more rigorous method is needed.

4.3 Atomistic Green's function simulation

We use the atomistic Green's function introduced in Chapter 3 to study the thermal conductivity in aperiodic superlattices, which includes specific atomic structures, full phonon dispersion relations and interface roughness. We choose Si and Ge atoms to construct the superlattice due to their large mass contrast (large impedance). However, Si and Ge have a large lattice mismatch hence making the Si/Ge superlattice difficult to realize in experiment. Therefore, we choose the $\text{Si}/\text{Si}_x\text{Ge}_{1-x}$ rather than Si/Ge , which greatly reduces the induced strain. The alloys structure of $\text{Si}_x\text{Ge}_{1-x}$

can significantly scatter high-frequency phonons and reduce their contribution to transport, as those phonons usually have small inelastic mean free paths and are difficult to localize.

We randomly choose the layer thickness for Si and $\text{Si}_{0.2}\text{Ge}_{0.8}$ within the range, $L \in [L_{\min}, L_{\max}]$, where the minimal layer thickness $L_{\min} = a$ and a is Si's lattice constant¹. In Fig. 4-3, we compare the thermal conductivity as a function of the total length with different maximal layer thickness L_{\max} . In the $\text{Si}_{0.2}\text{Ge}_{0.8}$ alloy layer, the Si and Ge atoms are randomly distributed according to the atomic fraction. The solid line are the fitted curves to the expression proposed by Wang *et. al.*[135],

$$\kappa(L) = G_0 \frac{\Lambda L}{\Lambda + L} \exp\left(-\frac{L}{\zeta}\right) \quad (4.10)$$

where G_0 is a characteristic thermal conductance, Λ can be interpreted as the phonon mean free path and ζ is the decaying length of the thermal conductance (half the phonon localization length ξ). We find that although the thermal conductivity fluctuates among specific disordered configurations, the length dependence of thermal conductivity follows the same trend indicated by the above expression. At short length scale, the phonon travels coherently with very weak back scattering due to the limited number of interfaces. When the number of interfaces increases, the multiple possible scattering paths are interfering with each other. In the disordered layered medium with increasing layer number, although the number of theoretically available paths increases, the number of paths that allows the phonon to travel through all layers is much smaller than those paths that let phonon come back. Whenever we have a path that allows phonon travel relatively far from its origin, there is always a time-reversal path available for phonon to come back. Such pair of time-reversal paths form constructive paths, and boost reflection probability while reducing transmission probability. This makes the transmission probability exponentially decay with increasing number of interfaces. Thus, the thermal conductivity starts to decrease according to the scaling $Le^{-L/\zeta}$ at the large length L . Since the transport transits from ballistic

¹We have assumed the $\text{Si}_{0.2}\text{Ge}_{0.8}$ has the same lattice constant of Si.

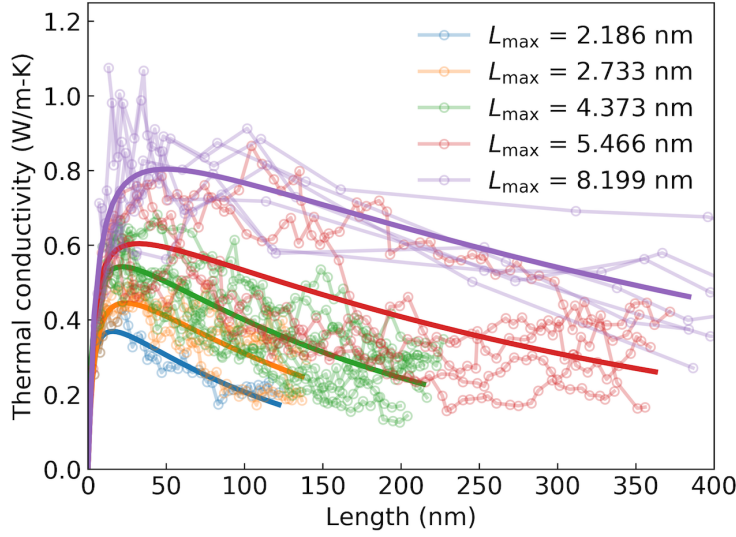


Figure 4-3: Thermal conductivity of Si/Si_{0.2}Ge_{0.8} aperiodic superlattices with different L_{\max} . The dots correspond to random configurations for a given L_{\max} . The solid lines are the fitted curve using the expression $\kappa = \frac{aL}{b+L} e^{-L/c}$.

transport to the localized transport, there is a peak in thermal conductivity versus length curve.

The phonon-phonon interaction is a phase-destroying process which can let the interference disappear. The inelastic mean free path, which describes the average traveling distance before being scattered by other phonons, is a measure of the inelastic scattering strength. A larger inelastic mean free path suggests weaker inelastic scatterings. We compare the *ab initio* phonon-phonon scattering mean free path with the mode-resolved localization length $\xi = -2L/\ln|T_i(L)|$, where $T_i(L)$ is the transmission probability for phonon state i through the sample of length L at 200 K². From Fig. 4-4, we find that the localization length generally decreases with increasing frequency. The localization length is generally smaller than the inelastic mean free path except near 4 THz and 6 THz, suggesting the localization is weakly affected by the inelastic scattering. The inelastic mean free path scales with temperature $\Lambda_{\text{in}} \propto 1/T$ while the localization is temperature-independent. Thus, with increasing tempera-

²The inelastic mean free path data is provided by Qian Xu and the detail for the computation can be found in Ref.[136].

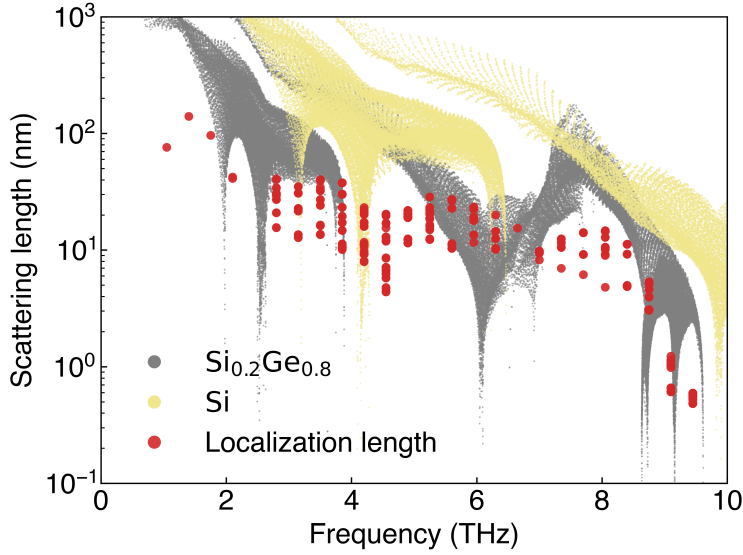


Figure 4-4: The mode-resolved localization length compared with the inelastic mean free path due to phonon-phonon scattering with $L_{\max} = 8a$ at 200 K.

tures, the inelastic effect becomes predominant and localization will be eventually destroyed by those inelastic scattering processes.

In Fig. 4-5, we specifically study a specific disordered configuration with $L_{\max} = 8a$. We find that the interface roughness has a minor effect in thermal conductivity. We also separate the contributions of specular transmission and diffuse transmission to the conductance. Accordingly, the specular and diffuse thermal conductivity is obtained by product of the length and the corresponding conductance. We find that the diffuse thermal conductivity decreases faster than the specular thermal conductivity. With a longer length, the thermal conductivity is mainly due to specular phonons. That is to say, the incident and outgoing phonons has to have the same transverse momentum, although the alloy structures inside the sample never has the corresponding transverse symmetry. This is because the high-frequency phonons are also diffuse, and their localization lengths are generally smaller. After several layers, those high-frequency phonons are fully localized. The remaining low-frequency phonons are all specularly transmitted phonons. In periodic superlattice, the interface roughness strongly scatters high-frequency phonons but cannot localize phonons. Thus, eventually, some phonons (especially low-frequency phonons) can transmit through the

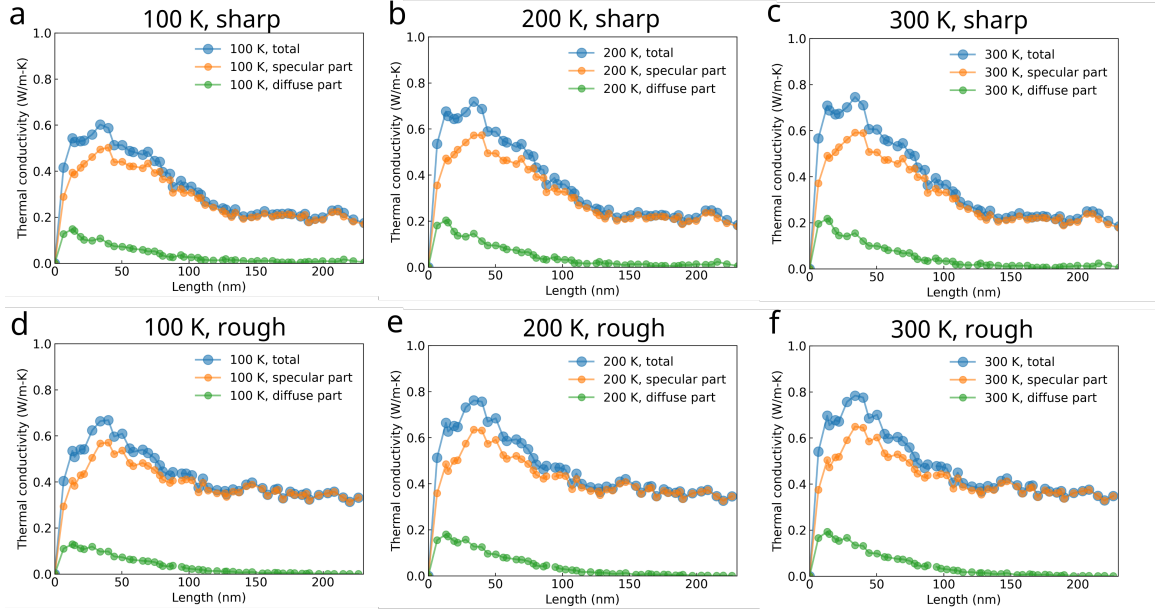


Figure 4-5: The specular and diffuse thermal conductivity versus length with $L_{\max} = 8a$ with and without interface roughness. We use a 2×2 transverse cell with 2 ml structure for rough interfaces.

periodic superlattices, and they can be either specular or diffuse. However, using aperiodic system above certain thickness can guarantee that outgoing phonons have the same transverse momentum as incident phonons. In a way, we create more order in transport using more disorders.

The peaks in the length dependence curve of thermal conductivity from various calculations give us confidence that it might be possible to observe the Anderson localization in such aperiodic system experimentally. In particular, the calculation indicates that the decay of thermal conductivity happens at very small L , which means that we can potentially observe the peak of thermal conductivity with several short samples that are easy to grow.

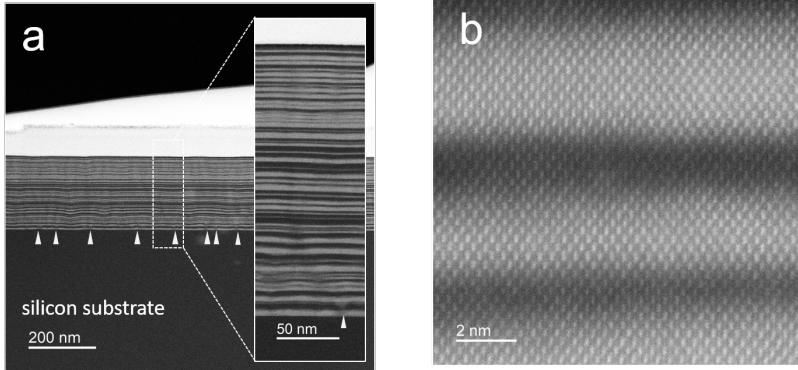


Figure 4-6: The STEM image for aperiodic samples grown on Si substrate using molecular-beam epitaxy.

4.4 Experimental validation

4.4.1 The sample preparation

We provide the atomic structures used in the atomistic Green's function calculation for Fig. 4-5 to Rui Pan and Professor Hong Lu, and they use molecular-beam epitaxy to grow four aperiodic superlattice samples with different number of layers on Si substrates. From the scanning transmission electron microscope image shown in Fig. 4-6, we found that the aperiodicity is clearly visible and the interface is not atomically flat. However, from our calculation, we learn that a modest amount of interface roughness do not destroy Anderson localization. We proceed to measure the thermal conductivity of thin films using optical characterization methods.

4.4.2 Frequency-domain thermoreflectance

We choose the frequency-domain thermoreflectance method to measure the length dependence of thermal conductivity. The Si and Ge have relatively large penetration depths (larger than sample thickness) for light absorption, which induces complicated electron-phonon interactions and carrier generations and combinations, and makes the heat transfer analysis complicated. We thus sputter a gold thin film of 96 nm on top of the aperiodic film to absorb the laser power to heat up the sample. The frequency-domain thermoreflectance setup situated at NanoEngineering lab is built by Aaron

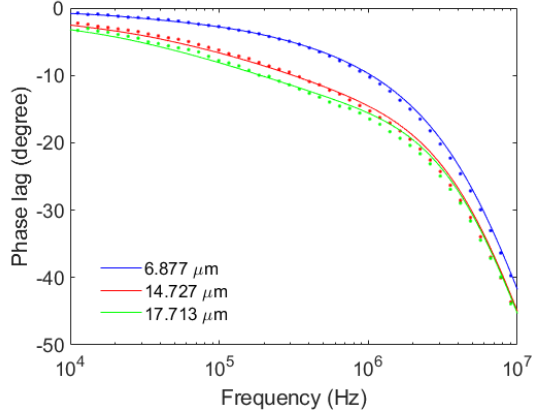


Figure 4-7: Representative frequency-domain thermoreflectance signals with different radii for the sample with 22.5 nm total thickness at $T = 260$ K.

Schmidt. It has a 405 nm pump with modulation frequency ranging from 5 KHz to 50 MHz. A 532 nm probe is used to probe the reflectance change due to temperature change. In experiment, we use pump power of 20 mW and a probe power of 5 mW. More details of the instrument can be found in Ref. [137].

In Fig. 4-7, we show the FDTR signals for the same sample with different pump beam radii. The phase lag describes the phase angle of the complex temperature responses on the metal surface. We fit the data with the same thermal transport properties and with different radii. The initial guess for beam radii can be known from the beam offset measurement.

In Fig. 4-8 (a), we have shown the length dependence of thermal conductivity from FDTR measurements at temperatures less or equal to 200 K. The curves are the fitting results using Eq. 4.10. The peaks in thermal conductivity versus length curves are a strong evidence of Anderson localization. At 200 K, the thermal conductivity is almost not changing with system length. In Fig. 4-8 (b), we show the thermal conductivity at higher temperatures. The thermal conductivity all increases with length, which is a feature of incoherent classical size effect.

If we plot the thermal conductivity for different samples versus temperature, we find that the thermal conductivity of the longest sample has very low thermal conductivity compared with shorter samples below 200 K. However, its thermal conductivity suddenly increases to become the highest among all samples above 200 K. The curve

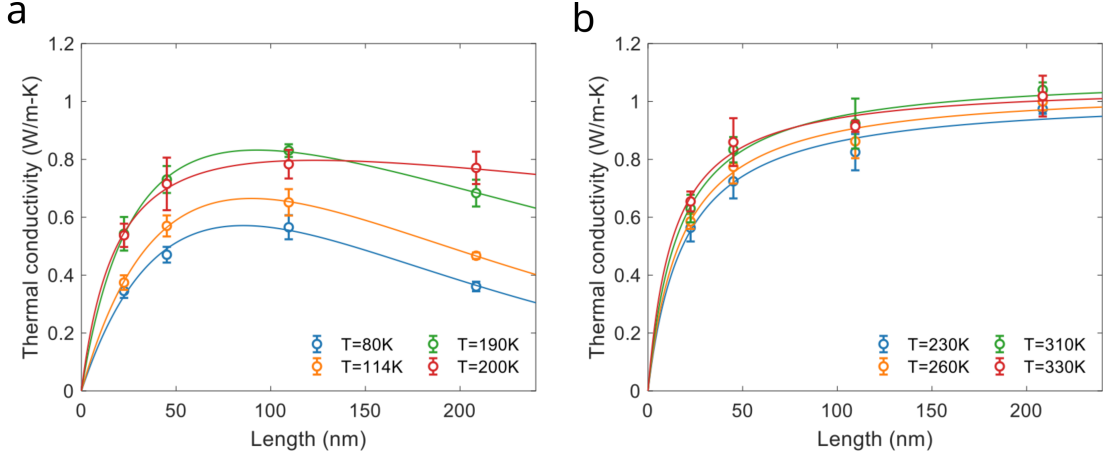


Figure 4-8: The thermal conductivity measured by FDTR in aperiodic layered medium versus length (a) at low temperatures and (b) at high temperatures.

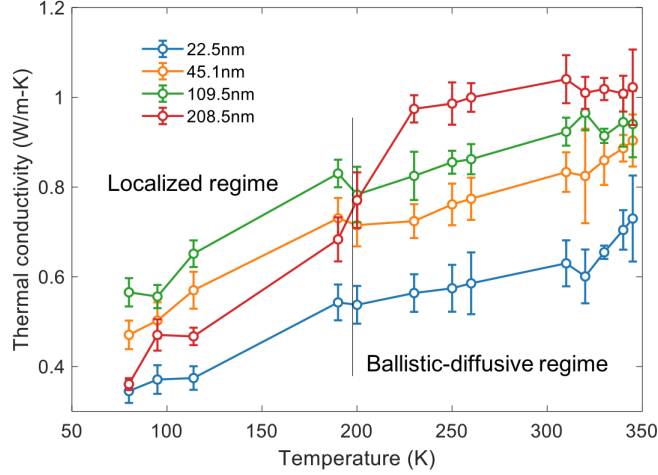


Figure 4-9: The thermal conductivity of different aperiodic samples versus temperature.

of κ versus T has crossings with other samples. The crossings suggest the transition from localized transport at low temperature and ballistic-diffusive transport at high temperatures. Thus, we conclude that the Anderson localization exists up to 200 K.

4.5 Conclusion

We have studied the phonon Anderson localization in aperiodic superlattices with scalar phonon modeling, atomistic Green's function simulation and frequency-domain thermoreflectance method. We learn that a larger acoustic impedance of the two con-

structive materials can lead to a smaller localization length. In Si/Si_{0.2}Ge_{0.8} aperiodic superlattices, the alloying scattering effectively scatter high-frequency phonons and make the low-frequency phonons dominate the transport. The simulations and experiments both show the peak in thermal conductivity, which is a strong evidence of Anderson localization. We also experimentally find the localization-delocalization temperature is around 200 K. Our work provides insights in using aperiodicity to manipulate phonons in practical applications such as thermoelectrics and quantum computing.

Chapter 5

Transient thermal grating measurement for thin films

5.1 Introduction

Pump-probe spectroscopy is a robust and versatile technique to characterize the thermal transport properties of bulk materials, thin films as well as the interfaces. The essential idea is to use the pump beam to heat up the sample, which causes temperature changes, and to use the probe beam to detect the surface reflectance change due to the temperature change ($\frac{\Delta R}{R} \propto \Delta T$). Since the temperature change dynamics is determined by the thermal transport properties, we can extract the values of the transport properties via proper fitting based on thermal modeling.

Time-domain thermoreflectance (TDTR), frequency-domain thermoreflectance (FDTR) and transient thermal grating (TTG) are three prevalent optical canalization techniques for thermal transport measurements. The TDTR technique uses an ultra-fast laser pulse as pump and another delayed pulse as probe[138, 139, 140]. The FDTR technique uses a frequency-modulated continuous-wave (CW) pump and a CW probe to probe temperature responses in the frequency domain. In these two techniques, the beam profiles are all Gaussian in the in-plane directions, so is the spatial heating profile. Moreover, after the pump pulses, electron excitation, electron-phonon coupling and phonon thermal conduction happen in different yet overlapped time ranges

of the whole equilibrium process, which brings challenges to distinguish the part of the signal that are actually due to thermal conduction. To ensure the signal is solely determined by thermal transport, people often coat a metallic transducer layer on top of the sample when conducting TDTR and FDTR measurements, since the electronic responses are very fast compared with the lattice responses.

The TTG, on the other hand, uses an entirely different heating geometry[141, 142, 143, 144]. It sends two pulsed pump beams that interfere and form a sinusoidal heating grating on sample surface, and sends the probe to the same grating with a time delay (or a CW probe with constant power). The surface temperature perturbation has a sinusoidal profile with periodic temperature peaks and valleys, which diffracts the probe beam with spatially-varying diffraction efficiency. As the heat dissipates horizontally, the temperature difference between the temperature peak and valley decreases and the decay of temperature difference encodes the thermal transport properties. Compared with TDTR and FDTR, the simple changes in the heating geometry in TTG completely change the heat transfer dynamics, making the TTG are more sensitive to in-plane thermal transport. In addition, the grating period for the heating profile is tunable via changing the phase mask. That is to say, the distance between the periodic “heat source” (the temperature peak) and the “heat sink” (the temperature valley) is tunable. This effectively determines how long it takes to reach thermal equilibrium. When the grating period length is longer, the heat dissipation takes longer time. By properly choosing the grating period length, it is possible to separate the non-thermal responses (electron diffusion, electron-phonon coupling, and carrier recombination) and thermal responses (phonon transport), thus it allows measuring the thermal conductivity in certain materials without the need for the metallic transducer.

For instance, the in-plane thermal conductivity of graphite[145] and Si membrane[144] have been directly measured with TTG in the transmission geometry without the metallic transducer layer, where the pump and probe beam transmit through the whole sample and the heat dissipation can be regarded as an ideal two-dimensional thermal transport process. However, a lot of thin film samples, whose in-plane ther-

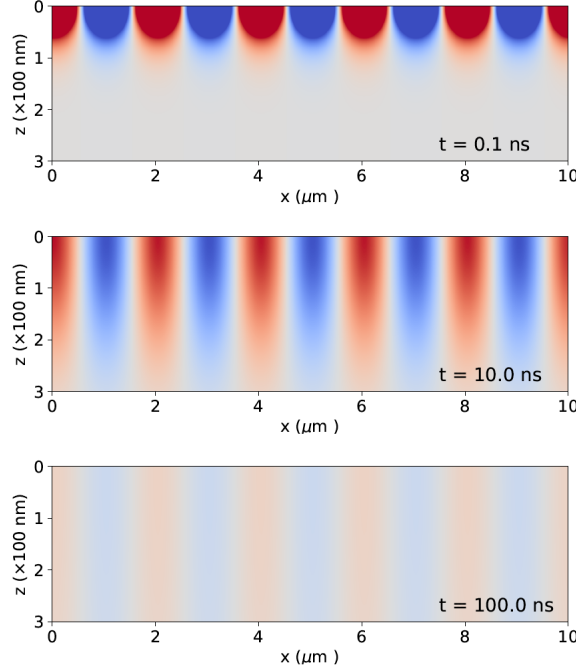


Figure 5-1: Representative temperature distribution snapshots in TTG experiments in a semi-infinite bulk sample. The color refers to the temperature change with respect to the background temperature. The z direction is pointing from the material surface to the inner region of the material. Initially, the temperature change at the surface is a sinusoidal function. As time evolves, the contrast of the temperature peaks and temperature valleys is weakened due to the heat transport both along the in-plane direction and the cross-plane direction (z direction).

mal conductivity is of interest, have thickness of ~ 100 nm and are grown on substrate. In this case, it is impossible to conduct TTG measurements in transmission geometry. Meanwhile, using TDTR or FDTR with transducer often has a limited sensitivity of in-plane thermal conductivity. Nevertheless, one can use the TTG with reflection geometry as illustrated in Fig. 5-1. Yet, there are rarely reports and analysis on using TTG with reflection geometry to measure thermal conductivity of thin films grown on substrate[141]. In this Chapter, we present the methodology of utilizing the TTG to measure thermal conductivity of thin films with single-layer or multiple-layer geometry. Such method allows the measurement for layered samples with any number of layers without the transducer, which serves as an alternative for TDTR and FDTR methods.

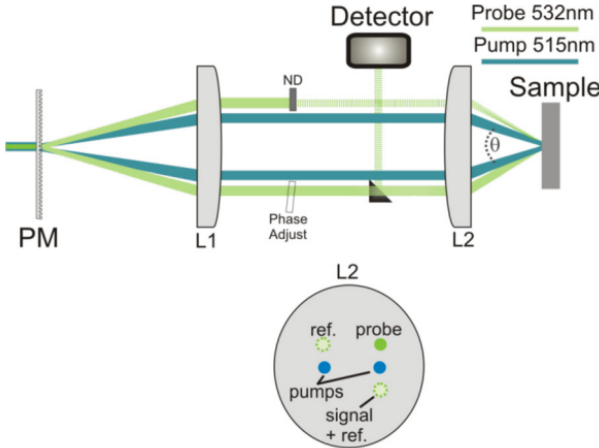


Figure 5-2: The optical configuration for heterodyne detection of transient thermal grating. Reprinted from Ref. [147].

5.2 Methodology

5.2.1 Phase-controlled, heterodyne TTG

The TTG setup is at NanoEngineering lab at MIT, and it was built by Bai Song and Ke Chen with the support of Professor Keith Nelson's group and modified by Jungwoo Shin and me. We adopt the phase-controlled, heterodyne TTG configuration, where the signal generally contains the contributions of temperature rises as well as the surface displacements[142, 143]. As shown in Fig. 5-2, in the reflection setup, a pump beam is first split into two beams by the phase mask. We block high-order diffraction beams and only keep the two first-order diffracted beams. The two beams are focused on sample surface after two lenses and form constructive interferences, serving as the transient grating. Similarly, another two beams split by the phase mask, called the probe beam and the reference beam, are focused on sample surface. The probe beam is diffracted by the thermal grating caused by pump and encodes information of the temperature rise. Usually, the intensity of the diffracted beam is weak, because the diffraction efficiency is proportional to the square of the material excitation amplitude I^2 ($I \ll 1$)[146].

To amplify the diffracted probe signal, we use the reference beam reflected by the thermal grating, which is collinear with the diffracted probe beam, to form coherence

between the diffracted probe and the reflected reference beam. The resulting output signal I_S writes[142],

$$I_S = I_R + I_D + 2\sqrt{I_R I_D} \cos\theta \quad (5.1)$$

where I_R and I_D are the reflected reference beam's intensity and diffracted probe beam's intensity, and θ is the phase difference between their associated electromagnetic fields. Generally, the reflected reference beam has a much higher intensity than the diffracted beam, $I_R \gg I_D$. Thus, the second term in Eq. 5.1 is negligible. The first term is almost a constant. The third term is amplified compared with I_D by a factor of $\sqrt{\frac{I_R}{I_D}} \gg 1$. We denote the third term the heterodyne signal I_{het} . By introducing a phase shift in the probe beam to tune θ , we can measure two different sets of output intensities I_S . After subtracting the two intensities, we remove the constant part and only the third term remains. We effectively obtain the signal that is solely proportional to $I_{\text{het}} \propto \sqrt{I_R I_D}$.

Next, we examine how to extract the temperature responses from the heterodyne signal. Johnson *et. al.* show that the heterodyne diffraction signal satisfies[143],

$$I_{\text{het}} \propto |r_0|^2 \{ r'(t) \cos\theta - [r''(t) - 2k_p u(t) \cos\beta_p] \sin\theta \} \quad (5.2)$$

where k_p and β_p are the wavevector and incident angle for the probe beam, $r(t) = r_0 [1 + r'(t) + ir''(t)]$ is the dynamic complex reflection coefficient, r_0 is the intrinsic reflection coefficient without transient grating and $u(t)$ is the surface displacement. When the phase θ is tuned to be 0 or $\pm\pi$, the corresponding signal is only related to $r'(t)$. For a lot of materials, we have $r'(t) \propto \Delta T(t)$, where $\Delta T(t)$ is the temperature difference between the peaks and valleys of the sinusoidal temperature profile and we call the such grating the amplitude grating. In the actual measurement, we will measure two heterodyne signals at $\theta = 0$ and $\theta = \pi$ and subtract the two signals. The resulting signal satisfies, $\Delta I_{\text{het,amplitude}} \propto \Delta T(t)$. If the phase difference θ is tuned to be $\pi/2$ and $-\pi/2$, the signal is related to $u(t)$ and $r''(t)$. If we subtract these two signals, the obtained signal satisfies $\Delta I_{\text{het,phase}} \propto A\Delta T + u(t)$, where A is an unknown constant. In this case, it is not a trivial task to separate the temperature

responses from the displacement responses. For certain materials (*e.g.* graphite), the temperature effect on $r''(t)$ is small such that $A \rightarrow 0$, and the signal is thus dominated by the surface displacement $u(t)$. Conventionally, we call the grating with $\theta = \pm\pi/2$ the phase grating. The signal from amplitude grating and phase grating have distinctive features. The surface displacement is often rapidly oscillating with time, whereas the signal for amplitude grating is smoothly decaying with time. Since the amplitude grating is directly related to temperature, in the following, we are focused on the TTG with amplitude grating.

5.2.2 The heat transfer model for layered medium

We have established the understanding of the necessity of heterodyne detection and the dependence of heterodyne diffraction signal on the temperature difference $\Delta T(t)$ between the temperature peaks and the valleys. In this section, we model the surface temperature $\Delta T(t)$ under the spatially periodic heating. To start with, we need to consider the optical absorption of the pump beam in the depth direction.

The electrons within the optical absorption depth are instantaneously heating up and the temperature of the lattice rises later due to electron-phonon interaction. We express the heat source term as,

$$P(t, x) = P_0(t) e^{iqx} e^{-\xi z} = \frac{1}{2\pi} \int P_0(\omega) e^{iqx} e^{-\xi z} e^{i\omega t} d\omega \quad (5.3)$$

where ξ is inverse penetration depth and $P_0 \approx \frac{j\xi}{A(1-e^{-\xi L})}$ with L the thickness of top layer, A the beam cross-sectional area, $q = \frac{2\pi}{\lambda}$ is the wavevector for the grating, λ is the grating period length and j is the pump laser power in Watt. The heat equation writes,

$$\nabla \cdot (\kappa \nabla T) + P(t, x) = \rho C \frac{\partial T}{\partial t}, \quad (5.4)$$

where T is the temperature rise with respect to the background temperature. The temperature rise will follow the expression, $T = \tilde{T}(\omega, q, z) e^{i(\omega t + qx)}$. Plugging the

temperature rise expression into Eq. 5.4, we obtain the expression for \tilde{T} ,

$$\tilde{T}(\omega) = \tilde{T}_0(\omega) + \frac{P_0(\omega)}{\kappa_z(\beta^2 - \xi^2)} e^{-\xi z}, \quad (5.5)$$

and the heat flux in cross-plane direction is,

$$\tilde{Q}(\omega) = \tilde{Q}_0(\omega) + \frac{\xi P_0(\omega)}{\beta^2 - \xi^2} e^{-\xi z}, \quad (5.6)$$

Here, $\tilde{T}_0(\omega) = Ae^{-\beta z} + Be^{\beta z}$ is the solution to Eq. 5.4 when there is no volumetric heating ($P(\omega) = 0$), $\beta = \sqrt{(q^2\kappa_x + i\rho C\omega)/\kappa_z}$ and κ_x and κ_z are the in-plane and cross-plane thermal conductivity. The boundary condition for surface ($z = 0$) is adiabatic as convection and radiation are negligible, thus $\kappa_z(\beta A - \beta B) = -\frac{\xi P_0(\omega)}{\beta^2 - \xi^2}$. The surface temperature is $\tilde{T}_{sf}(\omega) = A + B + \frac{P_0(\omega)}{\kappa_z(\beta^2 - \xi^2)}$. The bottom temperature and heat flux of the first layer writes,

$$\begin{aligned} \tilde{T}_1 &= Ae^{-\beta L} + Be^{\beta L} + \frac{P_0(\omega)}{\kappa_z(\beta^2 - \xi^2)} e^{-\xi L} = \cosh(\beta L)\tilde{T}_{sf}(\omega) \\ &+ \left[\frac{\sinh(\beta L)}{\kappa_z \beta} - \frac{\cosh(\beta L)}{\kappa_z \xi} + \frac{e^{-\xi L}}{\kappa_z \xi} \right] \frac{\xi P(\omega)}{\beta^2 - \xi^2} \end{aligned} \quad (5.7)$$

$$\begin{aligned} \tilde{Q}_1 &= \kappa_z \beta A e^{-\beta L} - \kappa_z \beta B e^{\beta L} + \frac{\xi P_0(\omega)}{\beta^2 - \xi^2} e^{-\xi L} \\ &= -\kappa_z \beta \sinh(\beta L) \tilde{T}_{sf}(\omega) \\ &+ \left[\frac{\beta}{\xi} \sinh(\beta L) - \cosh(\beta L) + e^{-\xi L} \right] \frac{\xi P(\omega)}{\beta^2 - \xi^2} \end{aligned} \quad (5.8)$$

In matrix form, the above equations can be expressed by,

$$\begin{pmatrix} \tilde{T}_1 \\ \tilde{Q}_1 \end{pmatrix} = \begin{pmatrix} \cosh(\beta L) & -\frac{\sinh(\beta L)}{\kappa_z \beta} + \frac{\cosh(\beta L)}{\kappa_z \xi} - \frac{e^{-\xi L}}{\kappa_z \xi} \\ -\kappa_z \beta \sinh(\beta L) & -\frac{\beta}{\xi} \sinh(\beta L) + \cosh(\beta L) - e^{-\xi L} \end{pmatrix} \begin{pmatrix} \tilde{T}_{sf} \\ \frac{\xi P(\omega)}{\xi^2 - \beta^2} \end{pmatrix} \quad (5.9)$$

For the remaining layers, the expression for the transfer matrix can be found in Sec. C.1.3 as long as we assume the volumetric heating is only happening within the top layer. When the top layer is made of metal which usually has a small penetration depth, this is a good assumption. The temperature and heat flux at the external

surface of the last layer satisfy,

$$\begin{pmatrix} \tilde{T}_n \\ \tilde{Q}_n \end{pmatrix} = \begin{pmatrix} a & b \\ c & d \end{pmatrix} \begin{pmatrix} \tilde{T}_{sf} \\ \frac{\xi P(\omega)}{\xi^2 - \beta^2} \end{pmatrix} \quad (5.10)$$

For adiabatic boundary condition at the external surface of the last layer (negligible convection and radiation), the surface temperature of the top layer can be expressed by,

$$\tilde{T}_{sf} = -\frac{d}{c} \frac{\xi P(\omega)}{\xi^2 - \beta^2} \quad (5.11)$$

Alternatively, for zero temperature (relative to background temperature) boundary condition at the bottom layer, the surface temperature rise can be expressed by,

$$\tilde{T}_{sf} = -\frac{b}{a} \frac{\xi P(\omega)}{\xi^2 - \beta^2}. \quad (5.12)$$

$\tilde{T}_{sf}(\omega)$ is equal to the Fourier transform of temperature difference between temperature peak and valleys $\Delta T(\omega)$. The above-mentioned two boundary conditions generally give the same results for surface temperature.

High-frequency limit At extremely high frequencies, the signal should converge to the heat conduction in semi-infinite slab. After adopting the adiabatic boundary condition for the bottom surface, the top surface temperature reads,

$$\begin{aligned} \tilde{T}_{sf}(\omega \rightarrow \infty) &= - \left[-\frac{\tanh(\beta L)}{\kappa_z \beta} + \frac{1}{\kappa_z \xi} - \frac{\exp(-\xi L)}{\kappa_z \xi \sinh(\beta L)} \right] \frac{\xi P(\omega)}{\xi^2 - \beta^2} \\ &\approx \frac{1}{\kappa_z \beta^2} P(\omega) = -\frac{P(\omega)}{\rho C \omega} i. \end{aligned} \quad (5.13)$$

Thus, the phase will goes to $-\frac{\pi}{2}$. On the other hand, we have assumed that for the initial heating profile is instantaneous. In fact, it takes time to build such heating profile and the characteristic time for electron-phonon interaction can be up to 100 ps. In this case, one can assume $P(t)$ with a finite width and plug the corresponding Fourier transform $P(\omega)$ into Eq. 5.11 or Eq. 5.12.

Semi-infinite limit For single-layer medium, the surface temperature is,

$$\tilde{T}_{\text{sf}}(\omega) = \frac{-\frac{\beta}{\xi} \sinh(\beta L) + \cosh(\beta L) - e^{-\xi L}}{\sinh(\beta L) \kappa_z \beta} \left. \frac{\xi P(\omega)}{\xi^2 - \beta^2} \right|_{L \rightarrow \infty}. \quad (5.14)$$

When ξ is large (close-to-zero penetration depth),

$$\tilde{T}_{\text{sf}}(\omega) \approx \frac{1}{\kappa_z \beta} \frac{P(\omega)}{\xi} = C e^{i\theta}. \quad (5.15)$$

where $\theta = -\text{atan}\left(\frac{\rho C \omega}{q^2 \kappa_x}\right)/2$. Essentially, the phase angle θ changes from 0 to $-\pi/4$ as ω changes from 0 to ∞ .

5.3 Results and discussions

We conduct the TTG in the reflection geometry for two types of thin film samples and apply the heat transfer model to extract the thermal conductivity of the thin film. Specifically, we study the thermal conductivity in correlated oxide thin film V₂O₃, which experiences insulator-metal transition at low temperatures and in GaAs/AlAs digital-alloy superlattices with ErAs quantum dots randomly inserted near interfaces.

5.3.1 Thermal conductivity in correlated oxide thin films

Metal-insulator transition has been observed in correlated oxide thin films such as VO₂ and V₂O₃. Such transition can be triggered by temperature changes or external voltage changes in company with structural deformation. The metal-insulator transition has been used in neuromorphic computing and resistive memories[148, 149].

The V₂O₃ sample is provided by Dr. Yoav Kalcheim from Professor Ivan K. Schuller's research group at University of California San Diego. The thin films are grown on sapphire substrates with different crystal orientations with thickness of 126 nm, one cut at the r plane and one cut at the a plane, denoted r-cut and a-cut, respectively. The electrical conductivity has been measured by Dr. Yoav Kalcheim, as shown in Fig. 5-3. The two samples both experience insulator-metal transition at

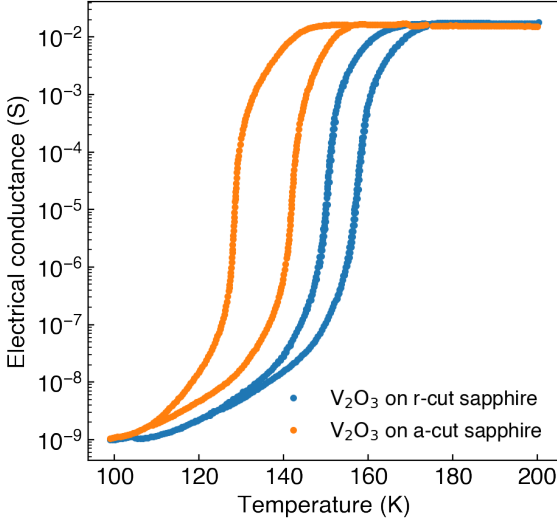


Figure 5-3: The electrical conductance for thin films with different crystal orientations.

low temperatures. The hysteresis feature suggests that the transition has a memory of the past physical states, which is the key for neuromorphic computing[150]. The crystal orientation has a large impact on the transition temperature. The transition temperature of the r-cut sample is around 150 K while the transition temperature for the a-cut sample is around 130 K. Such tunability in the transition temperature create new opportunities in memristive device. Since the electron transport shows strong dependence on crystal orientation, we are eager to answer the following question: How does the crystal orientation of thin films impact the thermal transport?

We used pulsed pump with duration time of 180 fs of 515 nm and a continuous-wave (CW) probe beam of 532 nm. The pump fluence is 1.29 mJ/cm² (estimated corresponding temperature rise on the order of ~ 10 K) and the probe power is 3.6 mW. The inverse penetration depth is computed from the reports on dielectric constants[151]. The heat capacity of oxide film, the thermal conductivity and heat capacity of substrate sapphire are all taken from literatures.

In Fig. 5-4, we present the normalized TTG signal with amplitude grating at room temperature and find a weak grating period length dependence. We do not find any grating dependence of the thermal conductivity. Moreover, the thermal conductivity shows a very weak dependence on the crystal orientation, suggesting

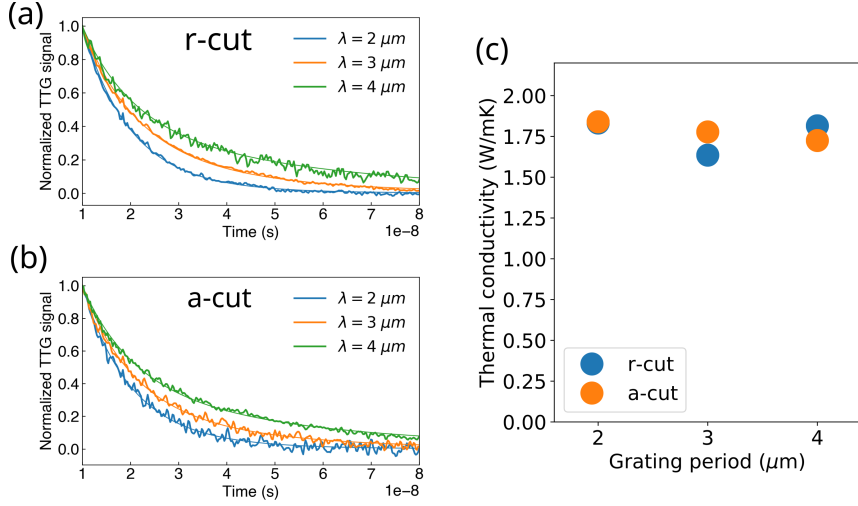


Figure 5-4: TTG signal for V_2O_3 grown on (a) r-cut sapphire and (b) a-cut sapphire and (c) the corresponding fitted thermal conductivity.

that the electronic contribution is small, and the phonon heat conduction does not have strong orientation dependence.

We further vary the temperature and find that near the phase transition temperature, the signal shows strong non-thermal feature. This is because the thermal grating causes the phase transition in the hotter regions first. The boundaries between metal and insulator phases propagate horizontally, which is a much slower process compared with heat conduction. The phase transition changed the band structures as well as the optical reflectivity, thus contributing to the time-dependent signals. However, it is not a trivial task to extract the thermal conductivity, as the heat from the pump are dissipated via two types of processes, the latent heat for phase transition and the lateral heat conduction. Outside the phase transition window, the non-thermal feature in TTG signal disappears.

In Fig. 5-6, we show the thermal conductivity as a function of temperature for the two samples. We drop those TTG datasets that show strong non-thermal features due to insulator-metal transition. The thermal conductivity of two samples are similar, thus we conclude that the thermal conductivity in V_2O_3 does not have a noticeable orientation dependence above the phase transition temperature.

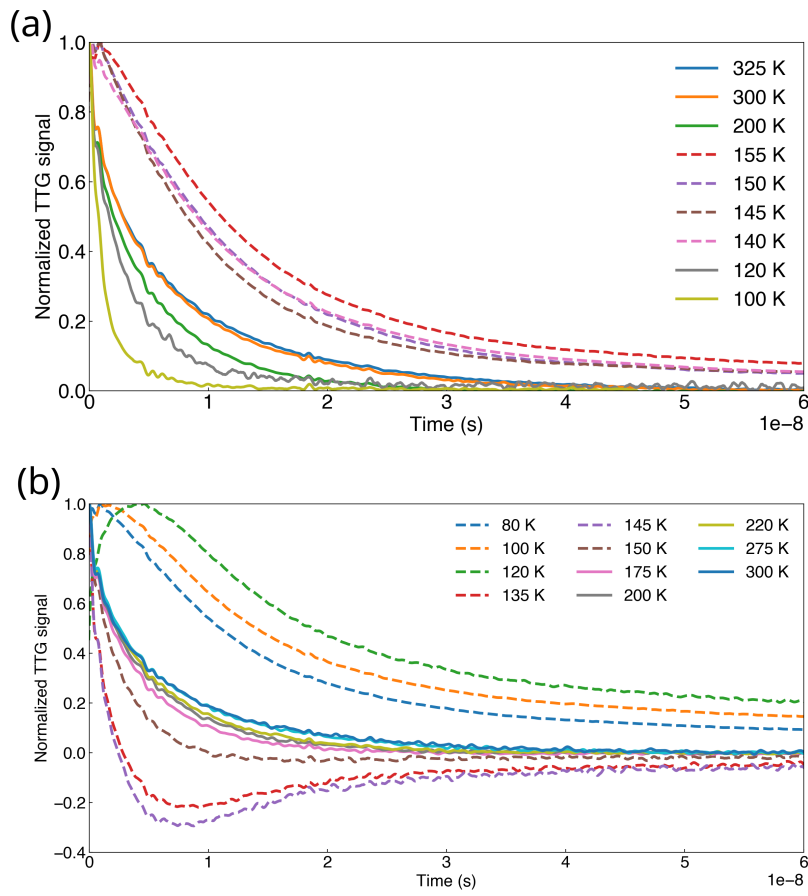


Figure 5-5: TTG signal for V_2O_3 grown on (a) r-cut and (b) a-cut sapphires at various temperatures. The grating period is $2 \mu\text{m}$.

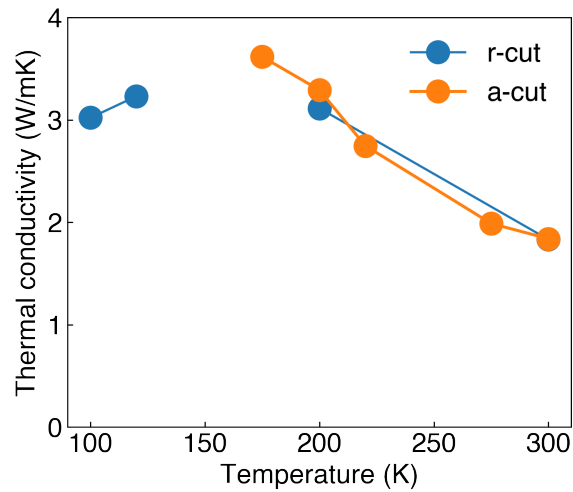


Figure 5-6: Thermal conductivity of V_2O_3 grown on (a) r-cut sapphire and (b) a-cut sapphire at various temperatures.

5.3.2 Thermal conductivity in digital-alloy superlattices

The GaAs/AlAs superlattice has been used in vertical cavity laser and digital-alloy has been often used to tune the electrical resistance of the superlattice. ErAs nanodots can be added at interfaces in superlattice to reduce the thermal conductivity and make GaAs/AlAs superlattice a potential candidate for high-performance thermoelectric materials. We are interested in finding out how the alloying and random dots affect the thermal conduction. The GaAs/AlAs digital-alloy superlattices are provided by Kedong Zhang and Professor Hong Lu. The period for the $\text{Ga}_{0.9}\text{Al}_{0.1}\text{As}/\text{Ga}_{0.1}\text{Al}_{0.9}\text{As}$ superlattice is $3\times[\text{GaAs } (0.9 \text{ nm}) \text{ AlAs } (0.1 \text{ nm})] \ 3\times[\text{GaAs } (0.1 \text{ nm}) \text{ AlAs } (0.9 \text{ nm})]$ and each layer in such structure is known as digital alloy. The digital alloy can strongly scatter high-frequency phonons via alloy scattering. ErAs random dots are introduced to further scatter middle to low frequency phonons. In this case, we want to understand how these strategies impact the thermal conductivity.

We find that directly measuring the superlattice sample without coating a metal transducer is difficult because the GaAs/AlAs superlattice without dots shows strong electronic (non-thermal) responses that cannot be explained by thermal modeling. Thus, we coat a layer of Au with thickness of 95 nm. The interface conductance between the superlattice and the GaAs substrates is taken to be $G_2 = 10^9 \text{ W/m}^2\text{-K}$. The penetration depth for gold transducer layer is taken as 10 nm. The thickness for undoped superlattice and superlattices doped with 4 ml (monolayers) and 8 ml of ErAs are 1120 nm, 1144 nm and 1176 nm, respectively.

In the transient thermal grating measurements, we use grating period of $5.59 \mu\text{m}$ and $9.9 \mu\text{m}$ and plot the average of the fitted thermal conductivity. We find that the sensitivity to the interface conductance between the metal transducer and the superlattice film is low, thus we use the FDTR, which has a higher sensitivity for interface conductance in this case, to measure the interface conductance first (shown in Fig. 5-7) and then we plug the conductance in the TTG model to fit for the thermal conductivity.

In Fig. 5-8, we find the fitted thermal conductivity from TTG signal agrees nicely

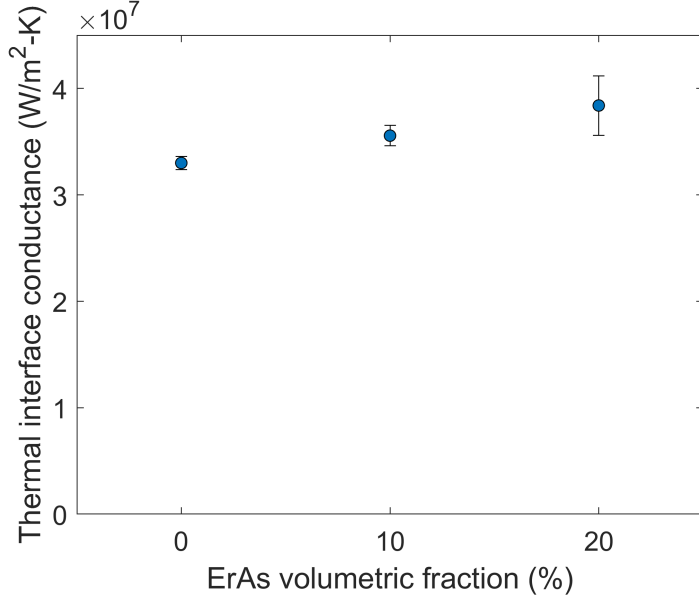


Figure 5-7: Interfacial thermal conductance from FDTR.

with the FDTR results. In addition, the thermal conductivity of GaAs/AlAs superlattice with 10 % quantum dots added is much lower than the superlattice without dots. Meanwhile, adding even more quantum dots does not significantly reduce the thermal conductivity, indicating that the dots cannot induce more phonon scatterings above certain defect concentration.

5.4 Conclusion

In this Chapter, we have presented a way to measure the transport properties of thin-film samples grown on substrates with TTG in the reflection geometry. This method can be used to measure the heat capacity, thermal conductivity and interface resistances in layered medium. We conduct measurements on correlated V₂O₃ thin films and find that orientation has a weak effect on thermal conductivity and the heat conduction is dominated by phonons. We also measure the GaAs/AlAs digital-alloy superlattice with random quantum dots at interfaces and find that the dots induce very strong phonon scattering and drastically reduce the thermal conductivity, yet when the dot concentration is very high, such reduction in thermal conductivity

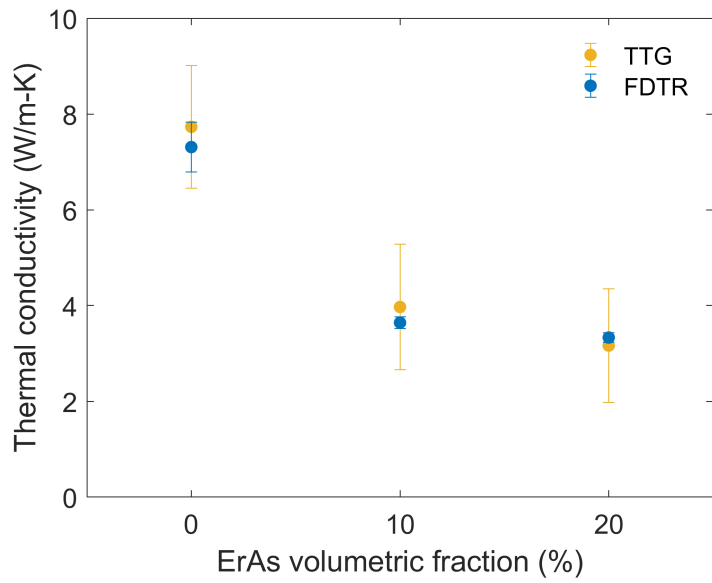


Figure 5-8: Thermal conductivity of GaAs/AlAs digital-alloy superlattices with different ErAs fractions.

saturates.

Chapter 6

Summary and outlook

6.1 Summary

Understanding the phonon and electron transport across interfaces and through disordered structures is crucial to the design of next-generation electronics. The analysis of the interface scattering for electron and phonon from the wave perspective provides new strategies of using interface disorders to enhance the interfacial transport. Furthermore, we experimentally demonstrate that the phonon Anderson localization exists in aperiodic layered medium, which suggests that the phonon wave interferences in disordered structures can be harnessed to control the phonon flow. This thesis provides several new practical strategies to engineer electron and phonon transport using disorders.

In Chapter 2, we present the mode-resolved Green's function formalism to study the electron transmission across interfaces. We find two important factors that contribute to the transmission: the symmetry and the interface roughness. We find that the energy and momentum conservation are not the sufficient condition for electron transmission; the symmetries of the Bloch wavefunctions have to be compatible. The interface roughness can scatter electrons with small wavelengths and create more preferable transmission channels than unwanted reflection channels, resulting in a drastic reduction in contact resistance.

In Chapter 3, we apply the electron Green's function formalism to study phonon

transport across rough interfaces, which has been conventionally studied using the diffuse mismatch model. The diffuse mismatch model assumes that phonon loses its memory of origin after diffuse phonon scattering by interfaces. We clarify that such assumption is invalid. Instead, the phonon partially remains its memory of origin.

In Chapter 4, we study the phonon Anderson localization in aperiodic system and answer three important questions. First, we show how the localization length depends on disorders and material properties. Second, we use theoretical calculation to design aperiodic superlattice structures that supports Anderson localization. Third, we experimentally verify our predictions using optical measurements and find that the phonon Anderson localization exists in aperiodic superlattices up to 200 K.

In Chapter 5, we present a new method based on transient thermal grating to study the in-plane transport of nanoscale thin films grown on substrate without the need to coat the metal transducer layer.

6.2 Outlook

In this section, we first give high-level outlooks on important questions that are yet to solve and then provide several detailed viable research directions. Firstly, the interfacial transport for electron and phonon in this thesis assumes elastic scattering. It remains unclear how inelastic effect changes the interface scattering. For example, for electron transport across interfaces, the electron-phonon scattering can cause Joule heating, which is harmful to transport. However, the electron-phonon scattering can also assist the tunneling. Therefore, it needs further study on the inelastic processes on interfacial transport. Secondly, the interplay between Anderson localization and anharmonicity can play an important role in disordered structures. The physical picture of how anharmonicity destroys phonon interferences is entirely unknown. What's more, experimentally demonstrating phonon Anderson localization in two-dimensional[152] is worth pursuing.

Specifically, for electron transport across interfaces, the impact of band bending needs to be considered by solving the Poisson's equation. In addition, the electron-

phonon interaction can be added via adding the electron-phonon self-energies. The heating and cooling due to energy exchange between electron and lattice (electron-phonon interaction) is relevant to find where the Joule heating and Peltier cooling are happening[153], which helps to optimize the heat generation in electronics.

For phonon transport across rough interfaces, we have presented a continuum model that includes the specular scattering and diffuse scattering while prior modeling has to describe specular scattering and diffuse scattering using different models and combine them with a phenomenological weighting parameter. However, our model is scalar, and it would be useful to derive the vector model that considers the polarization of acoustic phonons[31].

For phonon Anderson localization, we want to point out that there is no general way to compute the phonon localization length. People often uses participation ratio to describe localization, but it has no spatial information. In Chapter 4, we analyze the transmission amplitude decaying along one direction, yet for three-dimensional transport, such one-dimensional analysis is not enough. We think that it is possible to extract the localization length by solving the similar Bloch eigenvalue problem in Chapter 3. In the system where phonon localization emerges, the wavevector \mathbf{q} is complex and the $1/|\text{Im}\{\mathbf{q}\}|$ is the localization length. We can further conduct an ensemble average and identify the intrinsic localized state (gapped state), weakly localized states and strongly localized states due to disorders. Such methodology is applicable to systems in any dimensions.

Appendix A

Green's function for electron transmission

A.1 Mode-resolved Green's function formalism for electron transport

The mode-resolved Green's function formalism to compute the transmission and reflection probability matrix is developed by Khomyakov *et al.*. We present a brief introduction to the formalism as follows for completeness. We first construct the Hamiltonian for the structure shown in Fig. 2-1 (a). For a given $\mathbf{k}_{\text{sc},\parallel}$, the Hamiltonian writes,

$$H(\mathbf{k}_{\text{sc},\parallel}) = \begin{pmatrix} \ddots & & & \\ H_{11}^L & H_{01}^L & & \\ H_{10}^L & H_{00}^L & H_{LD} & \\ & H_{DL} & H_D & H_{DR} \\ & & H_{RD} & H_{00}^R & H_{01}^R \\ & & & H_{10}^R & H_{11}^R \\ & & & & \ddots \end{pmatrix} \quad (\text{A.1})$$

with the matrix blocks corresponding to different cells of the supercell along the interface normal as well as the interactions between neighboring cells. In the semi-infinite

lead region, we have $H_{nn}^L = H_{00}^L$ and $H_{nn}^R = H_{00}^R$, where n denote the n th repeated supercell cell in the lead region as denoted in Fig. 1 (a). H_D is the Hamiltonian corresponding to the device region. $H_{LD/DL}$ and $H_{RD/DR}$ describe interactions between the lead and the device region.

The Green's function matrix is defined by,

$$((E \pm i\eta)I - H(\mathbf{k}_{sc,\parallel}))G^{r/a}(E, \mathbf{k}_{sc,\parallel}) = I \quad (\text{A.2})$$

where I is the identity matrix, η is an infinitesimal positive real number and the superscripts r and a denote retarded and advanced Green's function, depending on the sign in front of $i\eta$. The retarded Green's function at given energy E in the block matrix form is explicitly expressed by,

$$G^r(E, \mathbf{k}_{sc,\parallel}) = \begin{pmatrix} \ddots & & & & \\ & G_{11}^L & G_{01}^L & & \ddots \\ & G_{10}^L & G_{00}^L & G_{LD} & G_{0,N+1} \\ & & G_{DL} & G_D & G_{DR} \\ & & G_{N+1,0} & G_{RD} & G_{00}^R & G_{01}^R \\ & \ddots & & & G_{10}^R & G_{11}^R \\ & & & & & \ddots \end{pmatrix} \quad (\text{A.3})$$

In particular, the matrix block G_{00}^L and G_{00}^R are useful physical quantities to compute the transmission matrix, called the surface Green's function for the left and right lead which satisfies,

$$g_{L/R}^r(E, \mathbf{k}_{sc,\parallel}) = G_{00}^{L/R} = [(E + i\eta)I - H_{00}^{L/R} - \Sigma_{L/R}^r]^{-1} \quad (\text{A.4})$$

where the self-energy of left and right lead are $\Sigma_L^r = H_{10}^L g_L^r H_{01}^L$ and $\Sigma_R^r = H_{01}^R g_R^r H_{10}^R$. In this work, the surface Green's functions are iteratively solved using the decimation technique[115].

The matrix block $G_{N+1,0}$ describes the response at $N + 1$ th cell (0 th cell in the

right lead) cell given the perturbation at 0 th cell in the left lead. We use Dyson's equation to compute the matrix $G_{N+1,0}$. To obtain $G_{N+1,0}$, we need to evaluate the matrix block G_D for the device region, which contains a large amount of atoms for the case of rough interfaces. The efficient computation for device Green's function G_D is thus challenging. To overcome this difficulty, the device Green's function is calculated using the recursive technique[116, 117] and the detail for our implementation of the recursive Green's function can be found in our prior work[76].

To compute the transmission mentioned in Eq. 2.4, we need to compute the eigenvector matrices and velocity matrices. We outline how to compute these matrices in the following. For a given transverse momentum $\mathbf{k}_{\text{sc},\parallel}$ and energy E , there are multiple subbands in the lead region with different perpendicular momenta k_z 's. What's more, the lead is semi-infinite, which supports both propagating (real k_z) and evanescent (imaginary k_z) states. We need to resolve the perpendicular momentum k_z and its corresponding velocity v_z to compute the ratio of scattered current to the incident current to obtain the transmission and reflection probability matrix.

We first introduce an auxiliary matrix for the right lead,

$$F_R^r = g_R^r H_{10}^R \quad (\text{A.5})$$

and compute its eigenvalue Λ_R^r and eigenvector U_R^r via,

$$F_R^r U_R^r = \Lambda_R^r U_R^r \quad (\text{A.6})$$

It has been pointed by Khomyakov *et al.*[75] that the eigenvalue $\Lambda_{R,i}^r$ stores the phase information of the electron and the eigenvector matrix $U_{R,i}^r$ contains the Bloch wavefunctions for state i . If $|\Lambda_{R,i}^r| \neq 1$, it corresponds to an evanescent state. If $|\Lambda_{R,i}^r| = 1$, it corresponds to a propagating state. We can extract the perpendicular momentum by $k_{R,i} = \frac{1}{a_R} \log \Lambda_{R,i}^r$. Similarly, for the left lead, we define the auxiliary

matrix, its eigenvalues and eigenvectors,

$$\begin{aligned} F_L^a &= g_L^a H_{01}^L \\ F_L^a U_L^a &= \Lambda_L^a U_L^a \end{aligned} \tag{A.7}$$

where $g_L^a = (g_L^r)^\dagger$ is the advanced surface Green's function for the left lead.

The velocity along the transport direction (perpendicular to interface) v_z can be described by the velocity matrix,

$$\begin{aligned} V_L^a &= -U_L^{a\dagger} \Gamma_L^a U_L^a, \\ V_R^r &= U_R^{r\dagger} \Gamma_R^r U_R^r. \end{aligned} \tag{A.8}$$

where $\Gamma = i(\Sigma - \Sigma^\dagger)$. The diagonal elements of these matrices correspond to the group velocities along z direction of different states.

The reflection probability matrix from α side $R_{\alpha\alpha,ji}(E, \mathbf{k}_{\text{sc},\parallel})$ is similarly defined by,

$$R_{\alpha\alpha,ji}(E, \mathbf{k}_{\text{sc},\parallel}) = |r_{\alpha\alpha,ji}(E, \mathbf{k}_{\text{sc},\parallel})|^2 \tag{A.9}$$

Specifically, the reflection matrices from the left and right side are,

$$\begin{aligned} r_{LL}(E, \mathbf{k}_{\text{sc},\parallel}) &= i\sqrt{V_L^r} [U_L^r]^{-1} (G_{0,0} - Q_L^{-1}) [U_L^{a\dagger}]^{-1} \sqrt{V_L^a} \\ r_{RR}(E, \mathbf{k}_{\text{sc},\parallel}) &= i\sqrt{V_R^r} [U_R^r]^{-1} (G_{N+1,N+1} - Q_R^{-1}) [U_R^{a\dagger}]^{-1} \sqrt{V_R^a} \end{aligned} \tag{A.10}$$

where $Q_L^{-1} = (E + i\eta)I - H_{00}^L - H_{10}^L g_L^r H_{01}^L - H_{01}^L g_L^r H_{10}^L$ and $Q_R^{-1} = (E + i\eta)I - H_{00}^R - H_{01}^R g_R^r H_{10}^R - H_{10}^R g_R^r H_{01}^R$ are the retarded Green's functions for bulk materials. g_α^r , $\alpha = L, R$ are the retarded surface Green's function similar to Eq. A.4, except that they describe the semi-infinite lead of the same material extending to infinity in the opposite direction, and they are given by,

$$\begin{aligned} g_{L'}^r(E, \mathbf{k}_{\text{sc},\parallel}) &= [(E + i\eta)I - H_{00}^L - \Sigma_{L'}^r]^{-1} \\ g_{R'}^r(E, \mathbf{k}_{\text{sc},\parallel}) &= [(E + i\eta)I - H_{00}^R - \Sigma_{R'}^r]^{-1} \end{aligned} \tag{A.11}$$

where the self-energies write,

$$\begin{aligned}\Sigma_{L'}^r &= H_{01}^L g_{L'}^r H_{10}^L \\ \Sigma_{R'}^r &= H_{10}^R g_{R'}^r H_{01}^R\end{aligned}\tag{A.12}$$

The reflection matrix also depends on another two surface Green's function g_L^r and g_R^a , as defined by Eq. A.4. The auxiliary matrices, eigenvalue matrices and eigenvector matrices for these two surface Green's functions are,

$$\begin{aligned}F_L^r &= g_L^r H_{01}^L \\ F_L^r U_L^r &= \Lambda_L^r U_L^r\end{aligned}\tag{A.13}$$

$$\begin{aligned}F_R^a &= g_R^a H_{10}^R \\ F_R^a U_R^a &= \Lambda_R^a U_R^a\end{aligned}\tag{A.14}$$

The self-energies for these two surface Green's functions are,

$$\begin{aligned}\Sigma_R^a &= H_{01}^R g_R^a H_{10}^R \\ \Sigma_L^r &= H_{10}^L g_L^r H_{01}^L\end{aligned}\tag{A.15}$$

The corresponding broadening matrices are computed by $\Gamma = i(\Sigma - \Sigma^\dagger)$. The velocity matrices V_R^a and V_L^r introduced in Eq. A.10 are expressed by,

$$\begin{aligned}V_R^a &= -U_R^{a\dagger} \Gamma_R^a U_R^a, \\ V_L^r &= U_L^{r\dagger} \Gamma_L^r U_L^r.\end{aligned}\tag{A.16}$$

A.2 Interface atomic mixing

In Fig. A-1, we present the ensemble-averaged atomic number density along z direction for different ml and transverse supercell sizes. In Fig. A-2, we demonstrate the corresponding electron transmission for different interface configurations. At fixed ml number, smaller transverse supercell sizes give rise to higher nonspecular transmission function. At fixed transverse supercell size, the higher ml numbers give rise to higher

nonspecular transmission function.

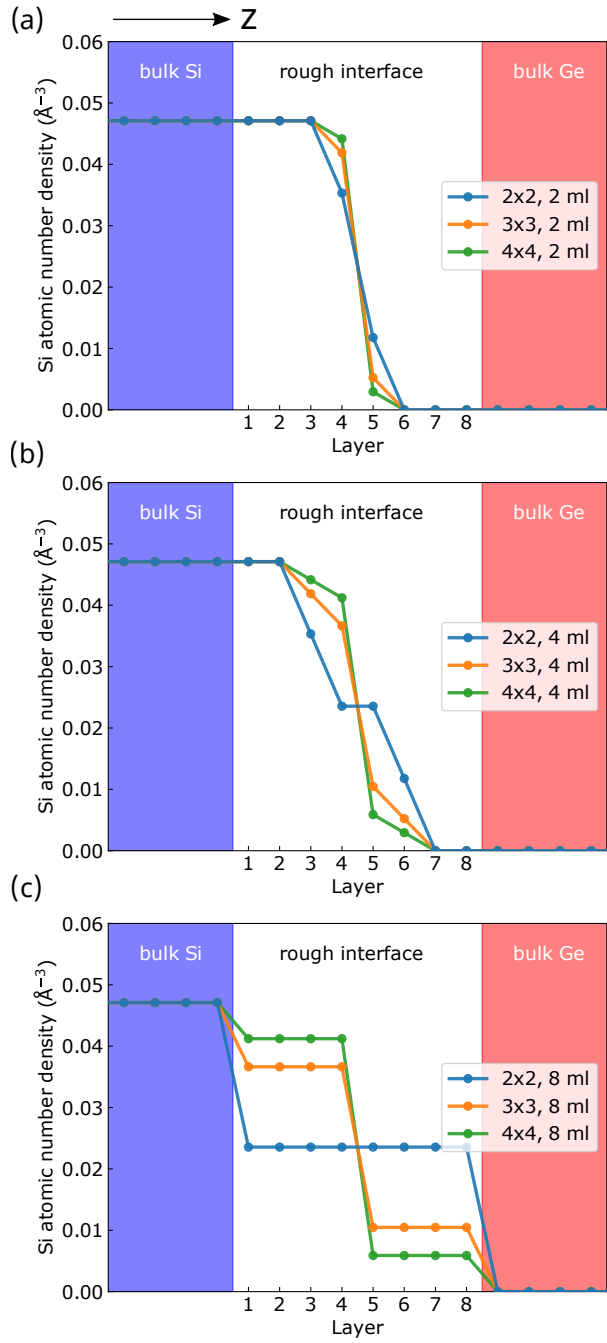


Figure A-1: The atomic number density (the number of atoms of a given type per unit volume) of Si at different atom layers of the interface.

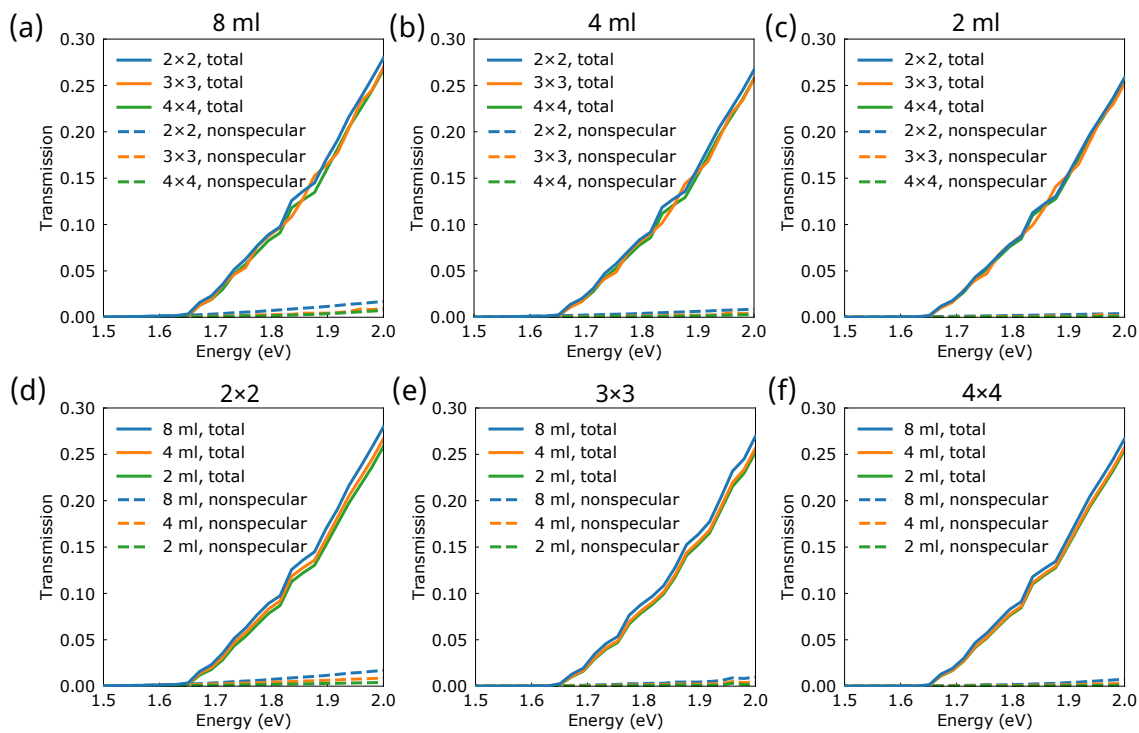


Figure A-2: The sensitivity of electron transmission on the degree of transverse and longitudinal disorders. We use 20×20 , 15×15 , 10×10 $\mathbf{k}_{sc,\parallel}$ -point mesh for 2×2 , 3×3 , 4×4 transverse supercells.

Appendix B

The continuum modeling of diffuse phonon scattering

B.1 Formalism

B.1.1 The transmission and reflection matrix

We consider interfacial transport in the case of scalar phonon model in the continuum limit, where the equation of motion (EOM) for displacements writes[154],

$$\rho(\mathbf{r}) \frac{\partial^2 u}{\partial t^2} - \nabla \cdot (\mu(z) \nabla u) = 0 \quad (\text{B.1})$$

where $\mu(z)$ is the bulk modulus. For an interface between two dissimilar solids, we have $\mu(z) = \mu_L$ for $z < 0$ and $\mu(z) = \mu_R$ for $z \geq 0$. $\rho(\mathbf{r}) = \rho_0(z) + \Delta\rho(\mathbf{r})$ is the density, where $\rho_0(z)$ is the density without mass disorder at the interface, expressed by $\rho_0(z < 0) = \rho_L$ and $\rho_0(z > 0) = \rho_R$. $\Delta\rho(\mathbf{r}) = \sum_i \Delta m_i \delta(\mathbf{r}_{\parallel} - \mathbf{r}_{i,\parallel}) \delta(z)$ is the density fluctuations due to atomic mixing at the interface, where Δm_i is the change of mass at atom site i and $\mathbf{r}_{i,\parallel}$ is the in-plane position of atom site i . The choice of the delta function form for density fluctuations suggests that the atomic mixing only exists exactly at the interface, thus our model does not apply to the cases where the atomic mixing exists even far away from the interface. When atomic mixing is realized by

randomly swapping pairs of atoms on two sides of the interface, the average of mass fluctuations is zero $\sum_i \Delta m_i = 0$. The mass disorders are distributed randomly in the x-y plane. The ensemble average of any physical quantity P over many configurations of mass disorders is obtained by integrating over all possible positions of mass disorders,

$$\langle P \rangle = \int \prod_j \frac{d^2 \mathbf{r}_{\parallel,j}}{A} P \quad (\text{B.2})$$

where A is the cross-section area. After ensemble average, the average of mass fluctuations is still zero $\langle \sum_i \Delta m_i = 0 \rangle$. We further assume an independent distribution of mass fluctuations such that,

$$\langle \sum_{i,j} \Delta m_i \Delta m_j \rangle = \sum_i \langle (\Delta m_i)^2 \rangle \quad (\text{B.3})$$

The time-harmonic solution of Eq. B.1 reads,

$$u = \sum_{\mathbf{q}_{\parallel}} u_{\mathbf{q}_{\parallel}}(z) \frac{e^{i(-\omega t + \mathbf{q}_{\parallel} \cdot \mathbf{r}_{\parallel})}}{\sqrt{A}} \quad (\text{B.4})$$

where $\mathbf{q}_{\parallel} = (q_x, q_y)$ is the transverse wavevector, ω is the phonon frequency, $\mathbf{r}_{\parallel} = (x, y)$ is the transverse position and $u_{\mathbf{q}_{\parallel}}(z)$ is the z-dependent component of the solution. The perpendicular wavevectors $q_{\perp}(z) = q_{z,L}$, when $z < 0$, and $q_{\perp}(z) = q_{z,R}$, when $z \geq 0$, are determined by the dispersion relation $\omega^2 = c_{L/R}^2 (q_{\parallel}^2 + q_{\perp,L/R}^2)$. Here, $c_{L/R}$ is the sound velocity defined by $c_{L/R} = \sqrt{\mu_{L/R}/\rho_{L/R}}$. Plugging in the time-harmonic solution to EOM, we have the following equation for $u_{\mathbf{q}_{\parallel}}(z)$,

$$\sum_{\mathbf{q}_{\parallel}} \left[(\rho_0(z) + \Delta\rho(\mathbf{r})) \omega^2 + \nabla \cdot \mu(z) \nabla \right] u_{\mathbf{q}_{\parallel}}(z) \frac{e^{i\mathbf{q}_{\parallel} \cdot \mathbf{r}_{\parallel}}}{\sqrt{A}} = 0 \quad (\text{B.5})$$

Multiply both sides of Eq. B.5 by $\int d^2 \mathbf{r}_{\parallel} e^{-i\mathbf{q}'_{\parallel} \cdot \mathbf{r}_{\parallel}} / \sqrt{A}$. The orthogonality relations for plane waves leads to,

$$\left[\mu(z) q_{\perp}^2(z) + \frac{\partial}{\partial z} \mu(z) \frac{\partial}{\partial z} \right] u_{\mathbf{q}'_{\parallel}} = \sum_{\mathbf{q}_{\parallel}} M_{\mathbf{q}'_{\parallel}, \mathbf{q}_{\parallel}} \delta(z) u_{\mathbf{q}_{\parallel}} \quad (\text{B.6})$$

The scattering matrix $M_{\mathbf{q}'_\parallel, \mathbf{q}_\parallel}$ is defined by,

$$M_{\mathbf{q}'_\parallel, \mathbf{q}_\parallel} = - \sum_i \Delta m_i \omega^2 A^{-1} e^{i(\mathbf{q}_\parallel - \mathbf{q}'_\parallel) \cdot \mathbf{r}_{\parallel, i}}. \quad (\text{B.7})$$

The solution to Eq. B.6 is expressed by,

$$\begin{aligned} u_{\mathbf{q}_\parallel}(z) &= \delta_{\mathbf{q}_\parallel, \mathbf{q}'_\parallel} e^{iq_L z} + r_{\mathbf{q}_\parallel, \mathbf{q}'_\parallel} \frac{\sqrt{v'_L}}{\sqrt{v_L}} e^{-iq_L z}, \quad z \leq 0 \\ u_{\mathbf{q}_\parallel}(z) &= t_{\mathbf{q}_\parallel, \mathbf{q}'_\parallel} \frac{\sqrt{\rho_L v'_L}}{\sqrt{\rho_R v_R}} e^{iq_R z}, \quad z \geq 0 \end{aligned} \quad (\text{B.8})$$

where $q_{L/R} = q_{z,L/R}$ is the phonon wavevector normal to the interface. $t_{\mathbf{q}_\parallel, \mathbf{q}'_\parallel}$ is the transmission matrix and $r_{\mathbf{q}_\parallel, \mathbf{q}'_\parallel}$ is the reflection matrix. $v_{L/R} = c_{L/R} \cos \theta_{L/R}$ is the group velocity perpendicular to the interface, where $\theta_{L/R}$ is the angle between the direction of phonon velocity and the axis normal to the interface.

The transmission and reflection probability matrix are defined by the ratio of the transmitted flux normal to the interface of phonon \mathbf{q}_\parallel and the reflected flux normal to the interface of phonon \mathbf{q}_\parallel to the incident flux normal to the interface of phonon state \mathbf{q}'_\parallel , $T_{\mathbf{q}_\parallel, \mathbf{q}'_\parallel} = \frac{J_{t, \mathbf{q}_\parallel}}{J_{\text{inc}, \mathbf{q}'_\parallel}}$ and $R_{\mathbf{q}_\parallel, \mathbf{q}'_\parallel} = \frac{J_{r, \mathbf{q}_\parallel}}{J_{\text{inc}, \mathbf{q}'_\parallel}}$, respectively, where the time-averaged energy flux for a phonon mode reads[155],

$$J = \frac{\mu(z)}{-i\omega A} \int \left(u^* \frac{\partial u}{\partial z} - u \frac{\partial u^*}{\partial z} \right) d^2 \mathbf{r}_\parallel \quad (\text{B.9})$$

The resultant expressions for transmission probability matrix and reflection probability matrix are,

$$T_{\mathbf{q}_\parallel, \mathbf{q}'_\parallel} = \left| t_{\mathbf{q}_\parallel, \mathbf{q}'_\parallel} \right|^2 \quad (\text{B.10a})$$

$$R_{\mathbf{q}_\parallel, \mathbf{q}'_\parallel} = \left| r_{\mathbf{q}_\parallel, \mathbf{q}'_\parallel} \right|^2 \quad (\text{B.10b})$$

The boundary conditions for displacement $u_{\mathbf{q}_\parallel}(z)$ for solving the transmission and reflection matrix write,

$$u_{\mathbf{q}_\parallel}(0^-) = u_{\mathbf{q}_\parallel}(0^+) \quad (\text{B.11a})$$

$$\mu(z) \frac{\partial}{\partial z} u_{\mathbf{q}_{\parallel}}(z) \Big|_{0^-}^{0^+} = \sum_{\mathbf{q}_{\parallel}''} M_{\mathbf{q}_{\parallel}, \mathbf{q}_{\parallel}''} u_{\mathbf{q}_{\parallel}''}(0), \quad (\text{B.11b})$$

where the second boundary condition is obtained by integrating Eq. B.6 from $-\eta$ to η , with $\eta \rightarrow 0^+$. Plug in the expression in Eq. B.8 into the boundary condition. We obtain the following expressions,

$$\delta_{\mathbf{q}_{\parallel}, \mathbf{q}'_{\parallel}} + r_{\mathbf{q}_{\parallel}, \mathbf{q}'_{\parallel}} = t_{\mathbf{q}_{\parallel}, \mathbf{q}'_{\parallel}} \quad (\text{B.12a})$$

$$\sum_{\mathbf{q}_{\parallel}''} (\delta_{\mathbf{q}_{\parallel}, \mathbf{q}_{\parallel}''} + i\Gamma_{\mathbf{q}_{\parallel}, \mathbf{q}_{\parallel}''}) t_{\mathbf{q}_{\parallel}''} = \Lambda_{\mathbf{q}_{\parallel}, \mathbf{q}'_{\parallel}} \quad (\text{B.12b})$$

where

$$\Gamma_{\mathbf{q}_{\parallel}, \mathbf{q}_{\parallel}''} = \frac{M_{\mathbf{q}_{\parallel}, \mathbf{q}_{\parallel}''}}{2\omega\bar{\rho}\bar{v}} \sqrt{\frac{v_R}{v_R''}} \quad (\text{B.13a})$$

$$\Lambda_{\mathbf{q}_{\parallel}, \mathbf{q}'_{\parallel}} = \delta_{\mathbf{q}_{\parallel}, \mathbf{q}'_{\parallel}} \frac{\sqrt{v_L v_R}}{\bar{v}} \quad (\text{B.13b})$$

$$\bar{v} = \frac{\rho_L v_L + \rho_R v_R}{2\bar{\rho}} \quad (\text{B.13c})$$

$$\bar{\rho} = \sqrt{\rho_L \rho_R} \quad (\text{B.13d})$$

In particular, we can reorganize Eq. B.12b and identify that the transmission matrix can be expanded in series as,

$$t = \sum_{N=0}^{\infty} (-i\Gamma)^N \Lambda. \quad (\text{B.14})$$

which is a summation of terms arising from multiple scatterings of different orders. We can discard high-order terms to obtain the approximate expression for the transmission matrix.

B.1.2 The Green's function in the continuum limit

The transmission matrix can be computed from the Green's function of the whole system. We choose to compute the Green's function because of the mathematical convenience in perturbation expansions using Dyson's equation. In the following, we will illustrate the exact relationship between the transmission matrix and the Green's function.

To start with, we evaluate the unperturbed Green's function for a disorder-free interface. The unperturbed EOM writes,

$$\left[\rho_0(z) \omega^2 + \frac{\partial}{\partial z} \mu(z) \frac{\partial}{\partial z} \right] u(z) = 0 \quad (\text{B.15})$$

which can be identified as a Sturm-Liouville equation. Two sets of solutions are given by,

$$u_<(z) = \begin{cases} t_L e^{-iq_L z}, & z < 0 \\ e^{-iq_R z} + r_L e^{iq_R z}, & z > 0 \end{cases} \quad (\text{B.16})$$

and

$$u_>(z) = \begin{cases} t_R e^{iq_R z}, & z > 0 \\ e^{iq_L z} + r_R e^{-iq_L z}, & z < 0 \end{cases} \quad (\text{B.17})$$

The continuity condition at interface gives,

$$t_L = 1 + r_L = \frac{2\mu_R q_R}{\mu_L q_L + \mu_R q_R} \quad (\text{B.18})$$

and

$$t_R = 1 + r_R = \frac{2\mu_L q_L}{\mu_L q_L + \mu_R q_R} \quad (\text{B.19})$$

For a Sturm-Liouville equation, the Wronskian writes[156],

$$W = u_<(z) \frac{du_>(z)}{z} - u_>(z) \frac{du_<(z)}{z}$$

$$= \begin{cases} \frac{4i\mu_L q_L q_R}{\mu_L q_L + \mu_R q_R}, & z > 0 \\ \frac{4i\mu_R q_L q_R}{\mu_L q_L + \mu_R q_R}, & z < 0 \end{cases} \quad (\text{B.20})$$

and the Green's function is defined by,

$$G_0(z, z') = \begin{cases} \frac{u_{<}(z)u_{>}(z')}{\mu(z')W(z')}, & -\infty < z < z' \\ \frac{u_{<}(z')u_{>}(z)}{\mu(z')W(z')}, & z' < z < \infty \end{cases}$$

$$= \begin{cases} -\frac{i}{2\mu_L} \frac{t_R}{q_L} e^{-iq_L z} e^{iq_R z'}, & z < 0, z' > 0 \\ -\frac{i}{2\mu_R} \frac{t_L}{q_R} e^{-iq_L z'} e^{iq_R z}, & z > 0, z' < 0 \\ -\frac{i}{2\mu_L} \frac{e^{-iq_L|z'-z|} + r_R e^{-iq_L(z+z')}}{q_L}, & z < 0, z' < 0 \\ -\frac{i}{2\mu_R} \frac{e^{iq_R|z'-z|} + r_L e^{iq_R(z+z')}}{q_R}, & z > 0, z' > 0 \end{cases} \quad (\text{B.21})$$

When z and z' both approaches zero, the unperturbed Green's function at interface is

$$G_0^+ = -\frac{i}{\mu_L q_L + \mu_R q_R} = -\frac{i}{2\omega \bar{\rho} \bar{v}} \quad (\text{B.22})$$

where the superscript $+$ is added to represents the retarded Green's function.

Then, we study the Green's function for the scenario where atomic mixing is present at the interface. It is convenient to define the Green's function operator,

$$\hat{G}^\pm = [\rho(\mathbf{r})\omega^2 - \hat{K} \pm i\eta]^{-1} \quad (\text{B.23})$$

where the operator $\hat{K} = -\nabla \cdot \mu(z)\nabla$ and η is an infinitesimal positive real number. The Green's function in the real space representation can then be expressed by $G^\pm(\mathbf{r}, \mathbf{r}') = \langle \mathbf{r} | \hat{G}^\pm | \mathbf{r}' \rangle$. The Green's function that describes the scattering channel between mode a of left side and mode b of right side is,

$$G_{b,a}^\pm(z, z') = A^{-1} \iint d\mathbf{r}_\parallel d\mathbf{r}'_\parallel e^{-i(\mathbf{q}_\parallel \cdot \mathbf{r}_\parallel - \mathbf{q}'_\parallel \cdot \mathbf{r}'_\parallel)} \times \langle u_{\mathbf{q}_\parallel} | \hat{G}^\pm | u'_{\mathbf{q}'_\parallel} \rangle \quad (\text{B.24})$$

where the transverse wavevector for mode a and mode b are \mathbf{q}'_\parallel and \mathbf{q}_\parallel , respectively.

When disorders are introduced, the perturbed eigenvector is related to the unper-

turbed eigenvector via[157],

$$u = u' + \int G^+(\mathbf{r}, \mathbf{r}') V(\mathbf{r}') u'(\mathbf{r}') d\mathbf{r}', \quad (\text{B.25})$$

where u' is the eigenstate for the disorder-free case and the perturbation $V(\mathbf{r}) = -\Delta\rho(\mathbf{r})\omega^2$. Specifically, the second term on the right-hand side of Eq. B.25 equals,

$$\begin{aligned} & \int d\mathbf{r}' G^+(\mathbf{r}, \mathbf{r}') V(\mathbf{r}') u'(\mathbf{r}') \\ &= \int d\mathbf{r}' \left\{ G^+(\mathbf{r}, \mathbf{r}') \hat{K}' - \delta(\mathbf{r} - \mathbf{r}') - [\hat{K}' G^+(\mathbf{r}, \mathbf{r}')] \right\} u'(\mathbf{r}') \end{aligned} \quad (\text{B.26})$$

Thus, Eq. B.25 is equivalent to,

$$u = \int \mu(\mathbf{r}') \left(u' \frac{\partial G^+}{\partial z'} - G^+ \frac{\partial u'}{\partial z'} \right) \hat{\mathbf{e}}_z \cdot d\mathbf{S}' \quad (\text{B.27})$$

It is easy to show that,

$$\begin{aligned} \langle u' | V | u \rangle_{b,a} &= \langle \hat{K} u' | u \rangle_{b,a} - \langle u' | \hat{K} | u \rangle_{b,a} \\ &= \int [u_a \hat{K} u_b'^* - u_b'^* \hat{K} u_a] d^3\mathbf{r} \\ &= \int \mu(\mathbf{r}) \left[u_b'^* \frac{\partial u_a}{\partial z} - \frac{\partial u_b'^*}{\partial z} u_a \right] \hat{\mathbf{e}}_z \cdot d\mathbf{S} \end{aligned} \quad (\text{B.28})$$

where we applied integration by part and the divergence theorem.

Plugging in the expression of u given by Eq. B.27 into Eq. B.28, we have,

$$\begin{aligned}
\langle u' | V | u \rangle_{b,a} &= \int [\hat{K}u_b'^*(\mathbf{r})] u_a(\mathbf{r}) d\mathbf{r} \\
&\quad - \iint u_b'^*(\mathbf{r}) \mu(\mathbf{r}') \\
&\quad \times \left[u_a'(\mathbf{r}') \frac{\partial \hat{K}G^+}{\partial z'} - \frac{\partial u_a'(\mathbf{r}')}{\partial z'} \hat{K}G^+ \right] dS' d\mathbf{r} \\
&= \iint \mu(\mathbf{r}) \mu(\mathbf{r}') \left\{ \frac{\partial u_b'^*(\mathbf{r})}{\partial z} \right. \\
&\quad \times \left[-u_a'(\mathbf{r}') \frac{\partial G^+}{\partial z'} + G^+ \frac{\partial u_a'(\mathbf{r}')}{\partial z'} \right] \\
&\quad \left. + u_b'^*(\mathbf{r}) \left[u_a'(\mathbf{r}') \frac{\partial^2 G^+}{\partial z \partial z'} - \frac{\partial u_a'(\mathbf{r}')}{\partial z'} \frac{\partial G^+}{\partial z} \right] \right\} dS dS' \\
&= -4\mu_L \mu_R t_{b,R}^* e^{-ik_{b,R}z_2 + ik_{a,L}z'_1} G^+(z_2, z'_1) q_{b,R} q_{a,L} \\
&\quad - 4\mu_L^2 r_{b,R}^* e^{ik_{b,L}z_1 + ik_{a,L}z'_1} G_1^+(z_1, z'_1) q_{b,L} q_{a,L} \\
&\quad + 4\mu_L^2 r_{b,R}^* e^{ik_{b,L}z_1 - ik_{a,L}z'_1} G_2^+(z_1, z'_1) q_{b,L} q_{a,L}
\end{aligned} \tag{B.29}$$

where $G^+(z_1, z'_1) = G_1^+(z_1, z'_1) + G_2^+(z_1, z'_1)$ and we do not need to know the exact expression of G_1^+ and G_2^+ . Note that we have used the form of Green's function in its asymptotic limit in deriving the above expression. Denote L the length of the domain containing disorders. Then, $z_1, z'_1 < 0$ and $z_2, z'_2 > L$ are the boundary for integration. Since the random mass disorders are localized at the interface at $z = 0$, we have $L \rightarrow 0$, such that we can set $z_1 = z'_1 = 0^-$ and $z_2 = z'_2 = 0^+$.

Directly plugging in the general expression of u' for unperturbed system given by Eq. B.17 and u for perturbed system given by Eq. B.8, we can obtain another expression for matrix element $\langle u' | V | u \rangle_{b,a}$,

$$\begin{aligned}
\langle u' | V | u \rangle_{b,a} &= 2i\omega t_{b,R}^* t_{b,a} \sqrt{\rho_L v_{a,L} \rho_R v_{b,R}} \\
&\quad + 2i\omega \left(r_{b,R}^* r_{b,a} \frac{\sqrt{v_{a,L}}}{\sqrt{v_{b,L}}} - \delta_{b,a} \right) \rho_L v_{b,L}
\end{aligned} \tag{B.30}$$

By equating Eq. B.29 to Eq. B.30, we have found the relationship between trans-

mission matrix and Green's function,

$$\begin{aligned} t_{b,a} &= 2i\omega G_{b,a}^+(0^+, 0^-) \sqrt{\rho_L \rho_R v_{a,L} v_{b,R}} \\ &= 2i\omega \bar{\rho} \sqrt{v_R v'_L} G_{\mathbf{q}_{\parallel}, \mathbf{q}'_{\parallel}}^+ \end{aligned} \quad (\text{B.31})$$

Furthermore, using the boundary condition given by Eq. B.12a, we find that the reflection matrix is related to Green's function through,

$$\begin{aligned} r_{b,a} &= 2i\omega G_{b,a}^+(0^-, 0^-) \rho_L \sqrt{v_{a,L} v_{b,L}} - \delta_{ba}. \\ &= 2i\omega \rho_L \sqrt{v_L v'_L} G_{\mathbf{q}_{\parallel}, \mathbf{q}'_{\parallel}}^+ - \delta_{\mathbf{q}_{\parallel}, \mathbf{q}'_{\parallel}} \end{aligned} \quad (\text{B.32})$$

B.1.3 The ensemble averaged Green's function

From the series expansion of the transmission matrix in Eq. B.14 and relationship between transmission matrix and Green's function given by Eq. B.31, we can obtain the following series for the ensemble averaged Green's function,

$$\langle G_{\mathbf{q}_{\parallel}, \mathbf{q}'_{\parallel}}^+ \rangle = -i \frac{1}{2\omega \bar{\rho} v'} \frac{\sqrt{v'_R}}{\sqrt{v_R}} \sum_N \left\langle (-i\Gamma)^N \right\rangle_{\mathbf{q}_{\parallel}, \mathbf{q}'_{\parallel}} \quad (\text{B.33})$$

According to Eq. B.2, the ensemble average of matrix $(-i\Gamma)^N$ is obtained by integrating over all possible impurity positions,

$$\langle (-i\Gamma)^N \rangle = \int \prod_j \frac{d^2 \mathbf{r}_{\parallel,j}}{A} (-i\Gamma)^N \quad (\text{B.34})$$

In the weak perturbation limit, using Eq. B.3, Eq. B.7 and Eq. B.13a, we write down the Green's function in Eq. B.33 up to the second order,

$$\langle G_{\mathbf{q}_{\parallel}, \mathbf{q}'_{\parallel}}^+ \rangle = \left(G_0^+(\mathbf{q}'_{\parallel}) + G_0^{+2}(\mathbf{q}'_{\parallel}) \frac{V_2}{A} \sum_{\mathbf{q}''_{\parallel}} G_0^+(\mathbf{q}''_{\parallel}) \right) \delta_{\mathbf{q}_{\parallel}, \mathbf{q}'_{\parallel}} \quad (\text{B.35})$$

where $V_2 = \langle \sum_i \frac{m_i^2}{A} \omega^4 \rangle$. The first-order term vanishes due to ensemble average $\langle \sum_i m_i \omega^2 \rangle = 0$. The diagonal form of Eq. B.35 implies that the ensemble average recovers the in-

plane translational symmetry of the unperturbed Green's function.

B.1.4 The transmission and reflection probability matrix

From Eq. B.10a, we find that the transmission probability matrix is related to the product of retarded and advanced Green's function,

$$\langle T_{\mathbf{q}_\parallel, \mathbf{q}'_\parallel} \rangle = 4\omega^2 \bar{\rho}^2 v'_L v_R \langle G_{\mathbf{q}_\parallel, \mathbf{q}'_\parallel}^+ G_{\mathbf{q}_\parallel, \mathbf{q}'_\parallel}^- \rangle. \quad (\text{B.36})$$

The ensemble averaged $\langle G_{\mathbf{q}_\parallel, \mathbf{q}'_\parallel}^+ G_{\mathbf{q}_\parallel, \mathbf{q}'_\parallel}^- \rangle$ can be expressed by,

$$\begin{aligned} \langle G_{\mathbf{q}_\parallel, \mathbf{q}'_\parallel}^+ G_{\mathbf{q}_\parallel, \mathbf{q}'_\parallel}^- \rangle &= |\langle G_{\mathbf{q}_\parallel, \mathbf{q}'_\parallel}^+ \rangle|^2 \\ &+ \sum_{\mathbf{q}''_\parallel, \mathbf{q}'''_\parallel} |\langle G^+(\mathbf{q}_\parallel, \mathbf{q}''_\parallel) \rangle|^2 W_{\mathbf{q}''_\parallel, \mathbf{q}'''_\parallel} |\langle G^+(\mathbf{q}'''_\parallel, \mathbf{q}'_\parallel) \rangle|^2 \end{aligned} \quad (\text{B.37})$$

where the term $W_{\mathbf{q}''_\parallel, \mathbf{q}'''_\parallel}$ is called the reducible vertex function. To the lowest order, the vertex function reads[158],

$$W_{\mathbf{q}''_\parallel, \mathbf{q}'''_\parallel} = \frac{V_2}{A} \quad (\text{B.38})$$

From Eq. B.35 to Eq. B.38, we obtain the expression for the transmission probability matrix,

$$\begin{aligned} \langle T_{\mathbf{q}_\parallel, \mathbf{q}'_\parallel} \rangle &= \delta_{\mathbf{q}_\parallel, \mathbf{q}'_\parallel} \frac{4\rho_L \rho_R v_L v_R}{|\rho_L v_L + \rho_R v_R|^2} \\ &\times \left[1 - 2\text{Re} \mathcal{G}^+ \omega^{-1} V_2 \left(\frac{1}{\rho_L v_L + \rho_R v_R} \right) \right] \\ &+ \frac{4\omega^{-2} V_2}{A} \frac{\rho_R v_R}{|\rho_L v_L + \rho_R v_R|^2} \frac{\rho_L v'_L}{|\rho_L v'_L + \rho_R v'_R|^2} \end{aligned} \quad (\text{B.39})$$

where $\mathcal{G}^+ = \left(\sum_{\mathbf{q}''_\parallel} iG_0^+(\mathbf{q}''_\parallel) \right)/A$ and the analytical expression for \mathcal{G}^+ can be found in the next session. We identify that the diagonal term is responsible for specular transmission, while the off-diagonal term is responsible for diffuse transmission. Similarly, from Eq. B.10b, Eq. B.32 and Eq. B.35 , we derive that the reflection probability

matrix writes,

$$\begin{aligned} \langle R_{\mathbf{q}_{\parallel}, \mathbf{q}'_{\parallel}} \rangle &= \delta_{\mathbf{q}_{\parallel}, \mathbf{q}'_{\parallel}} \frac{|\rho_L v_L - \rho_R v_R|^2}{|\rho_L v_L + \rho_R v_R|^2} \\ &\times \left[1 - 4 \operatorname{Re} \mathcal{G}^+ \omega^{-1} V_2 \operatorname{Re} \left(\frac{\rho_L v_L}{\rho_L^2 v_L^2 - \rho_R^2 v_R^2} \right) \right] \\ &+ \frac{4 \omega^{-2} V_2}{A} \frac{\rho_L v_L}{|\rho_L v_L + \rho_R v_R|^2} \frac{\rho_L v'_L}{|\rho_L v'_L + \rho_R v'_R|^2}. \end{aligned} \quad (\text{B.40})$$

B.1.5 The analytical expression of \mathcal{G}^+

The term \mathcal{G}^+ in Eq. B.39 and Eq. B.40 can be written in terms of an integral over all transverse wavevectors,

$$\begin{aligned} \mathcal{G}^+ &= \int \frac{d^2 \mathbf{q}_{\parallel}}{(2\pi)^2} \frac{1}{\sqrt{\mu_L(\rho_L \omega^2 - \mu_L q_{\parallel}^2)} + \sqrt{\mu_R(\rho_R \omega^2 - \mu_R q_{\parallel}^2)}} \end{aligned} \quad (\text{B.41})$$

Introduce the ratio of bulk moduli as $a = \rho_R/\rho_L$ and $b = \mu_R/\mu_L$. Depending on the bulk moduli and densities of two sides, the expression for the real part of \mathcal{G}^+ is as follows. When $(b-a)(1-b^2) > 0$,

$$\begin{aligned} \operatorname{Re} \mathcal{G}^+ &= \frac{\omega \mathcal{G}_0^+}{1-b^2} \left[1 - \sqrt{ab} + \sqrt{\frac{b(b-a)}{1-b^2}} \right. \\ &\quad \left. \times \left(\operatorname{atan} \sqrt{\frac{a(1-b^2)}{b-a}} - \operatorname{atan} \sqrt{\frac{1-b^2}{b(b-a)}} \right) \right] \end{aligned} \quad (\text{B.42})$$

where $\mathcal{G}_0^+ = \frac{1}{2\pi\mu_L} \sqrt{\frac{\rho_L}{\mu_L}}$ and for Si, $\mathcal{G}_0^+ = 2.62 \times 10^{-16} \text{ s}^3/\text{kg}$. When $(b-a)(1-b^2) < 0$,

$$\begin{aligned} \operatorname{Re} \mathcal{G}^+ &= \frac{\omega \mathcal{G}_0^+}{1-b^2} \left[1 - \sqrt{ab} + \frac{1}{2} \sqrt{\frac{b(a-b)}{1-b^2}} \right. \\ &\quad \left. \times \left(\ln \frac{|1 - \sqrt{\frac{b(a-b)}{1-b^2}}|}{1 + \sqrt{\frac{b(a-b)}{1-b^2}}} - \ln \frac{|1 - \sqrt{\frac{a-b}{a(1-b^2)}}|}{1 + \sqrt{\frac{a-b}{a(1-b^2)}}} \right) \right] \end{aligned} \quad (\text{B.43})$$

When $b = 1$ and $a \neq 1$,

$$\text{Re } \mathcal{G}^+ = \frac{\omega \mathcal{G}_0^+}{3} \frac{1 - a^{\frac{3}{2}}}{1 - a} \quad (\text{B.44})$$

When $a = b$,

$$\text{Re } \mathcal{G}^+ = \frac{\omega \mathcal{G}_0^+}{1 + b} \quad (\text{B.45})$$

B.1.6 The specular and diffuse transmittance/reflectance

The transmittance for a given initial state \mathbf{q}_{\parallel} is defined by summing transition probabilities to different final states \mathbf{q}'_{\parallel} ,

$$T_{L \rightarrow R}(\mathbf{q}_{\parallel}) = \sum_{\mathbf{q}'_{\parallel}} \langle T_{\mathbf{q}'_{\parallel}, \mathbf{q}_{\parallel}} \rangle \quad (\text{B.46})$$

where $\langle T_{\mathbf{q}'_{\parallel}, \mathbf{q}_{\parallel}} \rangle$ is the transmission probability matrix defined in Eq. B.39.

In the following, we will use direction $\Omega_L = (\theta_L, \phi_L)$ to denote a phonon state \mathbf{q}_{\parallel} , where $(\mathbf{q}_{\parallel}, q_L) = \frac{\omega}{c_L}(\sin\theta_L \cos\phi, \sin\theta_L \sin\phi, \cos\theta_L)$. Note that the group velocity is parallel to the wavevector thus the angles for the group velocity and the wavevector are the same. After integration, the transmittance in Eq. B.46 is given by,

$$\begin{aligned} T_{L \rightarrow R}(\Omega_L) &= T_{s, L \rightarrow R}(\Omega_L) + T_{d, L \rightarrow R}(\Omega_L) \\ &= T_{\text{AMM}}(\Omega_L) p_T(\Omega_L) + T_{d, L \rightarrow R}(\Omega_L) \end{aligned} \quad (\text{B.47})$$

The first term is the specular transmittance, which is the product of transmittance from AMM[93, 91],

$$T_{\text{AMM}}(\Omega_L) = \frac{4\rho_L \rho_R v_L v_R}{|\rho_L v_L + \rho_R v_R|^2} \quad (\text{B.48})$$

and the specularity parameter for transmittance,

$$p_T(\Omega_L) = 1 - 2\text{Re } \mathcal{G}^+ \omega^{-1} V_2 \left(\frac{1}{\rho_L v_L + \rho_R v_R} \right) \quad (\text{B.49})$$

The second term, diffuse transmittance, is given by Eq. 3.13 in Sec. 3.2.

Similarly, the reflectance for a given incident state from the left side is given by,

$$\begin{aligned}
R_{L \rightarrow L}(\Omega_L) &= \sum_{\mathbf{q}'_{||}} \langle R_{\mathbf{q}'_{||}, \mathbf{q}_{||}} \rangle \\
&= R_{s, L \rightarrow L}(\Omega_L) + R_{d, L \rightarrow L}(\Omega_L) \\
&= R_{\text{AMM}}(\Omega_L) p_R(\Omega_L) + R_{d, L \rightarrow L}(\Omega_L)
\end{aligned} \tag{B.50}$$

where $\langle R_{\mathbf{q}'_{||}, \mathbf{q}_{||}} \rangle$ is the reflection probability matrix defined in Eq. B.40. The reflectance by AMM writes,

$$R_{\text{AMM}}(\Omega_L) = \frac{|\rho_L v_L - \rho_R v_R|^2}{|\rho_L v_L + \rho_R v_R|^2} \tag{B.51}$$

The specularity parameter for reflectance is given by,

$$p_R(\Omega_L) = 1 - 4 \operatorname{Re} \mathcal{G}^+ \omega^{-1} V_2 \operatorname{Re} \left(\frac{\rho_L v_L}{\rho_L^2 v_L^2 - \rho_R^2 v_R^2} \right) \tag{B.52}$$

And the diffuse reflectance $R_{d, L \rightarrow L}(\Omega_L)$ is defined by Eq. 3.15. We want to stress that the expressions in Eq. B.47 and Eq. B.50 add up to one in the current lowest-order perturbation theory, which means our continuum model is a self-consistent theory. However, this is not a guaranteed property at higher orders.

In the previous study of partially specular and partially specular interface scattering by a disordered interface[159], the transmittance and reflectance are often phenomenologically written as,

$$T(\Omega) = p(\Omega) T_{\text{AMM}}(\Omega) + (1 - p(\Omega)) T_{\text{DMM}}(\Omega) \tag{B.53a}$$

$$R(\Omega) = p(\Omega) R_{\text{AMM}}(\Omega) + (1 - p(\Omega)) R_{\text{DMM}}(\Omega) \tag{B.53b}$$

where p is the specularity parameter calculated by Ziman's equation[160]. However, in our continuum modeling, there are two specularity parameters, one for transmittance (Eq. B.49), one for reflectance (eq. B.52) and they are generally not equal. The necessity of two specularity parameters has been hypothesized by Li *et al*[161] and our analytical model gives direct support for the hypothesis of two different specularity parameters. What's more, it is entirely possible to have p_R in our model larger than

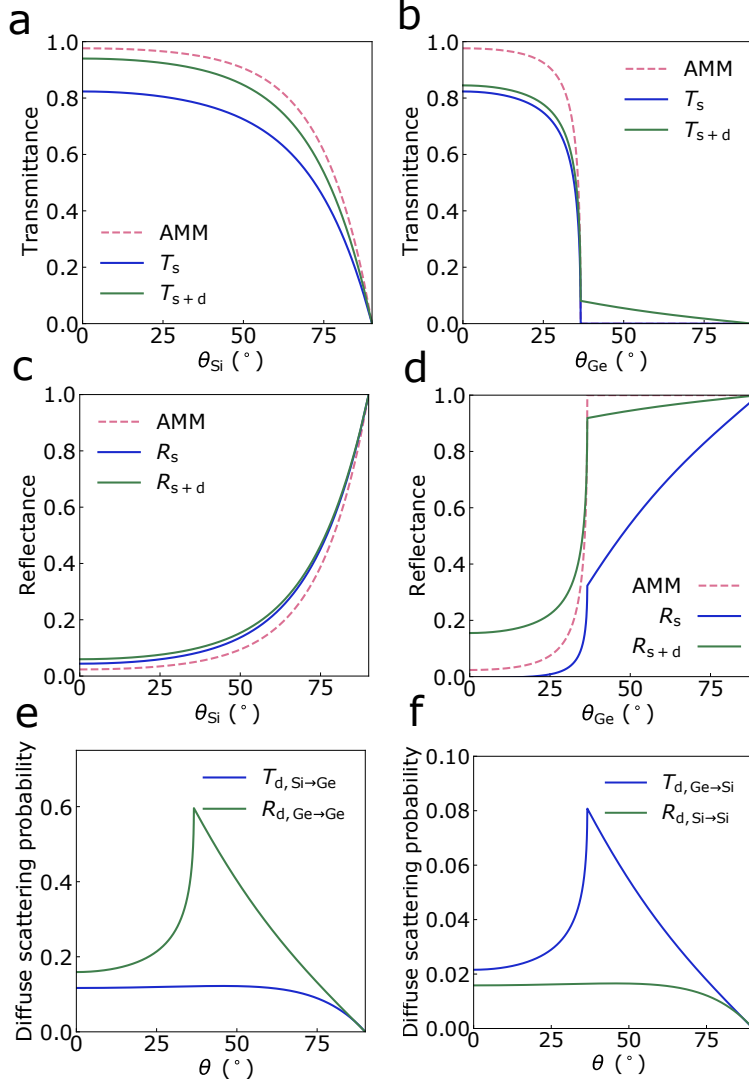


Figure B-1: The transmittance and reflectance for a rough Si/Ge interface predicted from the continuum model. (a) and (b): The specular and diffuse transmittance of acoustic phonons at 4 THz in Si and Ge compared with AMM. (c) and (d): The specular and diffuse reflectance of acoustic phonons at 4 THz in Si and Ge compared with AMM. (e) and (f): The diffuse transmittance from one side and reflectance from the other side of acoustic phonons at 4 THz. θ is the velocity angle of the incident state.

one (this is also observed in AGF calculation presented in the supplementary material in Ref. [76]), while the specularity parameter p given by Ziman's equation is bounded by one. Thus, the specularity parameter is merely a correction factor and cannot be interpreted as probability of being specularly scattered.

Similar to Eq. 3.20, we further compute the frequency-resolved average transmit-

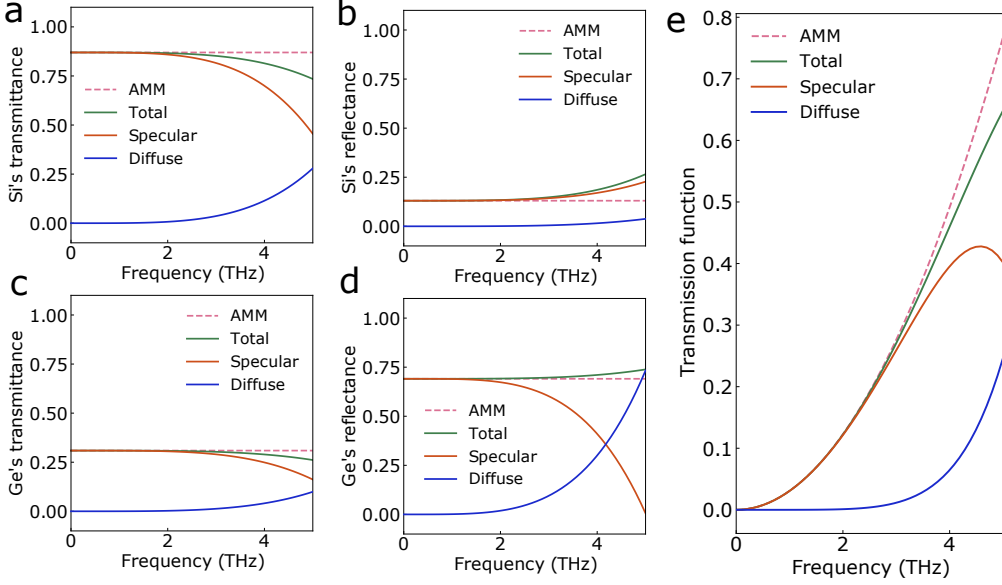


Figure B-2: (a)-(d) The frequency-resolved transmittance and reflectance from Si side and Ge side from continuum modeling. (e) The transmission function $\Theta(\omega)$ for Si/Ge interface as a function of frequency. A multiplicity factor of three is multiplied in the transmission function as there are three acoustic phonon branches. When the frequency is much higher than 5 Thz, the lowest perturbation theory is no longer valid, as the perturbed part becomes large.

tance by integrating over solid angle,

$$T_{L \rightarrow R}(\omega) = 2 \int_0^{\pi/2} d\theta \sin\theta \cos\theta T_{L \rightarrow R}(\Omega_L) \quad (\text{B.54})$$

and the reflectance can be similarly computed. The energy-resolved transmission function, which measures the number of conduction channels for interfacial thermal transport, is obtained by,

$$\begin{aligned} \Theta(\omega) &= A \int \frac{d^2 \mathbf{q}_\parallel}{(2\pi)^2} T_{L \rightarrow R}(\omega, \mathbf{q}_\parallel) \\ &= 2\pi A \int \frac{d^2 \mathbf{q}_\parallel dq_L}{(2\pi)^3} T_{L \rightarrow R}(\Omega_L) v_L \delta(\omega - c_L \sqrt{q_\parallel^2 + q_L^2}) \\ &= \pi A D_L(\omega) c_L \int_0^{\pi/2} d\theta \sin\theta \cos\theta T_{L \rightarrow R}(\Omega_L) \end{aligned} \quad (\text{B.55})$$

where $D_L(\omega) = \frac{\omega^2}{2\pi^2 c_L^3}$ is the density of states of left side and $\sin\theta = |\mathbf{q}_\parallel| c_L / \omega$. The two-probe interfacial thermal conductance per unit area is determined by the transmission

function,

$$G = \frac{1}{2\pi A} \int_0^\infty \hbar\omega \Theta(\omega) \frac{\partial f(\omega, T)}{\partial T} d\omega \quad (\text{B.56})$$

where $f(\omega, T)$ is the Bose-Einstein distribution function.

B.2 Numerical calculations

B.2.1 The interface scattering transition probability for a rough Si/Ge interface

We apply the derived equations for transmittance and reflectance for a rough Si/Ge interface along [001] direction. If we assume the atomic mixing is realized by swapping Si and Ge atoms on two sides of interface, the variance of mass fluctuations is estimated to be $\langle m_i^2 \rangle \approx (m_{\text{Si}} - m_{\text{Ge}})^2 = 1.985 \times 10^3 u^2$. Thus, the parameter $V_2 = n \langle m_i^2 \rangle \omega^4$, where n is the number of pairs of swapped Si and Ge atoms per unit area. We choose $n = 2/a^2$ in the following calculation, and $a = 5.527 \text{ \AA}$ is the lattice constant, obtained by taking the average of Si's and Ge's lattice constants. The bulk moduli of Si and Ge are $\mu_L = 95 \text{ GPa}$ and $\mu_R = 77.2 \text{ GPa}$. The densities of Si and Ge are $\rho_L = 2.329 \times 10^3 \text{ kg/m}^3$ and $\rho_R = 5.323 \times 10^3 \text{ kg/m}^3$.

As shown in Fig. B-1, we find that the phonon transmittance of Si is smaller compared with AMM. Although there are more transmission channels due to diffuse scattering, the reduction of transmittance is mainly due to fewer specular transmission channels, which are removed by interfacial disorders. In addition, we note that the diffuse transmission from the Ge side opens new transmission channels above the critical angle for total reflection. Furthermore, we find that the reflectance from the Si side increases with the angle, similar to the trend of AMM. For reflectance from the Ge side, the specular part is smaller than AMM. Due to large diffuse reflectance shown in Fig. B-1 (e), the total reflection probability is eventually higher than predictions of AMM below the critical angle and lower above the critical angle. In fact, from the expression of Eq. B.39 and Eq. B.40, we find that the specular transmittance is always reduced by disorders while the specular reflectance can either be enhanced or

reduced depending on the sign of $\rho_L v_L - \rho_R v_R$.

From Fig. B-1 (e) and (f), we observe that generally the diffuse transmittance from one side is different from the diffuse reflectance from the other side. Furthermore, we find that as frequency increases, the specular scattering probability decreases while the diffuse scattering probability increases, as shown in Fig. B-2 (a)-(d). For the transmittance from both sides, the reduction in the specular part is always larger than the increment in the diffuse part, hence a reduced total transmittance. In contrast, for reflectance, the increment in the diffuse part prevails over the reduction in the specular part, causing a greater total reflectance. When we compare the phonon transmission function for Si/Ge interface in Fig. B-2 (e), the interface disorders lead to a smaller total transmission, thus a smaller thermal conductance. Note that when $\omega > 5$ THz, the specular reflectance from Ge side will become negative, because the perturbation is no longer a small quantity. From Eq. B.52, we see that the reduction in the specularity parameter for reflectance p_R varies drastically with frequency with ω^4 scaling. When $p_R \sim 0$, we have a critical frequency $\omega \sim \left(\frac{\mu^2 A}{\langle m_i^2 \rangle}\right)^{1/4}$, and our model only works below this critical frequency.

To summarize, continuum modeling using perturbation theory to the lowest order suggests that the diffuse scattering cannot make a phonon forget its origin, opposing the picture of DMM. However, we want to point out limitations of the continuum model of scalar phonons. First of all, the phonon mode conversion is not considered. Secondly, the model is valid for low-frequency acoustic phonons thus at lifted temperatures, where high-frequency phonons are playing an important role in interfacial phonon transport, the model is no longer valid.

Appendix C

The transient grating signals for phase gratings

In this Appendix, we derive the expression for the TTG signals with phase grating for layered systems.

C.1 The model

C.1.1 General solutions

The heat equation writes,

$$\nabla \cdot (\kappa \nabla T) = \rho C \frac{\partial T}{\partial t}, \quad (\text{C.1})$$

where κ is the thermal conductivity tensor, a rank-2 tensor in three-dimensional system and T is the temperature. Here, we assume that the thermal conductivity tensor is not affected by elastic deformations. The equation of thermoelasticity writes[141],

$$(1 - 2\nu) \nabla^2 \mathbf{u} + \nabla (\nabla \cdot \mathbf{u}) + \mathbf{F} = 2(1 + \nu) \alpha_{\text{th}} \nabla T + \rho \frac{\partial^2 \mathbf{u}}{\partial t^2}, \quad (\text{C.2})$$

where \mathbf{u} is the displacement vector, ν is the Poisson's ratio related to Lamé constants through $\nu = \frac{\lambda}{2(\lambda+\mu)}^1$, α_{th} is the (volume) thermal expansion coefficient and \mathbf{F} is the

¹Some important related identities: $\lambda = \frac{\nu E}{(1+\nu)(1-2\nu)}$, $\mu = \frac{E}{2(1+\nu)}$.

applied force. For the case of TTG, there is no external force term. We further assume the inertia term is negligible as it often evolves much faster than the heat diffusion process. The simplified equation becomes,

$$(1 - 2\nu)\nabla^2\mathbf{u} + \nabla(\nabla \cdot \mathbf{u}) = 2(1 + \nu)\alpha_{\text{th}}\nabla T. \quad (\text{C.3})$$

Considering the periodic geometry of the transient grating, we can write the temperature and displacement in form of plane waves as,

$$\begin{aligned} T &= \tilde{T}(\omega, q, z) e^{i(\omega t + qx)}, \\ \mathbf{u} &= \tilde{\mathbf{u}}(\omega, q, z) e^{i(\omega t + qx)}. \end{aligned} \quad (\text{C.4})$$

We immediately identify the solution to the heat equation,

$$\tilde{T} = Ae^{-\zeta z} + Be^{\zeta z}, \quad (\text{C.5})$$

where $\zeta = \sqrt{(q^2\kappa_x + i\rho C\omega)/\kappa_z}$ and κ_x and κ_z are the in-plane and out-of-plane thermal conductivity.

As for the displacement, applying Helmholtz decomposition, we have

$$\mathbf{u} = \nabla\Phi + \nabla \times \Psi, \quad (\text{C.6})$$

where $\Psi = (\Psi_x, \Psi_y, \Psi_z)^T$ is a vector potential. By construction, we can express the scalar and vector potential as,

$$\begin{aligned} \Phi &= \tilde{\Phi}(\omega, q, z) e^{i(\omega t + qx)}, \\ \Psi &= \tilde{\Psi}(\omega, q, z) e^{i(\omega t + qx)}. \end{aligned} \quad (\text{C.7})$$

Plug Eq. C.7 into Eq. C.3, we have following identity,

$$\nabla(\nabla^2\phi - \gamma T) = \nabla \times (-\chi\nabla^2\Psi) \quad (\text{C.8})$$

where $\chi = \frac{1-2\nu}{2(1-\nu)}$, $\gamma = \frac{1+\nu}{1-\nu}\alpha_{\text{th}}$ and ∇^2 is the vector Laplacian. We explicitly write down the equations for different components of Ψ from Eq. C.8,

$$\begin{aligned} \frac{\partial}{\partial x} \left(\frac{\partial^2 \Phi}{\partial x^2} + \frac{\partial^2 \Phi}{\partial z^2} - \gamma T \right) &= \chi \frac{\partial}{\partial z} \nabla^2 \Psi_y, \\ \frac{\partial}{\partial x} \left(\frac{\partial^2 \Psi_x}{\partial z^2} \right) - \frac{\partial}{\partial z} \left(\frac{\partial^2 \Psi_z}{\partial x^2} \right) &= 0, \\ \frac{\partial}{\partial z} \left(\frac{\partial^2 \Phi}{\partial x^2} + \frac{\partial^2 \Phi}{\partial z^2} - \gamma T \right) &= -iq\chi \nabla^2 \Psi_y. \end{aligned} \quad (\text{C.9})$$

It is easy to show that Eq. C.9 lead to,

$$\frac{\partial^4 \tilde{\Phi}}{\partial z^4} - 2q^2 \frac{\partial^2 \tilde{\Phi}}{\partial z^2} + q^4 \tilde{\Phi} = \chi \left(\frac{\partial^2 \tilde{T}}{\partial z^2} - q^2 \tilde{T} \right). \quad (\text{C.10})$$

The special solution to Eq. C.10 is $\frac{\gamma A}{\zeta^2 - q^2} e^{-\zeta z} + \frac{\gamma B}{\zeta^2 - q^2} e^{\zeta z}$. Thus, the solution to Eq. C.10 is given by,

$$\tilde{\Phi} = M_1 e^{qz} + M_2 z e^{qz} + N_1 e^{-qz} + N_2 z e^{-qz} - \frac{\gamma A}{\zeta^2 - q^2} e^{-\zeta z} + \frac{\gamma B}{\zeta^2 - q^2} e^{\zeta z}. \quad (\text{C.11})$$

Without loss of generality, we choose a Coulomb gauge, where the vector potential $\nabla \cdot \Psi = 0$. With the knowledge of Φ , we obtain the y-component of Ψ ,

$$\Psi_y = \left[\frac{2i}{\chi} (M_2 z e^{qz} - N_2 z e^{-qz}) + G e^{-qz} + H e^{qz} \right] e^{i(\omega t + qx)} \quad (\text{C.12})$$

Thus, we are able to express the general solution for displacement, consistent with Ref. [141]. One can also directly solve Eq. C.2,

$$\begin{aligned} \frac{\partial^2 u_x}{\partial x^2} + \chi \frac{\partial^2 u_x}{\partial z^2} + \frac{iq}{2(1-\nu)} \frac{\partial u_z}{\partial z} &= \gamma \frac{\partial T}{\partial x} \\ \frac{\partial^2 u_z}{\partial z^2} + \chi \frac{\partial^2 u_z}{\partial x^2} + \frac{iq}{2(1-\nu)} \frac{\partial u_x}{\partial z} &= \gamma \frac{\partial T}{\partial z} \end{aligned} \quad (\text{C.13})$$

Define $x_1 = u_x$, $x_2 = \frac{\partial u_x}{\partial z}$, $y_1 = u_z$ and $y_2 = \frac{\partial u_z}{\partial z}$. We can express the relationship

between the displacement on the bottom and on the top of the first layer,

$$\begin{pmatrix} x'_1 \\ x'_2 \\ y'_1 \\ y'_2 \end{pmatrix} = \begin{pmatrix} 0 & 1 & 0 & 0 \\ \frac{q^2}{\chi} & 0 & 0 & \frac{-iq}{1-2\nu} \\ 0 & 0 & 0 & 1 \\ 0 & \frac{-iq}{2(1-\nu)} & \chi q^2 & 0 \end{pmatrix} \begin{pmatrix} x_1 \\ x_2 \\ y_1 \\ y_2 \end{pmatrix} = \mathbf{M} \cdot \mathbf{x} \quad (\text{C.14})$$

The eigenvalues are $-q, q$ and the eigenvectors are, $\mathbf{v}_1 = \left(\frac{i}{q}, -i, -\frac{1}{q}, 1\right)^T$ and $\mathbf{v}_2 = \left(\frac{i}{q}, i, \frac{1}{q}, 1\right)^T$. Since the eigenvalue $-q$ has two-fold degeneracy, the solution is $\mathbf{x} = z\exp(-qz)\mathbf{v}_1 + \exp(-qz)\mathbf{v}'_1$, where \mathbf{v}'_1 is determined by $(\mathbf{M} - (-q)\mathbf{I}) \cdot \mathbf{v}'_1 = \mathbf{v}_1$. We can also solve for \mathbf{v}'_2 similarly. As a result, we have $\mathbf{v}'_1 = \left(\frac{2i(-1+2\nu)}{q^2}, -\frac{-i(-3+4\nu)}{q}, -\frac{1}{q^2}, 0\right)^T$ and $\mathbf{v}'_2 = \left(\frac{-2i(-1+2\nu)}{q^2}, -\frac{-i(-3+4\nu)}{q}, -\frac{1}{q^2}, 0\right)^T$. Therefore, the solution reads, $\mathbf{x} = c_1 e^{-qz}\mathbf{v}_1 + c_2 (ze^{-qz}\mathbf{v}_1 + e^{-qz}\mathbf{v}'_1) + d_1 e^{qz}\mathbf{v}_2 + d_2 (ze^{qz}\mathbf{v}_2 + e^{qz}\mathbf{v}'_2)$. Finally, the displacements along x and z direction are,

$$\begin{aligned} u_x &= -C_1 ie^{-qz} + C_2 i (3 - 4\nu - qz) e^{-qz} + iC_3 e^{qz} + C_4 i (3 - 4\nu + qz) e^{qz} \\ &\quad + \frac{\gamma}{\zeta^2 - q^2} [iq(Ae^{-\zeta z} + Be^{\zeta z})], \\ u_z &= C_1 e^{-qz} + C_2 qze^{-qz} + C_3 e^{qz} + C_4 qze^{qz} \\ &\quad + \frac{\gamma}{\zeta^2 - q^2} [\zeta(-Ae^{-\zeta z} + Be^{\zeta z})]. \end{aligned} \quad (\text{C.15})$$

C.1.2 Free surface boundary condition

The free surface suggests that $\sigma_{zz} = \sigma_{xz} = 0$. The strain read $\varepsilon_{\alpha\alpha} = \frac{\partial u_\alpha}{\partial \alpha}$ and $\varepsilon_{xz} = \frac{1}{2} \left(\frac{\partial u_x}{\partial z} + \frac{\partial u_z}{\partial x} \right)$. The stress is determined by Duhamel-Neumann relations[162],

$$\sigma_{ij} = \lambda \delta_{ij} \varepsilon_{kk} + 2\mu \varepsilon_{ij} - \delta_{ij} (3\lambda + 2\mu) \alpha_{\text{th}} T. \quad (\text{C.16})$$

Specifically, we explicitly write down the two relevant strain components,

$$\begin{aligned} \sigma_{zz} &= iq\lambda u_x + (\lambda + 2\mu) \frac{\partial u_z}{\partial z} - (3\lambda + 2\mu) \alpha_{\text{th}} T, \\ \sigma_{xz} &= iq\mu u_z + \mu \frac{\partial u_x}{\partial z}. \end{aligned} \quad (\text{C.17})$$

The boundary condition for displacements writes,

$$\begin{aligned} \nu \frac{\partial u_x}{\partial x} + (1 - \nu) \frac{\partial u_z}{\partial z} - (1 + \nu) \alpha_{\text{th}} T &= 0, \\ \frac{\partial u_x}{\partial z} + \frac{\partial u_z}{\partial x} &= 0. \end{aligned} \quad (\text{C.18})$$

Solving the above equations renders $\tilde{u}_z(z = 0) = -\frac{2\alpha_{\text{th}}A(1+\nu)}{\beta+q}$. To integrate the signal, one needs following identity,

$$I = \int_{-\infty}^{\infty} dx e^{iax^2} = \sqrt{\frac{i\pi}{a}}, \quad a > 0. \quad (\text{C.19})$$

When calculating the displacement gradient,

$$\frac{\partial u_z}{\partial x} = -Q_0 q_0 \sin(q_0 x) \int \tilde{h}(\omega) \tilde{u}_z(q_0) e^{i\omega t} d\omega, \quad (\text{C.20})$$

the following integral is involved,

$$\int_{-\infty}^{\infty} \frac{e^{i\omega t} d\omega}{\sqrt{i\omega + c} (\sqrt{i\omega + c} + d)} \quad (\text{C.21})$$

where $c = q^2 \kappa_x$ and $d = q \sqrt{\kappa_z}$ are pure real number. One first split the integral into two part $\omega \in [-\infty, 0]$ and $\omega \in [0, +\infty]$, and denote $i\omega + c = u$. For the second part,

$$I_2 = e^{-ct} \int_c^{c+i\infty} \frac{e^{ut} du / i}{(\sqrt{u} + d) \sqrt{u}} \quad (\text{C.22})$$

Let $m = \sqrt{u} + d$,

$$I_2 = 2e^{-ct}/i \int_{\sqrt{c+d}}^{\sqrt{c+i\infty}+d} \frac{e^{(m-d)^2 t} dm}{m + d} \quad (\text{C.23})$$

Using Cauchy's integral theorem, the integral is equivalent to,

$$I_2 = 2e^{-ct} \int_0^{\infty} \frac{e^{-y^2 t} (d - iy) dy}{d^2 + y^2} \quad (\text{C.24})$$

Similarly, the first part of the integral is,

$$I_1 = -2e^{-ct} \int_0^\infty \frac{e^{-y^2 t}(d+iy)dy}{d^2+y^2} \quad (\text{C.25})$$

Therefore, the integral can be expressed by,

$$I = 2e^{-ct} d \int_0^\infty \frac{e^{-y^2 t}}{d^2+y^2}. \quad (\text{C.26})$$

Using the identity from Ref. [163], we have,

$$I = \pi e^{-ct+d^2 t} \operatorname{erfc}(d\sqrt{t}) = \pi e^{-(\kappa_x - \kappa_z)q^2 t} \operatorname{erfc}\left(q\sqrt{\frac{\kappa_z t}{\rho C}}\right), \quad (\text{C.27})$$

where the complementary error function is defined by,

$$\operatorname{erfc}(z) = \frac{2}{\sqrt{\pi}} \int_z^\infty e^{-t^2} dt. \quad (\text{C.28})$$

The displacement at surface now can be expressed,

$$\frac{\partial u_z}{\partial x}(z=0) = \frac{E_0(1+\nu)\alpha_{\text{th}}}{\rho C} q_0 \sin(q_0 x) e^{-(\kappa_x - \kappa_z)q^2 t} \operatorname{erfc}\left(q\sqrt{\frac{\kappa_z t}{\rho C}}\right). \quad (\text{C.29})$$

C.1.3 Transfer matrix

In this section, we drop the \sim for compactness. At given frequency ω , the temperature and heat flux of the n the layer can be expressed,

$$\begin{pmatrix} T_n \\ Q_n \end{pmatrix} = \mathbf{M}_n \mathbf{N}_n \mathbf{R}_{n-1} \dots \mathbf{R}_1 \mathbf{M}_1 \mathbf{N}_1 = \begin{pmatrix} A & B \\ C & D \end{pmatrix} \begin{pmatrix} T_1 \\ Q_1 \end{pmatrix}, \quad (\text{C.30})$$

For amplitude grating, above 2×2 transfer matrices can be used and compute the signal. The matrices involved read,

$$\mathbf{M}_i = \begin{pmatrix} e^{\beta L_i} & e^{-\beta L_i} \\ -(\kappa_z \beta)_i e^{\beta L_i} & (\kappa_z \beta)_i e^{-\beta L_i} \end{pmatrix}, \quad \mathbf{N}_i = \begin{pmatrix} \frac{1}{2} & -\frac{1}{2(\kappa_z \beta)_i} \\ \frac{1}{2} & \frac{1}{2(\kappa_z \beta)_i} \end{pmatrix} \text{ and } \mathbf{R}_i = \begin{pmatrix} 1 & -\frac{1}{G} \\ 0 & 1 \end{pmatrix}. \quad (\text{C.31})$$

$$\mathbf{M}_i \mathbf{N}_i = \begin{pmatrix} \cosh(\beta L_i) & -\frac{\sinh(\beta L_i)}{\kappa_z \beta_i} \\ -\kappa_z \beta_i \sinh(\beta L_i) & \cosh(\beta L_i) \end{pmatrix} \quad (\text{C.32})$$

where $\beta = \sqrt{(q^2 \kappa_{x,i} + i \rho_i C_i \omega) / \kappa_{z,i}}$. The adiabatic boundary condition for bottom layer and surface heating boundary condition $Q_1 = Q_0$ leads to, $CT_1 + DQ_0 = 0$. Equivalently, $T_1 = -\frac{D}{C}Q_0$.

Consider all physical quantities in the system,

$$\begin{pmatrix} T \\ Q \\ u_x \\ u_z \\ \sigma_{xz} \\ \sigma_{zz} \end{pmatrix} = \begin{pmatrix} e^{-\beta z} & e^{\beta z} & 0 & 0 & 0 & 0 \\ \kappa_z \beta e^{-\beta z} & -\kappa_z \beta e^{\beta z} & 0 & 0 & 0 & 0 \\ Giqe^{-\beta z} & Giqe^{\beta z} & -ie^{-qz} & ie^{-qz} H^-(z) & ie^{qz} & ie^{qz} H^+(z) \\ -G\beta e^{-\beta z} & G\beta e^{\beta z} & e^{-qz} & qze^{-qz} & e^{qz} & qze^{qz} \\ -2i\mu G\beta qe^{-\beta z} & 2i\mu G\beta qe^{\beta z} & 2i\mu qe^{-qz} & 2i\mu qe^{-qz} I^-(z) & 2i\mu qe^{qz} & 2i\mu qe^{qz} I^+(z) \\ 2\mu Gq^2 e^{-\beta z} & 2\mu Gq^2 e^{\beta z} & -2\mu qe^{-qz} & -2\mu qe^{-qz} J^-(z) & 2\mu qe^{qz} & 2\mu qe^{qz} J^+(z) \end{pmatrix} \begin{pmatrix} A \\ B \\ C_1 \\ C_2 \\ C_3 \\ C_4 \end{pmatrix}, \quad (\text{C.33})$$

where

$$G = \frac{\gamma}{\beta^2 - q^2},$$

$$H^-(z) = 3 - 4\nu - qz,$$

$$H^+(z) = 3 - 4\nu + qz,$$

$$I^-(z) = -2 + 2\nu + qz,$$

$$I^+(z) = 2 - 2\nu + qz,$$

$$J^-(z) = I^-(z) + 1,$$

$$J^+(z) = I^+(z) - 1.$$

Apparently, for an isotropic material where $\kappa_x = \kappa_z$, the coefficient G diverges. To ensure the numerical accuracy, we need to rescale the variables by some constants. Typically, temperature is around several K . Take the grating period to be around 10^{-5} m (typically ranging from $1 \mu\text{m}$ to $15 \mu\text{m}$). The coefficient $\beta \sim 10^5 \text{ m}^{-1}$. The heat flux is usually around 10^5 W/m^2 . Normally, the thermal expansion $\alpha \sim 10^{-5} \text{ K}^{-1}$ thus $G \sim 10^{-15} \text{ K}^{-1} \text{ m}^2$. Accordingly, the displacement is around 10^{-10} m . If we take

$\mu \sim 10^{10}$ Pa, the stress is around 10^5 Pa. The rescaled equation is,

$$\begin{pmatrix} T \\ r_1 Q \\ r_2 u_x \\ r_3 u_z \\ r_4 \sigma_{xz} \\ r_5 \sigma_{zz} \end{pmatrix} = \begin{pmatrix} a_1 & a_2 & a_3 & a_4 & a_5 & a_6 \\ r_1 b_1 & r_1 b_2 & b_3 & b_4 & b_5 & b_6 \\ r_2 c_1 & r_2 c_2 & c_3 & c_4 & c_5 & c_6 \\ r_3 d_1 & r_3 d_2 & \frac{r_3}{r_2} d_3 & \frac{r_3}{r_2} d_4 & \frac{r_3}{r_2} d_5 & \frac{r_3}{r_2} d_6 \\ r_4 e_1 & r_4 e_2 & \frac{r_4}{r_2} e_3 & \frac{r_4}{r_2} e_4 & \frac{r_4}{r_2} e_5 & \frac{r_4}{r_2} e_6 \\ r_5 f_1 & r_5 f_2 & \frac{r_5}{r_2} f_3 & \frac{r_5}{r_2} f_4 & \frac{r_5}{r_2} f_5 & \frac{r_5}{r_2} f_6 \end{pmatrix} \begin{pmatrix} A \\ B \\ r_2 C_1 \\ r_2 C_2 \\ r_2 C_3 \\ r_2 C_4 \end{pmatrix}, \quad (\text{C.34})$$

where the letter and subscripts denote the row and column of unscaled matrix.

Denote the above 6×6 matrix $\mathbf{M}_i(z)$, the vector of physical quantities $\mathbf{p}_i(z)$ and the vector of coefficients \mathbf{c}_i for i th layer. When $z = 0$, we can express the coefficients $\mathbf{c}_i = [\mathbf{M}_i(z = 0)]^{-1} \mathbf{p}_i(0)$. Let's denote $\mathbf{N}_i = [\mathbf{M}_i(z = 0)]^{-1}$ and $\mathbf{M}_i = \mathbf{M}_i(z = L_i)$, where L_i the thickness of i th layer. At the interface between the i th layer and the $i + 1$ th layer, the stress has to match such that $\sigma_{zz,i} = \sigma_{zz,i+1}$ and $\sigma_{xz,i} = \sigma_{xz,i+1}$. The displacement needs to match as well, $u_{x,i} = u_{x,i+1}$ and $u_{z,i} = u_{z,i+1}$. We now write these conditions in matrix form,

$$\begin{pmatrix} T \\ r_1 Q \\ r_2 u_x \\ r_3 u_z \\ r_4 \sigma_{xz} \\ r_5 \sigma_{zz} \end{pmatrix}_{i+1} = \begin{pmatrix} 1 & -\frac{1}{r_1 G} & 0 & 0 & 0 & 0 \\ 0 & 1 & 0 & 0 & 0 & 0 \\ 0 & 0 & 1 & 0 & 0 & 0 \\ 0 & 0 & 0 & 1 & 0 & 0 \\ 0 & 0 & 0 & 0 & 1 & 0 \\ 0 & 0 & 0 & 0 & 0 & 1 \end{pmatrix} \begin{pmatrix} T \\ r_1 Q \\ r_2 u_x \\ r_3 u_z \\ r_4 \sigma_{xz} \\ r_5 \sigma_{zz} \end{pmatrix}_i \quad (\text{C.35})$$

We denote the above matrix as R_i . At this moment, we can relate the physical properties of top layer (1 st) to the bottom layer (n th) by,

$$\mathbf{p}_n = \mathbf{M}_n \mathbf{N}_n \mathbf{R}_{n-1} \dots \mathbf{R}_1 \mathbf{M}_1 \mathbf{N}_1 \mathbf{p}_1 = \mathbf{T} \mathbf{p}_1. \quad (\text{C.36})$$

Choosing adiabatic boundary for bottom layer, $Q_n = 0$. If the bottom layer is thick enough, we can set $u_{x,n} = u_{z,n} = 0$. For top layer, $Q_1 = Q_0$ and $\sigma_{xz,1} = \sigma_{zz,1} = 0$. We

have,

$$\begin{pmatrix} T \\ 0 \\ 0 \\ 0 \\ r_4\sigma_{xz} \\ r_5\sigma_{zz} \end{pmatrix}_n = \mathbf{T} \begin{pmatrix} T \\ r_1Q_0 \\ r_2u_x \\ r_3u_z \\ 0 \\ 0 \end{pmatrix}_1 \quad (\text{C.37})$$

Introduce a vector,

$$\mathbf{x} = \begin{pmatrix} T_n & r_4\sigma_{xz,n} & r_5\sigma_{zz,n} & T_1 & r_2u_{x,1} & r_3u_{z,1} \end{pmatrix}^T \quad (\text{C.38})$$

Convert this to a matrix equation problem $\mathbf{Ax} = \mathbf{b}$, where

$$\mathbf{A} = \begin{pmatrix} -1 & 0 & 0 & a_1 & a_3 & a_4 \\ 0 & 0 & 0 & b_1 & b_3 & b_4 \\ 0 & 0 & 0 & c_1 & c_3 & c_4 \\ 0 & 0 & 0 & d_1 & d_3 & d_4 \\ 0 & -1 & 0 & e_1 & e_3 & e_4 \\ 0 & 0 & -1 & f_1 & f_3 & f_4 \end{pmatrix} \quad (\text{C.39})$$

and

$$\mathbf{b} = -r_1Q_0 \begin{pmatrix} a_2 & b_2 & c_2 & d_2 & e_2 & f_2 \end{pmatrix}^T, \quad (\text{C.40})$$

where letter indicates the row and number indicates the column of matrix \mathbf{T} , for example, $c_2 = T_{3,2}$. In practice, the rescaling constant can be chosen differently when calculating the response at different frequency. Consequently, the analytical solution for u_z at the given ω is,

$$u_z = -r_1Q_0 \frac{b_3c_2d_1 - b_2c_3d_1 - b_3c_1d_2 + b_1c_3d_2 + b_2c_1d_3 - b_1c_2d_3}{-b_4c_3d_1 + b_3c_4d_1 + b_4c_1d_3 - b_1c_4d_3 - b_3c_1d_4 + b_1c_3d_4}. \quad (\text{C.41})$$

The time-dependent $u_z(t)$ can be obtained by applying the inverse Fourier transform to $u_z(\omega)$.

Bibliography

- [1] David G Cahill, Paul V Braun, Gang Chen, David R Clarke, Shanhui Fan, Kenneth E Goodson, Paweł Kebinski, William P King, Gerald D Mahan, Arun Majumdar, et al. Nanoscale thermal transport. ii. 2003–2012. *Applied Physics Reviews*, 1(1):011305, 2014.
- [2] Gang Chen. Non-fourier phonon heat conduction at the microscale and nanoscale. *Nature Reviews Physics*, pages 1–15, 2021.
- [3] Keivan Esfarjani, Gang Chen, and Harold T. Stokes. Heat transport in silicon from first-principles calculations. *Phys. Rev. B*, 84:085204, Aug 2011.
- [4] HBG Casimir. Note on the conduction of heat in crystals. *Physica*, 5(6):495–500, 1938.
- [5] Renkun Chen, Allon I. Hochbaum, Padraig Murphy, Joel Moore, Peidong Yang, and Arun Majumdar. Thermal conductance of thin silicon nanowires. *Phys. Rev. Lett.*, 101:105501, Sep 2008.
- [6] John Cuffe, Jeffrey K. Eliason, A. A. Maznev, Kimberlee C. Collins, Jeremy A. Johnson, Andrey Shchepetov, Mika Prunnila, Jouni Ahopelto, Clivia M. Sotomayor Torres, Gang Chen, and Keith A. Nelson. Reconstructing phonon mean-free-path contributions to thermal conductivity using nanoscale membranes. *Phys. Rev. B*, 91:245423, Jun 2015.
- [7] Wu Li, Jesús Carrete, Nabil A Katcho, and Natalio Mingo. Shengbte: A solver of the boltzmann transport equation for phonons. *Computer Physics Communications*, 185(6):1747–1758, 2014.
- [8] E. T. Swartz and R. O. Pohl. Thermal boundary resistance. *Rev. Mod. Phys.*, 61:605–668, Jul 1989.
- [9] Ashutosh Giri and Patrick E Hopkins. A review of experimental and computational advances in thermal boundary conductance and nanoscale thermal transport across solid interfaces. *Advanced Functional Materials*, 30(8):1903857, 2020.
- [10] Rolf Landauer. Spatial variation of currents and fields due to localized scatterers in metallic conduction. *IBM Journal of Research and Development*, 1(3):223–231, 1957.

- [11] O. Koblinger, J. Mebert, E. Dittrich, S. Döttinger, W. Eisenmenger, P. V. Santos, and L. Ley. Phonon stop bands in amorphous superlattices. *Phys. Rev. B*, 35:9372–9375, Jun 1987.
- [12] T. Tsuchiya, H. Akera, and T. Ando. Phonons in gaas/ala_s superlattices. *Phys. Rev. B*, 39:6025–6033, Mar 1989.
- [13] Maria N Luckyanova, Jivtesh Garg, Keivan Esfarjani, Adam Jndl, Mayank T Bulsara, Aaron J Schmidt, Austin J Minnich, Shuo Chen, Mildred S Dresselhaus, Zhifeng Ren, et al. Coherent phonon heat conduction in superlattices. *Science*, 338(6109):936–939, 2012.
- [14] P. W. Anderson. Absence of diffusion in certain random lattices. *Phys. Rev.*, 109:1492–1505, Mar 1958.
- [15] Mordechai Segev, Yaron Silberberg, and Demetrios N Christodoulides. Anderson localization of light. *Nature Photonics*, 7(3):197–204, 2013.
- [16] Tianping Ying, Yueqiang Gu, Xiao Chen, Xinbo Wang, Shifeng Jin, Linlin Zhao, Wei Zhang, and Xiaolong Chen. Anderson localization of electrons in single crystals: Lixfe₇se₈. *Science Advances*, 2(2):e1501283, 2016.
- [17] Hefei Hu, A Strybulevych, JH Page, Sergey E Skipetrov, and Bart A van Tiggenlen. Localization of ultrasound in a three-dimensional elastic network. *Nature Physics*, 4(12):945–948, 2008.
- [18] Juliette Billy, Vincent Josse, Zhanchun Zuo, Alain Bernard, Ben Hambrecht, Pierre Lugan, David Clément, Laurent Sanchez-Palencia, Philippe Bouyer, and Alain Aspect. Direct observation of anderson localization of matter waves in a controlled disorder. *Nature*, 453(7197):891–894, 2008.
- [19] Maria N Luckyanova, Jonathan Mendoza, Hong Lu, Bai Song, Shengxi Huang, Jiawei Zhou, Mingda Li, Yongqi Dong, Hua Zhou, Joseph Garlow, et al. Phonon localization in heat conduction. *Science Advances*, 4(12):eaat9460, 2018.
- [20] PW Anderson. The size of localized states near the mobility edge. *Proceedings of the National Academy of Sciences*, 69(5):1097–1099, 1972.
- [21] Gary Wolfowicz, F Joseph Heremans, Christopher P Anderson, Shun Kanai, Hosung Seo, Adam Gali, Giulia Galli, and David D Awschalom. Quantum guidelines for solid-state spin defects. *Nature Reviews Materials*, pages 1–20, 2021.
- [22] David A Broido, Michael Malorny, Gerd Birner, Natalio Mingo, and DA Steward. Intrinsic lattice thermal conductivity of semiconductors from first principles. *Applied Physics Letters*, 91(23):231922, 2007.

- [23] Bolin Liao, Bo Qiu, Jiawei Zhou, Samuel Huberman, Keivan Esfarjani, and Gang Chen. Significant reduction of lattice thermal conductivity by the electron-phonon interaction in silicon with high carrier concentrations: A first-principles study. *Phys. Rev. Lett.*, 114:115901, Mar 2015.
- [24] Jivtesh Garg, Nicola Bonini, Boris Kozinsky, and Nicola Marzari. Role of disorder and anharmonicity in the thermal conductivity of silicon-germanium alloys: A first-principles study. *Phys. Rev. Lett.*, 106:045901, Jan 2011.
- [25] Tao Wang, Jesús Carrete, Ambroise van Roekeghem, Natalio Mingo, and Georg K. H. Madsen. Ab initio phonon scattering by dislocations. *Phys. Rev. B*, 95:245304, Jun 2017.
- [26] L. Lindsay, D. A. Broido, and T. L. Reinecke. Phonon-isotope scattering and thermal conductivity in materials with a large isotope effect: A first-principles study. *Phys. Rev. B*, 88:144306, Oct 2013.
- [27] Natalio Mingo, K. Esfarjani, D. A. Broido, and D. A. Stewart. Cluster scattering effects on phonon conduction in graphene. *Phys. Rev. B*, 81:045408, Jan 2010.
- [28] D. J. Thouless. Maximum metallic resistance in thin wires. *Phys. Rev. Lett.*, 39:1167–1169, Oct 1977.
- [29] David Ferry and Stephen Marshall Goodnick. *Transport in Nanostructures*. Number 6. Cambridge University Press, 1999.
- [30] Daniel S. Fisher and Patrick A. Lee. Relation between conductivity and transmission matrix. *Phys. Rev. B*, 23:6851–6854, Jun 1981.
- [31] G. Chen. Phonon Wave Heat Conduction in Thin Films and Superlattices. *Journal of Heat Transfer*, 121(4):945–953, 11 1999.
- [32] Jayakanth Ravichandran, Ajay K Yadav, Ramez Cheaito, Pim B Rossen, Arsen Soukiassian, SJ Suresha, John C Duda, Brian M Foley, Che-Hui Lee, Ye Zhu, et al. Crossover from incoherent to coherent phonon scattering in epitaxial oxide superlattices. *Nature Materials*, 13(2):168–172, 2014.
- [33] Shin-ichiro Tamura. Isotope scattering of dispersive phonons in ge. *Phys. Rev. B*, 27:858–866, Jan 1983.
- [34] Ping Sheng. *Introduction to wave scattering, localization and mesoscopic phenomena*, volume 88. Springer Science & Business Media, 2006.
- [35] Supriyo Datta. *Electronic Transport in Mesoscopic Systems*. Cambridge University Press, 1997.
- [36] Supriyo Datta. Nanoscale device modeling: the green’s function method. *Superlattices and Microstructures*, 28(4):253–278, 2000.

- [37] Wei Zhang, TS Fisher, and Natalio Mingo. The atomistic green's function method: An efficient simulation approach for nanoscale phonon transport. *Numerical Heat Transfer, Part B: Fundamentals*, 51(4):333–349, 2007.
- [38] Gang Chen. Diffusion–transmission interface condition for electron and phonon transport. *Applied Physics Letters*, 82(6):991–993, 2003.
- [39] Herbert Kroemer. Nobel lecture: Quasielectric fields and band offsets: teaching electrons new tricks. *Rev. Mod. Phys.*, 73:783–793, Oct 2001.
- [40] Haruhisa Soda, Ken-ichi Iga, Chiyuki Kitahara, and Yasuharu Suematsu. Gainasp/inp surface emitting injection lasers. *Japanese Journal of Applied Physics*, 18(12):2329, 1979.
- [41] K Tai, L Yang, YH Wang, JD Wynn, and AY Cho. Drastic reduction of series resistance in doped semiconductor distributed bragg reflectors for surface-emitting lasers. *Applied Physics Letters*, 56(25):2496–2498, 1990.
- [42] MG Peters, BJ Thibeault, DB Young, JW Scott, FH Peters, AC Gossard, and LA Coldren. Band-gap engineered digital alloy interfaces for lower resistance vertical-cavity surface-emitting lasers. *Applied Physics Letters*, 63(25):3411–3413, 1993.
- [43] Herbert Kroemer. Heterostructure bipolar transistors and integrated circuits. *Proceedings of the IEEE*, 70(1):13–25, 1982.
- [44] Mark S Lundstrom and Robert J Schuelke. Numerical analysis of heterostructure semiconductor devices. *IEEE Transactions on Electron Devices*, 30(9):1151–1159, 1983.
- [45] H Page, C Becker, A Robertson, G Glastre, V Ortiz, and C Sirtori. 300 k operation of a GaAs-based quantum-cascade laser at $\lambda \approx 9 \mu\text{m}$. *Applied Physics Letters*, 78(22):3529–3531, 2001.
- [46] BF Levine, CG Bethea, G Hasnain, VO Shen, E Pelve, RR Abbott, and SJ Hsieh. High sensitivity low dark current $10 \mu\text{m}$ GaAs quantum well infrared photodetectors. *Applied Physics Letters*, 56(9):851–853, 1990.
- [47] Gang Chen, Taofang Zeng. Energy conversion in heterostructures for thermionic cooling. *Microscale Thermophysical Engineering*, 4(1):39–50, 2000.
- [48] Gehong Zeng, A Shakouri, CL Bounty, G Robinson, E Croke, P Abraham, Xiafeng Fan, H Reese, and JE Bowers. SiGe micro-cooler. *Electronics Letters*, 35(24):2146–2147, 1999.
- [49] SC Jain and W Hayes. Structure, properties and applications of gexsi1-x strained layers and superlattices. *Semiconductor Science and Technology*, 6(7):547, 1991.

- [50] Giordano Scappucci, Christoph Kloeffel, Floris A Zwanenburg, Daniel Loss, Maksym Myronov, Jian-Jun Zhang, Silvano De Franceschi, Georgios Katsaros, and Menno Veldhorst. The germanium quantum information route. *Nature Reviews Materials*, pages 1–18, 2020.
- [51] L. A. Terrazos, E. Marcellina, Zhanning Wang, S. N. Coppersmith, Mark Friesen, A. R. Hamilton, Xuedong Hu, Belita Koiller, A. L. Saraiva, Dimitrie Culcer, and Rodrigo B. Capaz. Theory of hole-spin qubits in strained germanium quantum dots. *Phys. Rev. B*, 103:125201, Mar 2021.
- [52] N F Hinsche, I Mertig, and P Zahn. Thermoelectric transport in strained si and si/ge heterostructures. *Journal of Physics: Condensed Matter*, 24(27):275501, jun 2012.
- [53] T. Koga, X. Sun, S. B. Cronin, and M. S. Dresselhaus. Carrier pocket engineering applied to “strained” Si/Ge superlattices to design useful thermoelectric materials. *Applied Physics Letters*, 75(16):2438–2440, 1999.
- [54] T Koga, SB Cronin, MS Dresselhaus, JL Liu, and KL Wang. Experimental proof-of-principle investigation of enhanced z 3d t in (001) oriented Si/Ge superlattices. *Applied Physics Letters*, 77(10):1490–1492, 2000.
- [55] Daryoosh Vashaee and Ali Shakouri. Improved thermoelectric power factor in metal-based superlattices. *Phys. Rev. Lett.*, 92:106103, Mar 2004.
- [56] B. Laikhtman and S. Luryi. Landauer formula for transmission across an interface. *Phys. Rev. B*, 49:17177–17184, Jun 1994.
- [57] Dietmar Schroeder. *Modelling of Interface Carrier Transport for Device Simulation*. Springer Science & Business Media, 1994.
- [58] Hideki Takeuchi, Pushkar Ranade, Vivek Subramanian, and Tsu-Jae King. Observation of dopant-mediated intermixing at Ge/Si interface. *Applied Physics Letters*, 80(20):3706–3708, 2002.
- [59] Arrigo Calzolari, Nicola Marzari, Ivo Souza, and Marco Buongiorno Nardelli. Ab initio transport properties of nanostructures from maximally localized wannier functions. *Phys. Rev. B*, 69:035108, Jan 2004.
- [60] Nick Papior, Nicolás Lorente, Thomas Frederiksen, Alberto García, and Mads Brandbyge. Improvements on non-equilibrium and transport green function techniques: The next-generation transiesta. *Computer Physics Communications*, 212:8–24, 2017.
- [61] Magnus Paulsson and Mads Brandbyge. Transmission eigenchannels from nonequilibrium green’s functions. *Phys. Rev. B*, 76:115117, Sep 2007.

- [62] Jeremy Taylor, Hong Guo, and Jian Wang. Ab initio modeling of quantum transport properties of molecular electronic devices. *Phys. Rev. B*, 63:245407, Jun 2001.
- [63] Anisur Rahman, Jing Guo, Supriyo Datta, and Mark S Lundstrom. Theory of ballistic nanotransistors. *IEEE Transactions on Electron Devices*, 50(9):1853–1864, 2003.
- [64] Oleg V Yazyev and Steven G Louie. Electronic transport in polycrystalline graphene. *Nature Materials*, 9(10):806–809, 2010.
- [65] Daniele Stradi, Umberto Martinez, Anders Blom, Mads Brandbyge, and Kurt Stokbro. General atomistic approach for modeling metal-semiconductor interfaces using density functional theory and nonequilibrium green’s function. *Phys. Rev. B*, 93:155302, Apr 2016.
- [66] Bernhard Kretz, Christian S. Pedersen, Daniele Stradi, Mads Brandbyge, and Aran Garcia-Lekue. Atomistic insight into the formation of metal-graphene one-dimensional contacts. *Phys. Rev. Applied*, 10:024016, Aug 2018.
- [67] Gerrit E. W. Bauer. Perpendicular transport through magnetic multilayers. *Phys. Rev. Lett.*, 69:1676–1679, Sep 1992.
- [68] J. Barnaś, A. Fuss, R. E. Camley, P. Grünberg, and W. Zinn. Novel magnetoresistance effect in layered magnetic structures: Theory and experiment. *Phys. Rev. B*, 42:8110–8120, Nov 1990.
- [69] Th. G. S. M. Rijks, R. Coehoorn, M. J. M. de Jong, and W. J. M. de Jonge. Semiclassical calculations of the anisotropic magnetoresistance of nife-based thin films, wires, and multilayers. *Phys. Rev. B*, 51:283–291, Jan 1995.
- [70] J. Mathon. Ab initio calculation of the perpendicular giant magnetoresistance of finite Co/Cu(001) and Fe/Cr(001) superlattices with fluctuating layer thicknesses. *Phys. Rev. B*, 55:960–969, Jan 1997.
- [71] E. Bellotti, F. Bertazzi, A. Tibaldi, J. Schuster, J. Bajaj, and M. Reed. Disorder-induced degradation of vertical carrier transport in strain-balanced antimony-based superlattices. *Phys. Rev. Applied*, 16:054028, Nov 2021.
- [72] Alberto Tibaldi, Jesús A. Gonzalez Montoya, Matteo G. C. Alasio, Alberto Gullino, Anders Larsson, Pierluigi Debernardi, Michele Goano, Marco Vallone, Giovanni Ghione, Enrico Bellotti, and Francesco Bertazzi. Analysis of carrier transport in tunnel-junction vertical-cavity surface-emitting lasers by a coupled nonequilibrium Green’s function–drift-diffusion approach. *Phys. Rev. Applied*, 14:024037, Aug 2020.
- [73] V. F. Los. Self-consistent theory of scattering at disordered interfaces in layered nanostructures. *Phys. Rev. B*, 72:115441, Sep 2005.

- [74] Voicu Popescu and Alex Zunger. Effective band structure of random alloys. *Phys. Rev. Lett.*, 104:236403, Jun 2010.
- [75] P. A. Khomyakov, G. Brocks, V. Karpan, M. Zwierzycki, and P. J. Kelly. Conductance calculations for quantum wires and interfaces: Mode matching and Green's functions. *Phys. Rev. B*, 72:035450, Jul 2005.
- [76] Qichen Song and Gang Chen. Evaluation of the diffuse mismatch model for phonon scattering at disordered interfaces. *Phys. Rev. B*, 104:085310, Aug 2021.
- [77] B Yang, WL Liu, JL Liu, KL Wang, and G Chen. Measurements of anisotropic thermoelectric properties in superlattices. *Applied Physics Letters*, 81(19):3588–3590, 2002.
- [78] Jean-Marc Jancu, Reinhard Scholz, Fabio Beltram, and Franco Bassani. Empirical spds* tight-binding calculation for cubic semiconductors: General method and material parameters. *Phys. Rev. B*, 57:6493–6507, Mar 1998.
- [79] J. C. Slater and G. F. Koster. Simplified LCAO method for the periodic potential problem. *Phys. Rev.*, 94:1498–1524, Jun 1954.
- [80] Y. M. Niquet, D. Rideau, C. Tavernier, H. Jaouen, and X. Blase. Onsite matrix elements of the tight-binding hamiltonian of a strained crystal: Application to silicon, germanium, and their alloys. *Phys. Rev. B*, 79:245201, Jun 2009.
- [81] *We are interested in the interface scattering by the atomically rough interfaces. Hence, we focus on the domain within the range of \sim nm to the interface, where the lattice constant does not vary drastically. Thus, we assume the Si-Si, Ge-Ge bond lengths are the same with Si-Ge bond length of 2.3979 \AA in the domain of our simulation. That is to say, the Si/Ge interface structure is the same with bulk Si's structure except some atoms are substituted by Ge atoms.*
- [82] *The band structure transits from Si to Ge with a discontinuity of valence band edge known as the valence band offset. In addition, depending on the carrier concentrations of Si and Ge side, the band structures of Si and Ge vary with distance to the interface known as band bending. The characteristic length of band bending is the Debye length, which is typically around ~ 10 to ~ 100 nm. Since we focus on the interface scattering in the proximity of rough interfaces (below 10 nm), we neglect the band bending and assume a constant band edge profile in Si side and Ge side. As for the band offset across the Si/Ge interface, we use the value of 0.68 eV for bond length $L = L_0 = 2.398 \text{ \AA}$.*
- [83] Eleftherios N Economou. *Green's Functions in Quantum Physics*, volume 7. Springer Science & Business Media, 2006.
- [84] V. Gurarie. Single-particle Green's functions and interacting topological insulators. *Phys. Rev. B*, 83:085426, Feb 2011.

- [85] Mildred S Dresselhaus, Gene Dresselhaus, and Ado Jorio. *Group Theory: Application to the Physics of Condensed Matter*. Springer Science & Business Media, 2007.
- [86] L. P. Bouckaert, R. Smoluchowski, and E. Wigner. Theory of brillouin zones and symmetry properties of wave functions in crystals. *Phys. Rev.*, 50:58–67, Jul 1936.
- [87] Mois I Aroyo, Asen Kirov, Cesar Capillas, JM Perez-Mato, and Hans Wondratschek. Bilbao crystallographic server. ii. representations of crystallographic point groups and space groups. *Acta Crystallographica Section A: Foundations of Crystallography*, 62(2):115–128, 2006.
- [88] Jurgen Michel, Jifeng Liu, and Lionel C Kimerling. High-performance ge-on-si photodetectors. *Nature Photonics*, 4(8):527–534, 2010.
- [89] Hosung Seo, Richard C. Hatch, Patrick Ponath, Miri Choi, Agham B. Posadas, and Alexander A. Demkov. Critical differences in the surface electronic structure of ge(001) and si(001): Ab initio theory and angle-resolved photoemission spectroscopy. *Phys. Rev. B*, 89:115318, Mar 2014.
- [90] Arne Brataas and Gerrit E. W. Bauer. Semiclassical theory of perpendicular transport and giant magnetoresistance in disordered metallic multilayers. *Phys. Rev. B*, 49:14684–14699, May 1994.
- [91] WA Little. The transport of heat between dissimilar solids at low temperatures. *Canadian Journal of Physics*, 37(3):334–349, 1959.
- [92] P.L. Kapitza. *Zh. Eksp. Teor. Fiz.*, 11(1), 1941.
- [93] I. M. Khalatnikov. *Zh. Eksp. Teor. Fiz.*, 22(687), 1952.
- [94] Ho-Ki Lyeo and David G. Cahill. Thermal conductance of interfaces between highly dissimilar materials. *Phys. Rev. B*, 73:144301, Apr 2006.
- [95] Zhe Cheng, Yee Rui Koh, Habib Ahmad, Renjiu Hu, Jingjing Shi, Michael E Liao, Yekan Wang, Tingyu Bai, Ruiyang Li, Eungkyu Lee, et al. Thermal conductance across harmonic-matched epitaxial al-sapphire heterointerfaces. *Communications Physics*, 3(1):1–8, 2020.
- [96] Y. Chalopin, K. Esfarjani, A. Henry, S. Volz, and G. Chen. Thermal interface conductance in si/ge superlattices by equilibrium molecular dynamics. *Phys. Rev. B*, 85:195302, May 2012.
- [97] Kiarash Gordiz and Asegun Henry. A formalism for calculating the modal contributions to thermal interface conductance. *New Journal of Physics*, 17(10):103002, 2015.

- [98] Kiarash Gordiz and Asegun Henry. Phonon transport at crystalline Si/Ge interfaces: the role of interfacial modes of vibration. *Scientific Reports*, 6(1):1–9, 2016.
- [99] E. S. Landry and A. J. H. McGaughey. Thermal boundary resistance predictions from molecular dynamics simulations and theoretical calculations. *Phys. Rev. B*, 80:165304, Oct 2009.
- [100] K. Sääskilahti, J. Oksanen, J. Tulkki, and S. Volz. Role of anharmonic phonon scattering in the spectrally decomposed thermal conductance at planar interfaces. *Phys. Rev. B*, 90:134312, Oct 2014.
- [101] Nuo Yang, Tengfei Luo, Keivan Esfarjani, Asegun Henry, Zhiting Tian, Junichiro Shiomi, Yann Chalopin, Baowen Li, and Gang Chen. Thermal interface conductance between aluminum and silicon by molecular dynamics simulations. *Journal of Computational and Theoretical Nanoscience*, 12(2):168–174, 2015.
- [102] Yann Chalopin and Sebastian Volz. A microscopic formulation of the phonon transmission at the nanoscale. *Applied Physics Letters*, 103(5):051602, 2013.
- [103] Chris Kimmer, Sylvie Aubry, Ashton Skye, and Patrick K. Schelling. Scattering of phonons from a high-energy grain boundary in silicon: Dependence on angle of incidence. *Phys. Rev. B*, 75:144105, Apr 2007.
- [104] Bowen Deng, Aleksandr Chernatynskiy, Marat Khafizov, David H Hurley, and Simon R Phillipot. Kapitza resistance of Si/SiO₂ interface. *Journal of Applied Physics*, 115(8):084910, 2014.
- [105] W. Zhang, T. S. Fisher, and N. Mingo. Simulation of interfacial phonon transport in si–ge heterostructures using an atomistic green’s function method. *Journal of Heat Transfer*, 129(4):483–491, 05 2006.
- [106] Zhiting Tian, Keivan Esfarjani, and Gang Chen. Enhancing phonon transmission across a si/ge interface by atomic roughness: First-principles study with the green’s function method. *Phys. Rev. B*, 86:235304, Dec 2012.
- [107] Zhun-Yong Ong and Gang Zhang. Efficient approach for modeling phonon transmission probability in nanoscale interfacial thermal transport. *Phys. Rev. B*, 91:174302, May 2015.
- [108] Sridhar Sadashivam, Umesh V. Waghmare, and Timothy S. Fisher. Phonon-eigenspectrum-based formulation of the atomistic Green’s function method. *Phys. Rev. B*, 96:174302, Nov 2017.
- [109] Benoit Latour, Nina Shulumba, and Austin J. Minnich. Ab initio study of mode-resolved phonon transmission at Si/Ge interfaces using atomistic green’s functions. *Phys. Rev. B*, 96:104310, Sep 2017.

- [110] Zhun-Yong Ong, Georg Schusteritsch, and Chris J. Pickard. Structure-specific mode-resolved phonon coherence and specularity at graphene grain boundaries. *Phys. Rev. B*, 101:195410, May 2020.
- [111] Zhun-Yong Ong. Specular transmission and diffuse reflection in phonon scattering at grain boundary. *EPL (Europhysics Letters)*, 133(6):66002, mar 2021.
- [112] D. A. Young and H. J. Maris. Lattice-dynamical calculation of the Kapitza resistance between fcc lattices. *Phys. Rev. B*, 40:3685–3693, Aug 1989.
- [113] H Zhao and JB Freund. Lattice-dynamical calculation of phonon scattering at ideal Si – Ge interfaces. *Journal of Applied Physics*, 97(2):024903, 2005.
- [114] Simon Lu and Alan JH McGaughey. Thermal conductance of graphene/hexagonal boron nitride heterostructures. *Journal of Applied Physics*, 121(11):115103, 2017.
- [115] MP Lopez Sancho, JM Lopez Sancho, JM Lopez Sancho, and J Rubio. Highly convergent schemes for the calculation of bulk and surface Green functions. *Journal of Physics F: Metal Physics*, 15(4):851, 1985.
- [116] Caio H. Lewenkopf and Eduardo R. Mucciolo. The recursive Green’s function method for graphene. *Journal of Computational Electronics*, 12(2):203–231, May 2013.
- [117] Fernando Sols, M. Macucci, U. Ravaioli, and Karl Hess. Theory for a quantum modulated transistor. *Journal of Applied Physics*, 66(8):3892–3906, October 1989.
- [118] At a given transverse wavevector \mathbf{q}_{\parallel} , there are multiple phonon states with different q_z or degenerate states with the same q_z . Here, we use \mathbf{q}_{\parallel} to describe one of those states.
- [119] C Caroli, R Combescot, P Nozieres, and D Saint-James. Direct calculation of the tunneling current. *Journal of Physics C: Solid State Physics*, 4(8):916–929, jun 1971.
- [120] Kedong Bi, Jianqiang Wang, Yujuan Wang, Jingjie Sha, Zan Wang, Minhua Chen, and Yunfei Chen. The thermal conductivity of SiGe heterostructure nanowires with different cores and shells. *Physics Letters A*, 376(40-41):2668–2671, 2012.
- [121] One may be concerned about the contribution from specularity parameter to the diffuse transmittance and reflectance. We have discussed the role of specularity parameter in diffuse scattering in the supplementary material in Ref. [76].
- [122] Lina Yang, Benoit Latour, and Austin J. Minnich. Phonon transmission at crystalline-amorphous interfaces studied using mode-resolved atomistic Green’s functions. *Phys. Rev. B*, 97:205306, May 2018.

- [123] Xufei Wu and Tengfei Luo. The importance of anharmonicity in thermal transport across solid-solid interfaces. *Journal of Applied Physics*, 115(1):014901, 2014.
- [124] Tianli Feng, Yang Zhong, Jingjing Shi, and Xiulin Ruan. Unexpected high inelastic phonon transport across solid-solid interface: Modal nonequilibrium molecular dynamics simulations and landauer analysis. *Phys. Rev. B*, 99:045301, Jan 2019.
- [125] Jinghang Dai and Zhiting Tian. Rigorous formalism of anharmonic atomistic Green's function for three-dimensional interfaces. *Phys. Rev. B*, 101:041301, Jan 2020.
- [126] Yangyu Guo, Zhongwei Zhang, Marc Bescond, Shiyun Xiong, Masahiro Nomura, and Sebastian Volz. Anharmonic phonon-phonon scattering at the interface between two solids by nonequilibrium Green's function formalism. *Phys. Rev. B*, 103:174306, May 2021.
- [127] Ivana Savić, Natalio Mingo, and Derek A. Stewart. Phonon transport in isotope-disordered carbon and boron-nitride nanotubes: Is localization observable? *Phys. Rev. Lett.*, 101:165502, Oct 2008.
- [128] Abhishek Chaudhuri, Anupam Kundu, Dibyendu Roy, Abhishek Dhar, Joel L. Lebowitz, and Herbert Spohn. Heat transport and phonon localization in mass-disordered harmonic crystals. *Phys. Rev. B*, 81:064301, Feb 2010.
- [129] Takahiro Yamamoto, Kenji Sasaoka, and Satoshi Watanabe. Universality and diversity in a phonon-transmission histogram of isotope-disordered carbon nanotubes. *Phys. Rev. Lett.*, 106:215503, May 2011.
- [130] Jonathan Mendoza and Gang Chen. Anderson localization of thermal phonons leads to a thermal conductivity maximum. *Nano letters*, 16(12):7616–7620, 2016.
- [131] Taneli Juntunen, Osmo Vänskä, and Ilkka Tittonen. Anderson localization quenches thermal transport in aperiodic superlattices. *Phys. Rev. Lett.*, 122:105901, Mar 2019.
- [132] E. Abrahams, P. W. Anderson, D. C. Licciardello, and T. V. Ramakrishnan. Scaling theory of localization: Absence of quantum diffusion in two dimensions. *Phys. Rev. Lett.*, 42:673–676, Mar 1979.
- [133] Varouzhan Baluni and Jorge Willemsen. Transmission of acoustic waves in a random layered medium. *Phys. Rev. A*, 31:3358–3363, May 1985.
- [134] John M Ziman et al. *Models of Disorder: the Theoretical Physics of Homogeneously Disordered Systems*. CUP Archive, 1979.

- [135] Yan Wang, Haoxiang Huang, and Xiulin Ruan. Decomposition of coherent and incoherent phonon conduction in superlattices and random multilayers. *Phys. Rev. B*, 90:165406, Oct 2014.
- [136] Qian Xu, Jiawei Zhou, Te-Huan Liu, and Gang Chen. Effect of electron-phonon interaction on lattice thermal conductivity of SiGe alloys. *Applied Physics Letters*, 115(2):023903, 2019.
- [137] Jia Yang, Carlo Maragliano, and Aaron J Schmidt. Thermal property microscopy with frequency domain thermoreflectance. *Review of Scientific Instruments*, 84(10):104904, 2013.
- [138] David G Cahill. Analysis of heat flow in layered structures for time-domain thermoreflectance. *Review of Scientific Instruments*, 75(12):5119–5122, 2004.
- [139] Aaron J Schmidt, Xiaoyuan Chen, and Gang Chen. Pulse accumulation, radial heat conduction, and anisotropic thermal conductivity in pump-probe transient thermoreflectance. *Review of Scientific Instruments*, 79(11):114902, 2008.
- [140] Puqing Jiang, Xin Qian, and Ronggui Yang. Tutorial: Time-domain thermoreflectance (tdtr) for thermal property characterization of bulk and thin film materials. *Journal of Applied Physics*, 124(16):161103, 2018.
- [141] OW Käding, H Skurk, AA Maznev, and E Matthias. Transient thermal gratings at surfaces for thermal characterization of bulk materials and thin films. *Applied Physics A*, 61(3):253–261, 1995.
- [142] AA Maznev, KA Nelson, and JA Rogers. Optical heterodyne detection of laser-induced gratings. *Optics letters*, 23(16):1319–1321, 1998.
- [143] Jeremy A Johnson, Alexei A Maznev, Mayank T Bulsara, Eugene A Fitzgerald, TC Harman, S Calawa, CJ Vineis, G Turner, and Keith A Nelson. Phase-controlled, heterodyne laser-induced transient grating measurements of thermal transport properties in opaque material. *Journal of Applied Physics*, 111(2):023503, 2012.
- [144] Jeremy A. Johnson, A. A. Maznev, John Cuffe, Jeffrey K. Eliason, Austin J. Minnich, Timothy Kehoe, Clivia M. Sotomayor Torres, Gang Chen, and Keith A. Nelson. Direct measurement of room-temperature nondiffusive thermal transport over micron distances in a silicon membrane. *Phys. Rev. Lett.*, 110:025901, Jan 2013.
- [145] Samuel Huberman, Ryan A Duncan, Ke Chen, Bai Song, Vazrik Chiloyan, Zhiwei Ding, Alexei A Maznev, Gang Chen, and Keith A Nelson. Observation of second sound in graphite at temperatures above 100 k. *Science*, 364(6438):375–379, 2019.
- [146] Hans Joachim Eichler, Peter Günter, and Dieter W Pohl. *Laser-induced Dynamic Gratings*, volume 50. Springer, 2013.

- [147] Alejandro Vega-Flick, Daehwan Jung, Shengying Yue, John E. Bowers, and Bolin Liao. Reduced thermal conductivity of epitaxial GaAs on Si due to symmetry-breaking biaxial strain. *Phys. Rev. Materials*, 3:034603, Mar 2019.
- [148] AS McLeod, E Van Heumen, JG Ramirez, S Wang, T Saerbeck, S Guenon, M Goldflam, L Anderegg, P Kelly, A Mueller, et al. Nanotextured phase coexistence in the correlated insulator V₂O₃. *Nature Physics*, 13(1):80–86, 2017.
- [149] Javier Del Valle, Pavel Salev, Federico Tesler, Nicolás M Vargas, Yoav Kalcheim, Paul Wang, Juan Trastoy, Min-Han Lee, George Kassabian, Juan Gabriel Ramírez, et al. Subthreshold firing in mott nanodevices. *Nature*, 569(7756):388–392, 2019.
- [150] Qiangfei Xia and J Joshua Yang. Memristive crossbar arrays for brain-inspired computing. *Nature Materials*, 18(4):309–323, 2019.
- [151] I. Lo Vecchio, L. Baldassarre, F. D’Apuzzo, O. Limaj, D. Nicoletti, A. Perucchi, L. Fan, P. Metcalf, M. Marsi, and S. Lupi. Optical properties of V₂O₃ in its whole phase diagram. *Phys. Rev. B*, 91:155133, Apr 2015.
- [152] Sajeev John, H. Sompolinsky, and Michael J. Stephen. Localization in a disordered elastic medium near two dimensions. *Phys. Rev. B*, 27:5592–5603, May 1983.
- [153] Kyle L Grosse, Myung-Ho Bae, Feifei Lian, Eric Pop, and William P King. Nanoscale joule heating, peltier cooling and current crowding at graphene–metal contacts. *Nature Nanotechnology*, 6(5):287–290, 2011.
- [154] G Eason. Wave propagation in inhomogeneous elastic media, solution in terms of bessel functions. *Acta Mechanica*, 7(2-3):137–160, 1969.
- [155] S. G. Johnson. Notes on the algebraic structure of wave equations. *Notes on the algebraic structure of wave equations*, 2007.
- [156] Leslie Copley. Chapter 12 non-homogeneous boundary value problems: Green’s functions. In *Mathematics for the Physical Sciences*, pages 384–417. Sciendo Migration, 2014.
- [157] Albert Messiah. *Quantum Mechanics: Volume II*. North-Holland Publishing Company Amsterdam, 1962.
- [158] D. A. Stewart, W. H. Butler, X.-G. Zhang, and V. F. Los. Interfacial scattering in magnetic multilayers and spin valves. *Phys. Rev. B*, 68:014433, Jul 2003.
- [159] G. Chen. Thermal conductivity and ballistic-phonon transport in the cross-plane direction of superlattices. *Phys. Rev. B*, 57:14958–14973, Jun 1998.
- [160] John M Ziman. *Electrons and phonons: the theory of transport phenomena in solids*. Oxford university press, 2001.

- [161] Deyu Li and Alan JH McGaughey. Phonon dynamics at surfaces and interfaces and its implications in energy transport in nanostructured materials—an opinion paper. *Nanoscale and Microscale Thermophysical Engineering*, 19(2):166–182, 2015.
- [162] Witold Nowacki. *Thermoelasticity*. Elsevier, 2013.
- [163] Edward W Ng and Murray Geller. A table of integrals of the error functions. *Journal of Research of the National Bureau of Standards-B. Mathematical Sciences*, 73(1), 1969.